Technical Report
TR-23-14
September 2023

Approach to assessing the influence of roughness on fracture shear displacements

Margareta Lönnqvist
Billy Fälth

SVENSK KÄRNBRÄNSLEHANTERING AB

SWEDISH NUCLEAR FUEL
AND WASTE MANAGEMENT CO

Box 3091, SE-169 03 Solna
Phone +46 8 459 84 00
skb.se

SVENSK KÄRNBRÄNSLEHANTERING

ISSN 1404-0344
SKB TR-23-14
ID 2001386
September 2023

Approach to assessing the influence of roughness on fracture shear displacements

Margareta Lönnqvist, Billy Fälth
Clay Technology AB

Abstract

The objective of this study was to examine how the shear resistance on large fractures at the repository site in Forsmark potentially could be affected by non-planarity. The intention with the study was to provide results that can be used to assess the conservativeness of the fracture shear displacement estimates that are made for the Forsmark repository site.

The work was carried out by means of numerical modelling using 3DEC. Shear displacements on 300 m diameter fractures were simulated for both quasi-static loading conditions and dynamic (earthquake) loading conditions. Results were generated for different fracture surface geometries, surface wavelengths, surface deviation angles, and stress situations (different normal stresses). The impact on the results of soft fracture fillings/apertures was examined by normal stiffness variations on perfectly mated fractures as well as by explicit modelling of fracture apertures.

Fracture surface geometries with different degrees of idealisation were used:

- Wavy surfaces with undulations in only one direction.
- Alternating asperities created by superposition of two triangular waves in orthogonal directions.
- Fractal surfaces. Two types of synthetic fractal surfaces were considered: (1) surfaces with roughness parameters based on *JRC* determined from drill core samples, and (2) fractal surfaces with generic roughness properties.

The results from the quasi-static analyses can be summarized as follows:

- Fracture non-planarity imposes additional shear resistance and an associated reduction in shear displacement. The main parameters influencing the maximum shear displacement along a non-planar fracture are the (average) angle of deviation and the (dominant) wavelength of the surface undulations. Surfaces with steeply inclined asperities combined with small wavelengths give the largest reductions in slip.
- The efficiency of a given fracture surface type to reduce the shear displacements depends on if shearing takes place under high or low normal stress. Higher normal stress means that the non-planarity introduces more shear resistance.
- If the dominant wavelength is reasonably small in comparison with the size of the fracture (around 10 % of the fracture diameter or less) the apparent increase in friction angle i resulting from the corrugations is approximately equal to the (average) angle of deviation θ. On a non-planar fracture, the effect of dilation may be significant, particularly at low normal stresses. Hence, when simulating the effects of corrugations using a planar fracture with increased friction angle, the dilation angle should be set equal to the excess friction angle i.
- The influence of aperture variations or soft fracture filling materials, as simulated by a reduced normal stiffness, shows that the normal stiffness can be reduced by one to two orders of magnitude before any significant increase in the maximum shear displacements is observed. The results suggest that the maximum shear displacement on an undulated low-stiffness fracture may, for deviation angles in the range 5° to 15°, become some 5–15 % larger, as compared to the displacement on a high-stiffness fracture.

The results from the dynamic models are in qualitative agreement with the results from the quasi-static models in the sense that the maximum induced shear displacements along the non-planar fractures decrease with increasing angle of deviation. The efficiency of the corrugations to reduce the maximum induced shear displacement (expressed as the ratio of maximum slip along a non-planar fracture to that along the equally oriented and positioned planar fracture) appears to be dependent on details in the dynamic load. However, for the two dynamic load cases tested here, and for modest angles of deviation (~5°), the reduction in displacement becomes similar and on par with the reduction obtained in the quasi-static case.

The results presented here indicate that the shear resistance from large-scale undulations on Forsmark fractures gives shear displacement reductions in the range 5 % to 10 % relative to the case with a planar fracture surface. It can be concluded that the planar-fracture-assumption seems to be a fairly good but pessimistic approximation of an undulated fracture. Hence, models that include planar fractures with friction angles obtained from lab-scale samples (i.e. no account for large-scale undulations) should generate shear displacements that can be regarded as overestimates rather than underestimates.

Contents

1 Introduction

1.1 Background

The Swedish Nuclear Fuel and Waste Management Company (SKB) is planning to construct a deep geological repository for spent nuclear fuel at the Forsmark site in south-eastern Sweden. The repository will be constructed according to the KBS-3 method in which the spent nuclear fuel will be encapsulated in copper canisters and deposited, surrounded by a buffer of compacted bentonite clay, in vertical deposition holes at 400–500 m depth in crystalline rock.

A concern for the long-term performance of the repository is that future changes in load and/or groundwater pressure will trigger an earthquake and induce sufficiently large secondary displacements along near-fault fractures to damage intersected canisters (see Figure 1-1). The potential for reactivation of differently sized and oriented fractures as well as the magnitude of the resulting shear displacements have, therefore, been extensively investigated over the years by use of dynamic three-dimensional distinct-element models (e.g. Fälth 2018, Fälth et al. 2010, 2015, 2016). Such models are computationally very demanding and quickly become excessively large and time-consuming even for modest increases in resolution. To simplify the problem, the approach has been to approximate the surface geometry of the earthquake fault and of the near-fault fractures to be planar. Given currently available computational resources, a similar approach is likely to be taken also in the foreseeable future.

In contrast to the planar fracture representations used in the models discussed above, data indicate that the roughness of natural rock fractures has fractal properties with deviations from planarity on a wide range of length scales (e.g. Power and Tullis 1991). Although the near-fault fractures in the aforementioned studies are assigned mechanical properties that are in agreement with results from lab-scale tests and, therefore, to some extent account for small-scale fracture roughness, the absence of roughness or undulations on larger scales is believed to contribute to an overestimation of the calculated secondary shear displacements (Hökmark et al. 2019). Results from previous modelling work indicate that shear displacements on a perfectly mated fracture with modest deviations from planarity could be reduced by tens of percent compared with that on a correspondingly sized and oriented planar fracture (e.g. Dieterich and Smith 2009, Lönnqvist and Hökmark 2015a, Marshall and Morris 2012, Ritz and Pollard 2012). The reduction in slip could, however, be less pronounced if the fracture surfaces are mis-matched, i.e., if they are not in perfect contact everywhere, or if the fracture contains soft filling materials that could be compressed during shearing.

In this study, the impact of non-planarity on the shear displacements of large fractures is investigated. The purpose is to assess the conservatism in the approach to estimating fracture shear displacements of relevance for the safety assessment of the Forsmark repository (cf Hökmark et al. 2019).

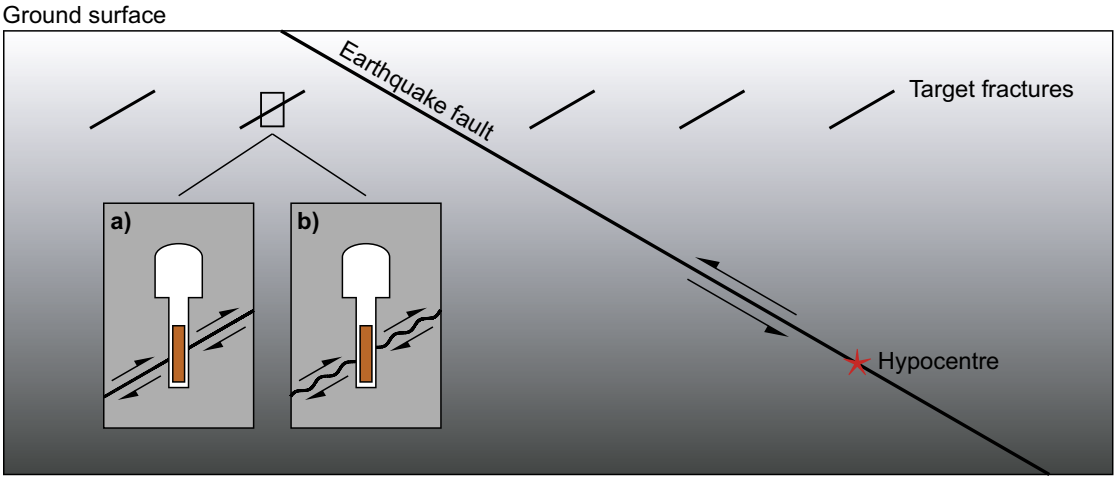

Figure 1-1. *Schematic illustration of earthquake-induced secondary shearing of a) planar near-fault fractures and b) undulating near-fault fractures across a canister position. Redrawn and modified after Fälth (2015, Figure 4).*

1.2 Objectives and scope

The objective of this study is to examine how the shear resistance on large fractures at the repository site in Forsmark potentially could be affected by non-planarity. The work is carried out by means of numerical modelling using the three-dimensional distinct-element code 3DEC (Itasca 2013, 2020).

In the first part of the study, a set of synthetic fracture surfaces is generated with deviations from planarity that are judged to be relevant for large fractures at repository depth. Each of these is implemented in 3DEC and subjected to quasi-static loading. Different aspects of shearing of non-planar fractures are examined:

- The influence of different types (regular triangle waves, fractals) and degrees of irregularities on the shear displacement at different stress-levels.
- The influence of asperities having finite strength.
- The influence of the degree of mis-match between the fracture surfaces and/or of the presence of soft fracture filling materials. These effects are examined both by variation of fracture normal stiffness and by explicit modelling of fracture apertures.

In the second part of the study, a sub-set of the previously analysed models are selected for dynamic analyses to determine if there are systematic and important differences in the mechanical response of a non-planar fracture to quasi-static and dynamic loading, respectively. The dynamic load applied here aims at being representative for the co-seismic near-fault effects that may be expected close to a rupturing fault. The load is obtained from a dynamic earthquake rupture simulation based on generic input data.

All calculations of shear displacements on fractures with matched surfaces as well as the dynamic large-scale simulations are performed using 3DEC, version 5 (Itasca 2013). The models where fracture apertures are explicitly modelled were built and analysed at a later stage in the project when a new version (version 7) (Itasca 2020) of 3DEC was available. For these types of models, this newer code version was used.

For the purpose of this study, the term *fault* is used to denote a structure that is sufficiently large to host an earthquake that may induce secondary fracture displacements of concern for the repository. The term *fracture* is used to denote all types of off-fault discontinuities regardless of their size, mode of formation, or deformation history.

2 Quasi-static loading

In this chapter, results from simulations of quasi-static slip on fractures with different degrees of non-planarity are presented. To simplify the problem, it is assumed that the fractures are subjected to a uniform stress field. The stress magnitudes at the Forsmark site vary linearly with depth (Glamheden et al. 2007). Hence, assuming that a fracture is, on average, subjected to a homogeneous stress field should be appropriate here where the purpose is to examine the impact of the fracture morphology per se.

The first subsection regards slip on mated fractures, i.e. fractures with no mis-match on the fracture surfaces. The simulations presented in the second subsection were performed to examine the potential impact of non-matedness/soft fracture fillings.

2.1 Mated fracture surfaces

2.1.1 Description of numerical model

Model outlines

The numerical model consists of a cube with side-length 1 600 m in which an isolated fracture with radius 150 m is included (cf Figure 2-1a). The model size is set such that influence on the results of the boundaries can be regarded to be negligible, i.e., to simulate an infinite volume. For convenience, the mean fracture plane is horizontal. The circular shape of the fracture is obtained by assignment of fracture properties within a circular region on the fracture plane. The fracture surfaces (cf Figures 2-1b and c) are constructed from triangular prisms (Kalenchuk et al. 2012, Lönnqvist and Hökmark 2015a) where the shortest side-length is 5 m. For the resolution considered here, the fracture surfaces consist of about 5 600 triangular sub-surfaces. The model is discretized with tetrahedral finite-difference elements with edge-lengths ranging from 1.8 m surrounding the fracture to 53 m near the model's boundaries.

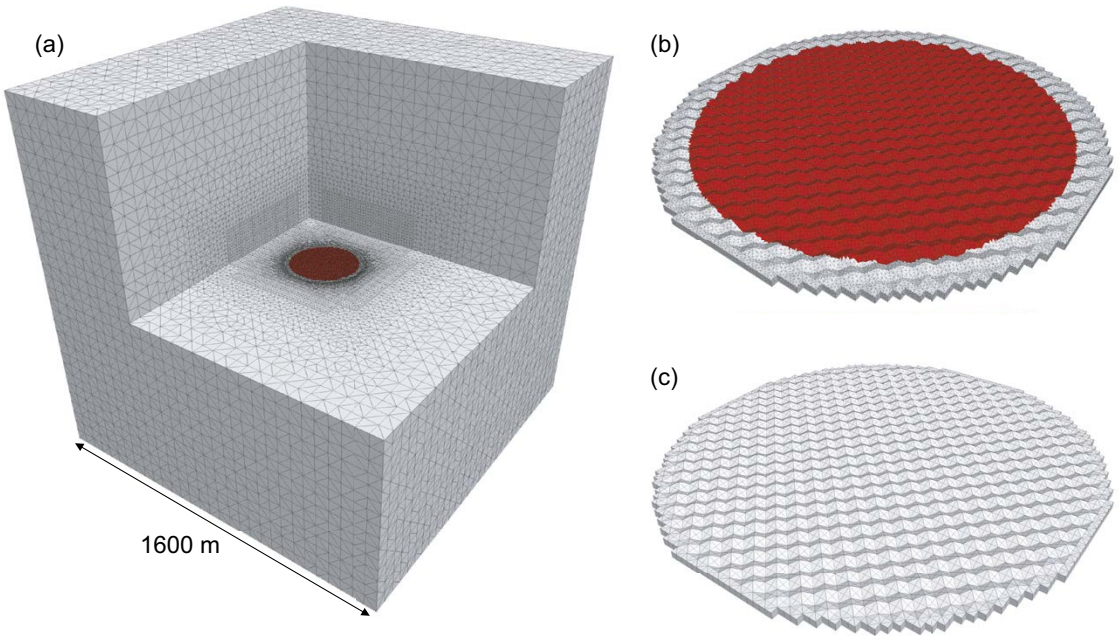

Figure 2-1. *(a) Illustration of the 3DEC model with a non-planar fracture (marked in red; alternating asperities, θ = 30°, λ = 20 m, see the following subsection for a detailed description of the types of fracture surfaces considered in this study). Note that parts of the model are hidden to expose the fracture surface. (b) Close-up of the fracture surface. (c) Corresponding view of the triangular prisms (block structure) used to create the fracture surfaces.*

Fracture surfaces

There are currently no data regarding the surface geometry of large fractures at the Forsmark site that can be used as input to the models. Instead, a set of synthetic surfaces with different types and degrees of deviations from planarity are considered. In several previous studies, the shape of such fractures has been approximated to be sinusoidal (e.g. Chester and Chester 2000, Marshall and Morris 2012, Ritz and Pollard 2012). Two types of non-planar surfaces are considered in this study: (1) triangle wave and (2) fractal.

The triangle wave geometry is illustrated in Figure 2-2a. The reason for choosing a triangle wave over a sinusoidal wave is two-fold: (1) it loosens the requirements on the resolution of the block structure from which the fracture surfaces are formed in 3DEC[1] and (2) allows for a more purified way to assess the correlation between the steepness of the asperities (in terms of the angle of deviation from the mean plane) and the increase in the effective friction angle of the non-planar surface (cf Lönnqvist and Hökmark 2015a). Two types of triangle wave surfaces with the same cross-sectional geometry but with different roughness anisotropy are constructed (see Table 2-1 for input parameters to the surfaces):

- Wavy surfaces (denoted *waves* in the following) with undulations in only one direction (to maximise the directional roughness anisotropy), see Figure 2-2b.
- A superposition of two triangular waves in orthogonal directions (to obtain a surface that has approximately isotropic roughness). These surfaces consist of pyramids with a square base whose tips alternate up and down (denoted *alternating asperities* in the following), see Figure 2-2c.

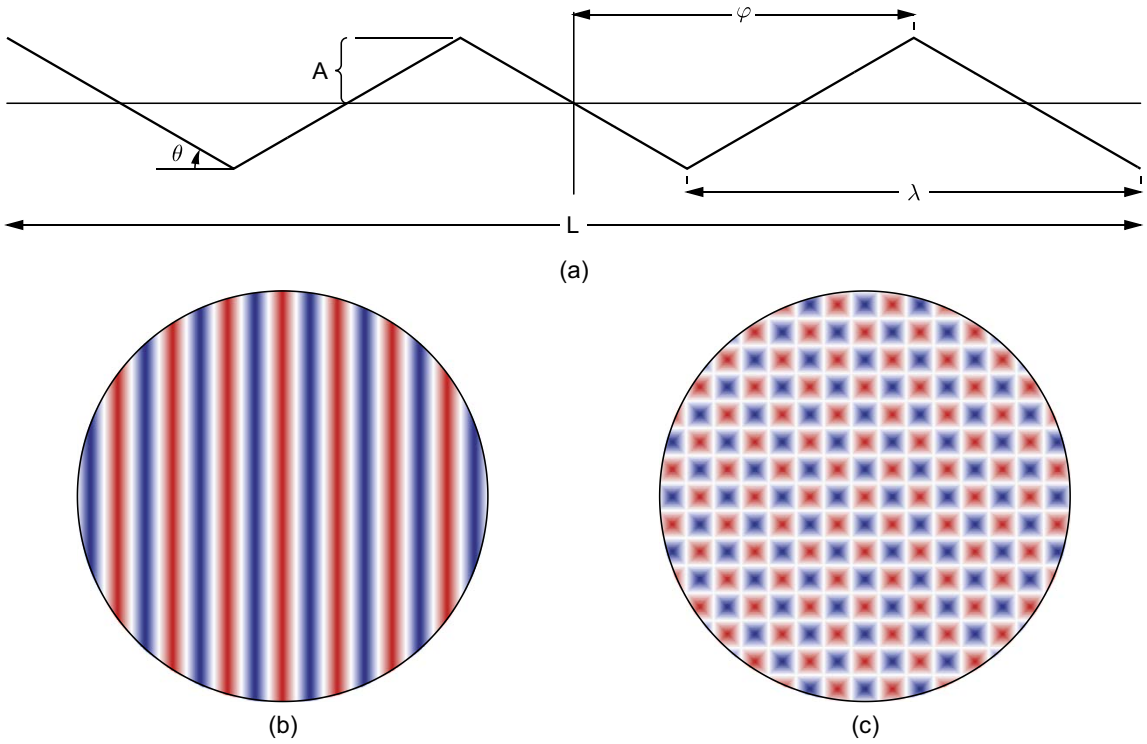

Figure 2-2. *(a) Description of a profile of length L = 2.5 λ with a "wavy" shape characterised by the amplitude (A), wavelength (λ), angle of deviation from the mean plane (θ), and phase (φ). (b) Example of a wavy surface (φ = 0°). (c) Example of waviness in two orthogonal directions (denoted "alternating asperities" in the following). Here, red and blue colours represent deviations above and below the mean plane, respectively.*

[1] A triangle wave is correctly reproduced using two blocks per wavelength whereas a sinusoidal wave needs more blocks in order to capture the smooth shape of the function.

Table 2-1. Summary of generic triangle wave fracture surfaces analysed in this study, cf Figure 2-2. Note that not all possible parameter combinations are used.

Type of surface	Angle of deviation (°)	Wavelength (m)
Waves	0*, 5, 10, 15, 20, 25, 30	10**, 20, 40, 60, 80, 100, 120
Alternating asperities	0*, 5, 10, 15, 20, 25, 30	20**, 40, 60, 80, 100, 120

* Planar surface.

** The minimum wavelength that can be resolved using a 5 m block side length.

As noted in Chapter 1, natural rock fractures have surfaces with a distribution of differently sized and inclined asperities at a wide range of length scales (e.g. Power and Tullis 1991). The distribution of irregularities typically has fractal properties. Here, two types of synthetic fractal surfaces are considered: (1) surfaces with roughness parameters based on *JRC* determined from drill core samples and (2) fractal surfaces with generic roughness (generic parameter combinations):

- The *JRC*-surfaces have been generated, and supplied, by Martin Stigsson, SKB (Stigsson 2020, personal communication). These were generated as square surfaces with a side length of 300 m and a grid spacing of 0.5 m (of which every 10th data point in the *x*- and *y*-directions were used to obtain the resolution used in 3DEC).
- The generic fractal surfaces are based on a pseudo-code ("SpectralSynthesisFM2D") given by Peitgen and Saupe (1988, pp 108) that has been implemented in Python. These were generated as square surfaces with a side length of 340 m and a grid spacing of 0.1 m (of which every 50th data point in the *x*- and *y*-directions were used to obtain the resolution used in 3DEC).

The down-sampling of the fractal surfaces was made to obtain the 5 m resolution set by the 3DEC model geometry. This means that wavelengths shorter than 10 m or 20 m (for waves or alternating asperities, respectively, see Table 2-1) are omitted, but the fractal properties of the remaining wave spectrum are maintained (cf Figure 2-3). According to Fang and Dunham (2013), the shear resistance imposed by surface roughness is governed by the shortest surface wavelength. This means that a down-sampled surface should give lower shear resistance than the corresponding original surface. However, if this means that the surfaces modelled here would give lower shear resistance than a typical large Forsmark fracture is difficult to say since there are no data available of large Forsmark fractures, as noted above.

The power spectral density function of an ideally self-similar or self-affine surface depends on the surface characteristics (Peitgen and Saupe 1988):

$$P(f_1, \ldots, f_n) = C\left(\sqrt{\sum_{i=1}^{n} f_i^2}\right)^{-2H-n} \tag{2-1}$$

Here, C is a constant, f is spatial frequency, H is the Hurst exponent and the factor C is a measure of the surface variance. The Hurst exponent H takes values between 0 and 1, with $H = 1$ meaning that the roughness has self-similar properties, i.e. a small portion of the surface when magnified isotropically will appear statistically identical to the entire surface. Values of H lower than 1 mean that short wavelength roughness is more pronounced. The root mean square roughness (h_{rms}) of a surface profile is equal to the square root of the area under the power spectral density function and is given by (Power and Tullis 1991).

$$h_{rms} = \left(\int_{f_{min}}^{f_{max}} P(f)df\right)^{1/2}. \tag{2-2}$$

The h_{rms} values here are given as fractions of the side length $L = 340$ m that was used when generating the surfaces (i.e., slightly larger than the 300 m diameter of the fractures used in the simulations), i.e., $h_{rms} = \varepsilon L$. Fractal surfaces with different values of H and of the fracture length fraction ε were generated and used in the simulations.

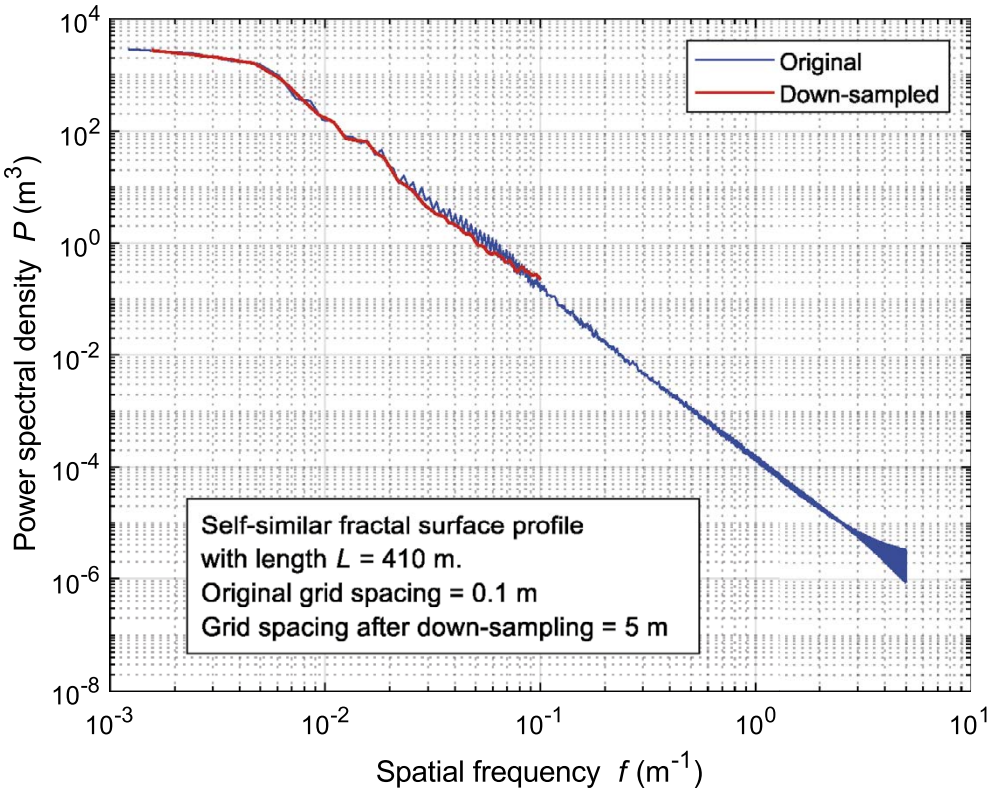

Figure 2-3. *Power spectral density P of two generic fractal surface profiles with self-similar properties. The down-sampled profile is created by picking every 50th grid point on the original surface. The lowest spatial frequency in the spectrum is 1/(2 L) m^{-1}. The highest frequency that can be represented is 1/λ (cf Figure 2-2). For the original surface this means 1/(2 × 0.1) m^{-1} and for the down-sampled surface 1/(2 × 5) m^{-1}. The curves show that the down-sampling only means that the upper cut-off frequency becomes lower while the fractal properties of the remaining spectrum are maintained.*

Material properties

As a base case assumption, the rock mass is assumed to respond to loading as a homogeneous, isotropic and linear elastic material with parameter values set according to the site descriptive model for Forsmark (Glamheden et al. 2007). The fracture is assigned an ideal elasto-plastic constitutive relation with constant normal and shear stiffnesses, zero tensile strength and shear strength based on a Mohr-Coulomb criterion. The base-case property values for the fracture are based on those given in the site descriptive model for Forsmark (Glamheden et al. 2007). Note that the same fracture friction angle is used as input to all models regardless of large-scale fracture surface geometry. The value of the shear stiffness is, however, set equal to that of the normal stiffness for convenience and to minimize any elastic deformations. The parameters and their values used in this study are summarized in Table 2-2.

Table 2-2. Material property values.

Component	Parameter	Value
Rock	Young's modulus, E (GPa)	70
	Poisson's ratio, ν (-)	0.24
	Density, ρ (kg/m^3)	2 700
	Friction angle*, ϕ (°)	60
	Cohesion*, c (MPa)	28
	Tensile strength*, σ_t (MPa)	13

Table 2-2. Continued.

Component	Parameter	Value
Fracture	Friction angle, ϕ (°)	35
	Cohesion**, c (MPa)	0
	Tensile strength**, σ_t (MPa)	0
	Normal stiffness, k_n (GPa/m)	656 (65.6*, 6.56*, 0.656*)
	Shear stiffness, k_s (GPa/m)	656

* Alternative parameter values used for sensitivity analyses, see Section 2.2.3.

** The fracture's cohesion and tensile strength are ramped down in small steps from intially high values to zero in order to minimize non-physical movements due to unbalanced forces at the beginning of a calculation cycle (Lönnqvist and Hökmark 2015a).

Stress models

The fracture is assumed to slip in response to a generic stress-field designed such that the maximum shear displacement along an optimally oriented planar fracture with 150 m radius is 50 mm. Here, the "optimal orientation" means the orientation that, for a given stress field and given fracture friction angle, gives the lowest fracture stability and hence largest potential for slip (see difference between shear stress and shear strength in Figure 2-4). At the Forsmark site, the (effective) normal stress acting on optimally oriented fractures at repository depth is typically around 10 to 15 MPa throughout the repository's life-span (see Hökmark et al. 2010, Chapters 6 and 7). This is used as a guideline to derive the base-case stress model in which the normal stress acting on the optimally oriented planar fracture is 12 MPa. The impact of groundwater pressure is ignored. To assess if the efficiency of a given surface irregularity to reduce the maximum shear displacements is different if shearing takes place at lower or higher levels of normal stress (as may be the case during an earthquake (cf e.g., Fälth et al. 2010, Figure 5-13)), three additional normal stress-levels are considered: 1 MPa, 6 MPa and 24 MPa. To cover a wide range of stress conditions, these are schematically chosen to be 1/12, 1/2, and 2 times the 12 MPa base case value, respectively.

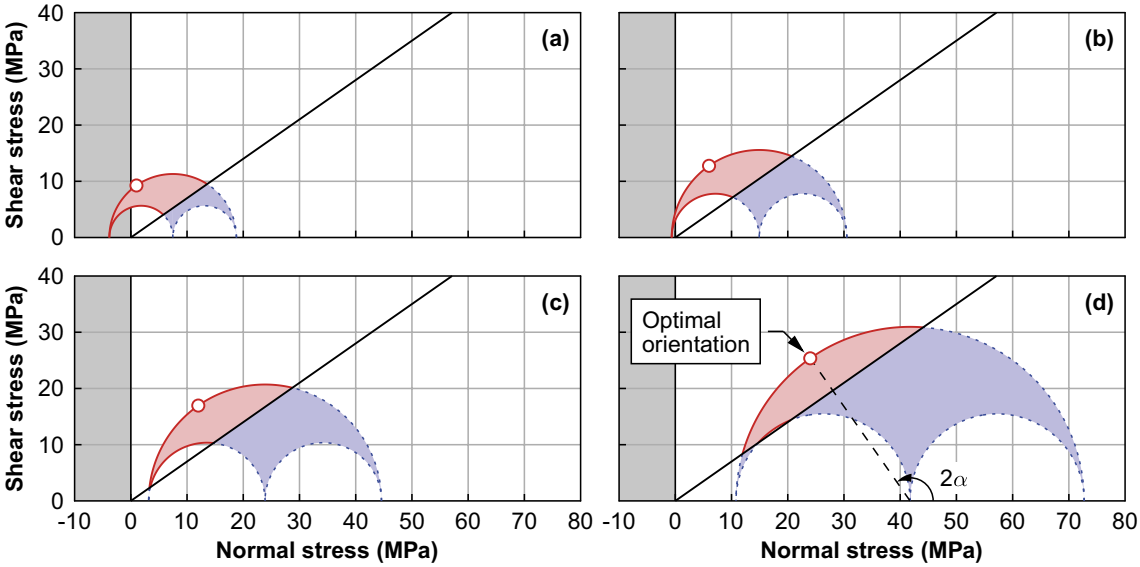

Figure 2-4. *Illustrations of the stress models. Each Mohr-circle in the σ_1-σ_3-plane is derived such that the maximum shear displacement along an optimally oriented planar fracture with uniform shear strength will be 50 mm at a normal stress of (a) 1 MPa, (b) 6 MPa, (c) 12 MPa (base-case model) and (d) 24 MPa. Stable fracture orientations (below the strength envelope) are located in the blue shaded area and unstable fracture orientations (above the strength envelope, ϕ = 35°) are located in the red shaded area. The grey region represents tensile stresses.*

The principal components of the stress tensor in each stress model are derived starting from a closed-form solution (Segedin 1951) for the slip distribution along an isolated, circular fracture embedded in an infinitely large linear elastic material and subjected to a uniform and positive (quasi-static) change in shear stress. Knowing the fracture's radius (a = 150 m) and the properties of the surrounding rock mass (cf Table 2-2), the change in shear stress ($\Delta\tau$) required to induce a maximum shear displacement $u_{s,\max}$ (here 50 mm) is given by

$$\Delta\tau = \frac{u_{s,max}}{a}\frac{\pi(2-\vartheta)}{8}\frac{G}{(1-\vartheta)} \tag{2-3}$$

where G is the shear modulus and ν is Poisson's ratio. Assuming further that the fracture has Mohr-Coulomb shear strength, the total shear stress (τ) is given by

$$\tau = \sigma_N \tan\left(\phi\right) + \Delta\tau \tag{2-4}$$

where σ_N is the normal stress acting on the fracture and ϕ is the fracture friction angle. If σ_N and τ are the stresses acting on the optimally oriented fracture, the major, most compressive (σ_1) and minor (σ_3) principal stresses are given by (e.g. Brady and Brown 1993)

$$\begin{aligned}\sigma_1 &= \sigma_N + \tau\frac{\left[1-\cos\left(2\alpha\right)\right]}{\sin\left(2\alpha\right)}\\ \sigma_3 &= \sigma_N - \tau\frac{\left[1+\cos\left(2\alpha\right)\right]}{\sin\left(2\alpha\right)}\end{aligned} \tag{2-5}$$

where $\alpha = 45° + \phi/2$. The intermediate principal stress (σ_2) is set at $\sigma_2 = 0.5\ (\sigma_1 + \sigma_3)$ in all cases. The resulting four stress models with σ_N set at 1 MPa, 6 MPa, 12 MPa or 24 MPa are presented in Figure 2-4.

Boundary conditions

Since the principal components of the *in situ* stress tensor are not (necessarily) aligned with the model's axes, the boundaries are locked in all directions to prevent displacements along the boundaries.

2.1.2 Evaluation of results

To assess how the response of the different fracture surfaces differs from the perfectly planar fracture, the following quantities are calculated:

- The maximum shear displacement and the distribution of shear displacements across the fracture surfaces.
- The (apparent) shear strength.
- The average slip direction.

Shear displacements

The primary objective is to determine the maximum shear displacement. On a planar and uniformly loaded fracture, the largest shear displacements occur at the centre of the fracture (Segedin 1951). On a non-planar fracture, the maximum may be found elsewhere on the fracture plane (e.g. Lönnqvist and Hökmark 2015a). In this study, the maximum (regardless of its position on the fracture plane), is used.

Apparent shear strength

If shearing takes place under normal stress levels that are sufficiently low that the asperities are not sheared off, the shear strength can be expressed as (e.g. Lindblom 2010)

$$\tau^u = \sigma_N\, tan(\phi + i) \tag{2-6}$$

where ϕ is the fracture friction angle and i is the dilation angle. It was demonstrated experimentally by Patton (1966), using plaster samples with saw-tooth surfaces, that i is approximately equal to the angle of deviation, θ. This has been demonstrated numerically to be a reasonable approximation also for triangular waves (Lönnqvist and Hökmark 2015a) and for fractal surfaces (Fälth et al. 2018).

It has been suggested that the impact of the surface irregularities could be translated into an apparent friction angle, ϕ', that would be valid on a similarly sized and oriented planar fracture (e.g., Kaven et al. 2012, Lönnqvist and Hökmark 2015a). A simple way to estimate ϕ' is to assume that the relationship between the shear stress drop $\Delta\tau$ and the maximum shear displacement can be expressed according to Equation 2-3 and Equation 2-4 regardless of fracture surface geometry, i.e.,

$$\frac{\Delta\tau}{\Delta\tau^*} \equiv \frac{\tau^* - \sigma_N^* \tan(\phi')}{\tau^* - \sigma_N^* \tan(\phi)} = \frac{u_{s,\max}}{u^*_{s,\max}} \tag{2-7}$$

where the parameters marked with an asterisk (*) refer to the optimally oriented planar fracture. Solving for ϕ' gives

$$\phi' = \tan^{-1}\left[\left(\tau^* - \Delta\tau^* \frac{u_{s,\max}}{u^*_{s,\max}}\right) \Big/ \sigma_N^*\right]. \tag{2-8}$$

The excess apparent friction angle, or dilation angle i, is then given by

$$i = \phi' - \phi\,. \tag{2-9}$$

It should be noted that this approach to estimate the apparent friction angle fails if $\sigma_N \leq 0$ MPa or if $u_{s,\max} \ll u^*_{s,\max}$:

- In the first case, the apparent friction angle is indeterminable.
- In the second case, Equation 2-8 gives the minimum friction angle for which the planar and optimally oriented fracture is stable, i.e., $\phi' = \tan^{-1}(\tau^*/\sigma^*_N)$.

Also note that here, the normal stress σ_N on the undulated fracture is assumed to be constant and equal to the normal stress σ^*_N on the corresponding planar fracture. This is an idealisation that corresponds to the conditions in a constant load shear box lab test where there is no restriction in normal displacement. However, on a fracture with a finite size, the normal displacement is restricted due to the presence of the fracture edges (the assumption made here of an elastic rock mass means zero displacement condition along the fracture edges). Hence, during shearing of a non-planar fracture, the dilation imposed by the irregularities will lead to an increase in normal stress.

Average slip direction

The Wallace-Bott hypothesis states that slip along a fracture occurs in the direction of the maximum resolved shear stress (e.g. Lisle 2013). This is the case for perfectly planar fractures. For non-planar fractures, the slip direction could deviate from the maximum resolved shear stress direction (e.g. Lejri et al. 2015, Lisle 2013, Marshall and Morris 2012). To assess the slip direction along the fractures considered in this study, the average slip direction (φ) is calculated from the average horizontal slip components ($\bar{u}_{s,x}$ and $\bar{u}_{s,y}$) calculated as

$$\bar{u}_{s,x} = \frac{1}{A}\sum_i A_i \cdot u_{s,x_i}, \bar{u}_{s,y} = \frac{1}{A}\sum_i A_i \cdot u_{s,y_i} \tag{2-10}$$

where A is the fracture's surface area, A_i is the area associated with subcontact i, and $u_{s,xi}$ and $u_{s,yi}$ are the shear displacement components in the x- and y-direction, respectively, at subcontact i. The average slip direction, φ, is then given by

$$\varphi = \arccos\frac{\bar{u}_{s,y}}{\sqrt{\bar{u}^2_{s,x} + \bar{u}^2_{s,y}}}\,. \tag{2-11}$$

2.1.3 Results

Different surface types: base-case stress model

The influence of the type and degree of undulations and how their response to loading deviates from the idealised planar surface are investigated for the case with 12 MPa normal stress. The tested surface types include single wavelengths in one direction ("waves"), in two orthogonal directions ("alternating asperities") and a superposition of waves with different wavelengths ("fractals").

Planar fractures: comparison with analytical solution

The slip distribution, i.e., the slip u_s as function of radial position r, on an isolated, circular fracture with radius a embedded in an infinitely large linear elastic continuum (with Poisson's ratio, ν, and shear modulus, G) and subjected to a uniform and positive (quasi-static) change in shear stress ($\Delta\tau$) is given by Segedin (1951):

$$u_s(r) = \frac{8}{\pi(2-\nu)}\frac{(1-\nu)}{G}\Delta\tau a\sqrt{1-\left(\frac{r}{a}\right)^2}\,. \qquad (2\text{-}12)$$

The ability of 3DEC to reproduce the analytical solution (Equation 2-12) is tested. Figure 2-5 (top) shows examples of the shear displacement of an optimally oriented planar fracture as calculated using the two methods. The results are in good agreement both in terms of the shape of the slip distribution and in terms of the slip magnitude. The results in Figure 2-5 (bottom left) show that the slip takes place in the direction of the maximum resolved shear stress, as expected.

The optimal plunge angle of the major principal stress component with respect to a planar fracture is $45° - \phi/2$, where ϕ is the fracture friction angle (e.g. Brady and Brown 1993). For the friction angle considered in this study (35°, see Table 2-2), the optimal plunge angle is 27.5°. Figure 2-5 (bottom right) shows simulated fracture shear displacement as function of plunge angle. The results show that 3DEC generates results that are in good agreement with theory also in this respect.

Wavy fractures

The wavy fractures are the simplest of the non-planar surface-types considered here with corrugations consisting of a single triangular wave in one direction along the fracture-plane. This type of surface geometry also has a large roughness-anisotropy. The magnitude of the maximum shear displacements along such a fracture should, therefore, be sensitive to the direction of loading (cf e.g. Lönnqvist and Hökmark 2015a, Marshall and Morris 2012). Although it is primarily the impact of segments opposing the direction of slip that is of concern in this study, different trends (β) of the major principal stress (or, equivalently, the direction of the maximum resolved shear stress) with respect to the orientation of the corrugations are, for completeness, tested. Here, $\beta = 0°$ is parallel to the ridges of the waves.

The results shown in Figure 2-6 (upper) indicate that a modest θ value has a significant impact on the fracture displacement. With $\theta = 10°$ the displacement is reduced by 50 % and with $\theta > 20°$ effectively no displacement is generated. The middle graphs in Figure 2-6 show that the results are highly sensitive to the direction of the stress tensor, as could be expected from the considerable surface anisotropy of the wavy surface. The lower diagram in Figure 2-6 shows how the fracture displacement depends on the plunge of the major principal stress. The peak value of displacement occurs at lower plunge angles for larger θ. This is consistent with higher shear resistance and an effectively higher friction angle (cf discussion in previous subsection).

Figure 2-7 shows how the wavelength of the surface deviations influences the results. Shorter wavelengths tend to give higher shear resistance. It appears that, for the fracture size and type of surface geometry considered here, reducing the wavelength below 20 m does not give any significant additional shear resistance.

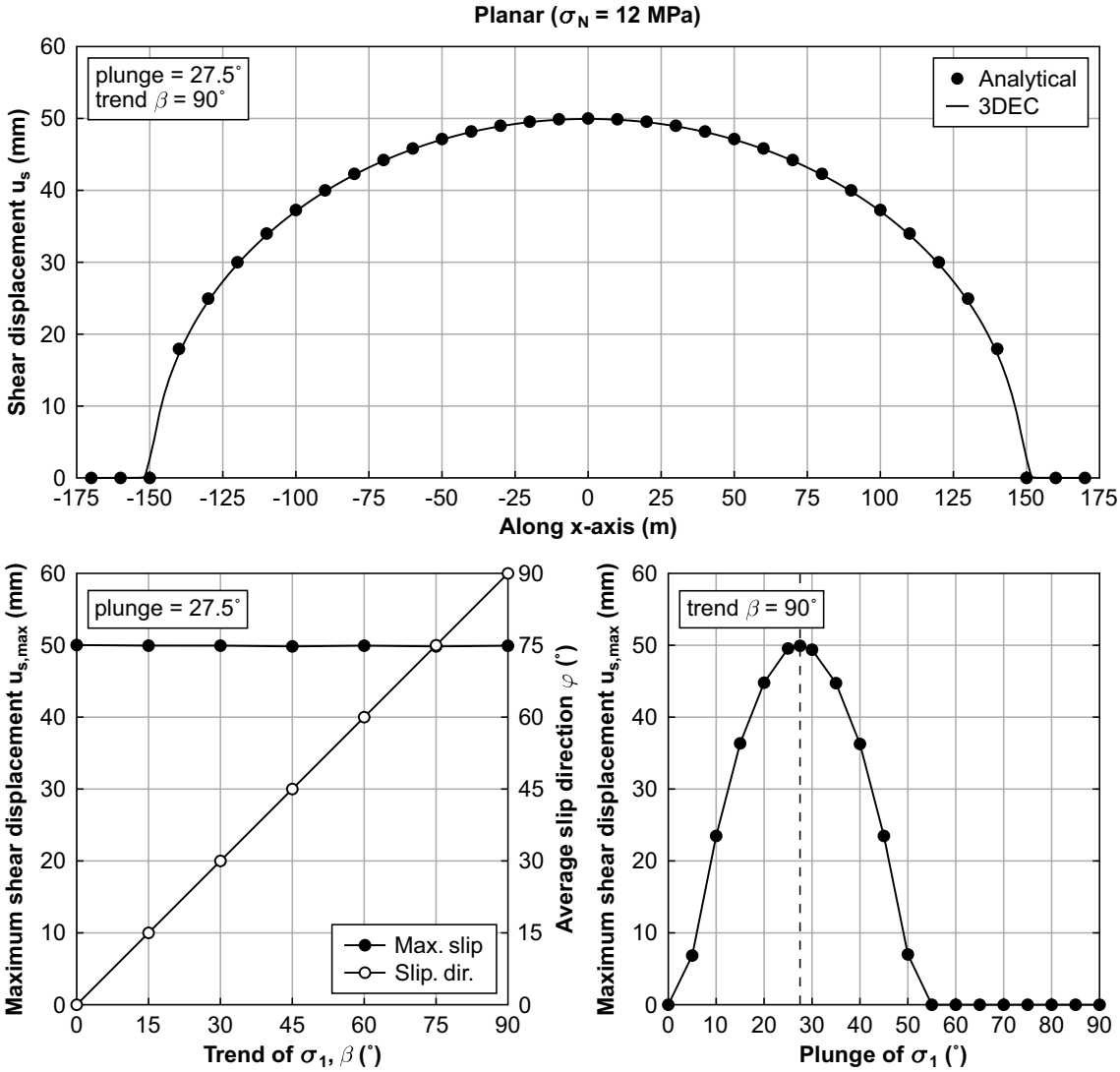

Figure 2-5. *Top: Comparison between the slip distributions along the optimally oriented planar fracture as calculated by the analytical solution (Equation 2-12) and by 3DEC. Bottom left: Maximum shear displacements along the fracture as a function of the trend of the major principal stress and corresponding average slip direction evaluated using Equation 2-11. Bottom right: Maximum shear displacements along the fracture as a function of the plunge of the major principal stress with respect to the mean fracture orientation.*

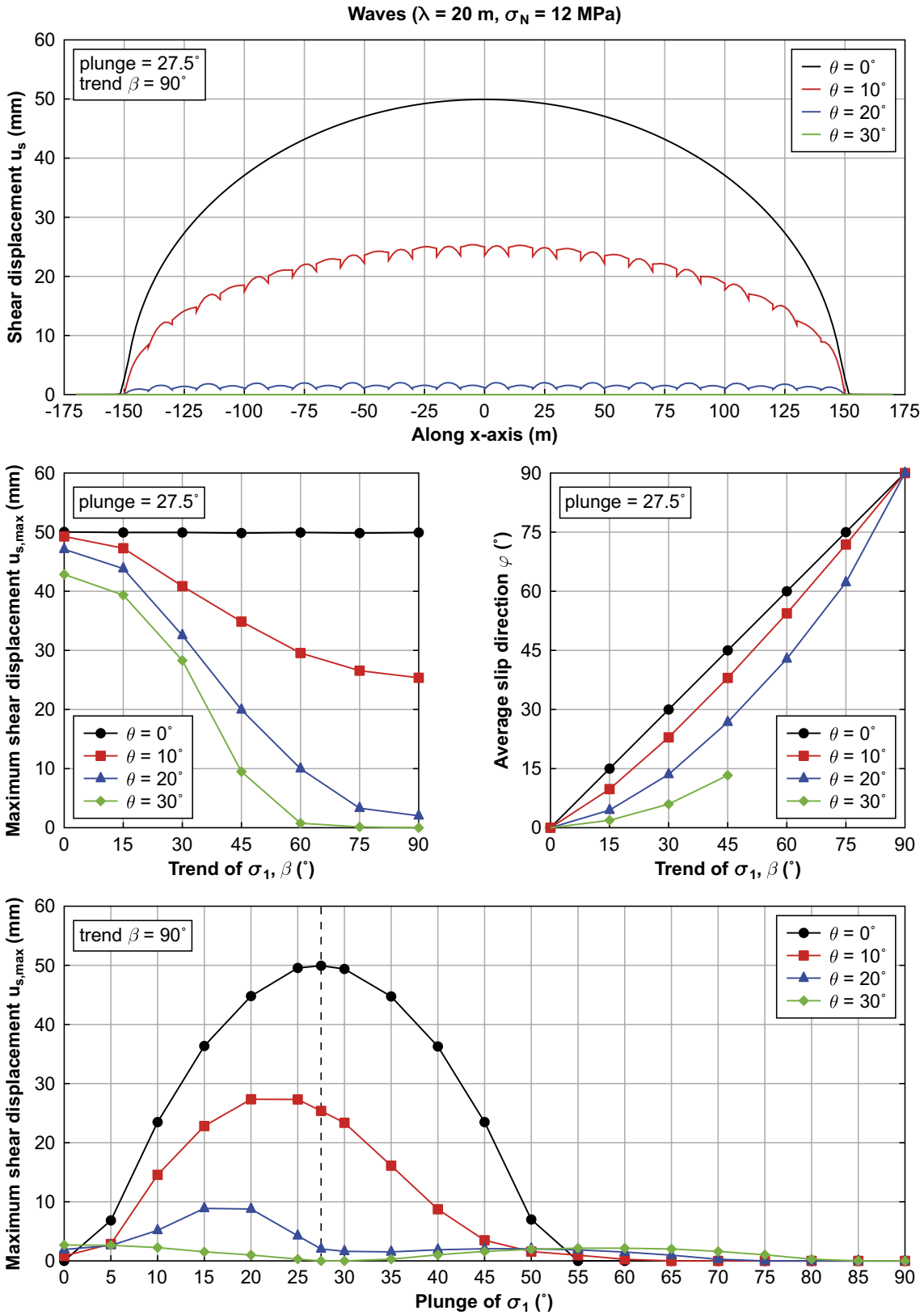

Figure 2-6. *Top: Comparison between the slip distributions along the optimally oriented planar fracture and wavy fractures with angles of deviation in the range 10° to 30°. Middle left: Maximum shear displacements along the fracture as a function of the trend of the major principal stress. Middle right: Corresponding average slip direction evaluated using Equation 2-11. Note that the average slip direction is judged to be indeterminable when the maximum shear displacement is less than 1 mm. Bottom: Maximum shear displacements along the fracture as a function of the plunge of the major principal stress with respect to the mean fracture orientation.*

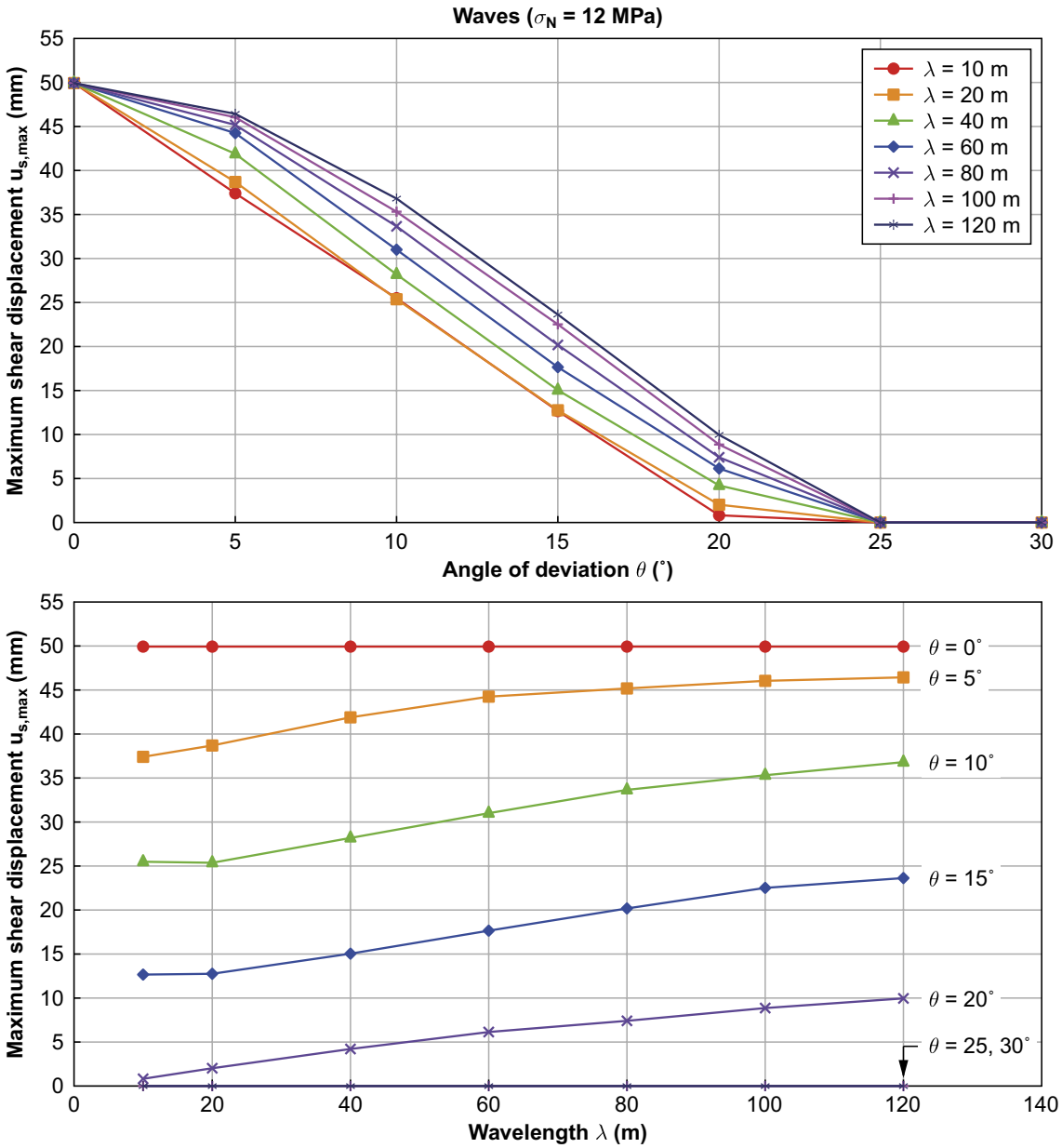

Figure 2-7. *Top: Maximum shear displacements along the wavy fractures as functions of the angle of deviation for wavelengths in the range 10 m to 120 m. Bottom: Corresponding results shown as functions of the wavelength.*

The shear displacement results are converted to apparent excess friction angle using Equation 2-9. The results of the calculation are plotted in Figure 2-8. The results show that, for the assumed stress model and for surface wavelengths shorter than some 60 m, the additional shear resistance imposed by the surface irregularities corresponds to an additional friction angle that is approximately equal to the angle of deviation. This confirms the results of previous studies, cf the discussion in Section 2.1.2. Note in Figure 2-8 that the excess friction angle "saturates" at 20°, i.e., it does not continue to increase for further increase in θ. This is because further increase in θ makes the fracture stable and no slip takes place. This causes the estimate of the apparent friction angle to fail, see discussion in Section 2.1.2.

Furthermore, the results in Figure 2-8 are also in accord with the results in Figure 2-6 (lower). Recall that the optimal plunge angle of the major principal stress component with respect to a planar fracture is $45° - \phi/2$. According to the results in Figure 2-8 one would then expect the optimal plunge angle for a wavy surface to be approximately $45° - (\phi + \theta)/2$. For $\theta = 10°$, this would give an optimal plunge angle of about 22.5° while $\theta = 20°$ corresponds to a plunge angle of about 17.5°. This is just what is indicated by the results in Figure 2-6 (lower).

Alternating asperities

The surfaces with alternating asperities are created by a superposition of triangular waves in two orthogonal directions and, therefore, have approximately isotropic roughness. The isotropy of the surfaces is examined by a variation of the σ_1 trend β. Since this type of surface has a symmetry plane oriented at 45° with respect to the y-axis, it is sufficient to consider values of β in the range 45° to 90°. The results in Figure 2-9 (middle right) confirm that the surface is (approximately) isotropic and that the average slip direction is the same as the direction of the maximum resolved shear stress.

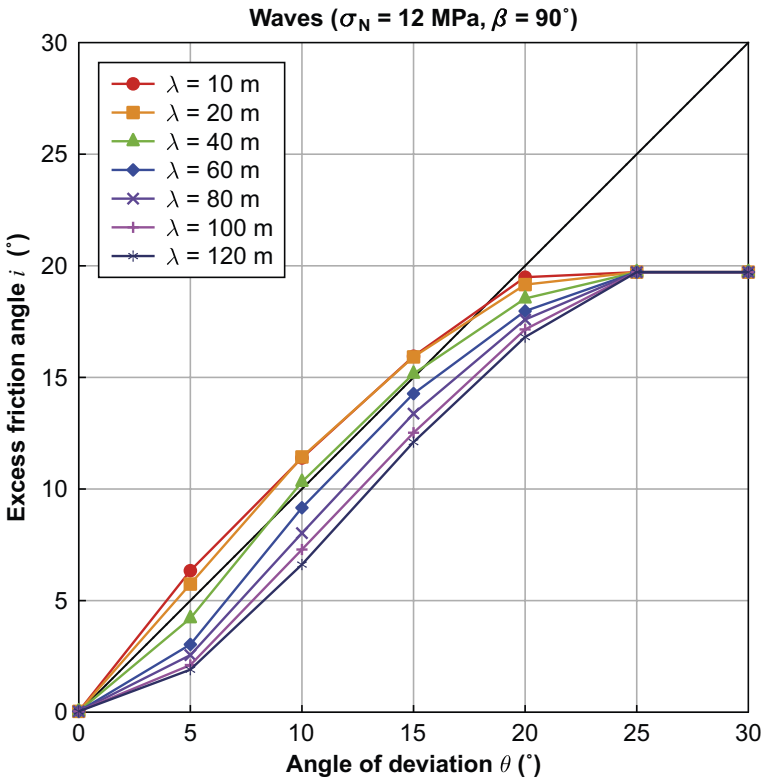

Figure 2-8. *Calculated apparent excess friction angle i (Equation 2-9) for each of the wavy fractures. The black diagonal line indicates the case for which the apparent excess friction angle is equal to the angle of deviation.*

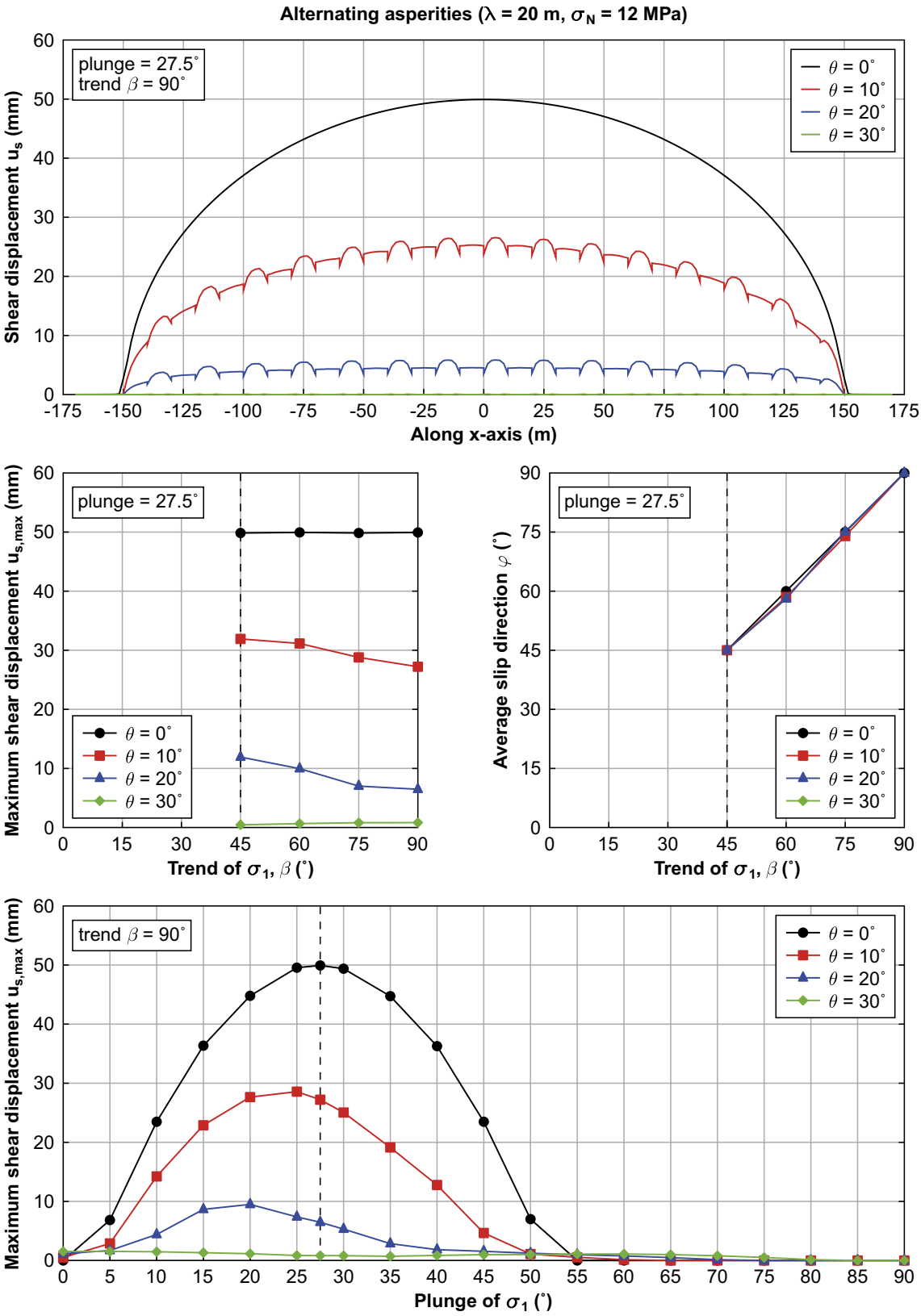

Figure 2-9. *Top: Comparison between the slip distributions along the optimally oriented planar fracture and the fractures with alternating asperities with angles of deviation in the range 10° to 30°. Middle left: Maximum shear displacements along the fracture as a function of the trend of the major principal stress. Middle right: Corresponding average slip direction evaluated using Equation 2-11. Note that the average slip direction is judged to be indeterminable when the maximum shear displacement is less than 1 mm. Bottom: Maximum shear displacements along the fracture as a function of the plunge of the major principal stress with respect to the mean fracture orientation.*

Figure 2-10 shows the maximum shear displacements along the fractures with alternating asperities for wavelengths in the range 20 m to 120 m. The mechanical response of these fractures is qualitatively similar to that of the wavy fractures (cf Figure 2-7) in the sense that the maximum shear displacement decreases with increasing angle of deviation for all tested wavelengths. In addition, as for the wavy fractures, the shear resistance appears to increase with reduced wavelength. Quantitatively, the slip magnitudes along the fractures with alternating asperities are generally larger than the corresponding ones along the wavy fractures. For instance, for wavelength 20 m the alternating asperity model gives displacements that are 3 %–300 % larger (for θ in the range 5° to 20°) than those in the wavy fracture model. The difference in mechanical response between the two surface types could be explained by noticing that the areas of the fracture segments opposing the direction of the maximum resolved shear stress are smaller than for the wavy fractures.

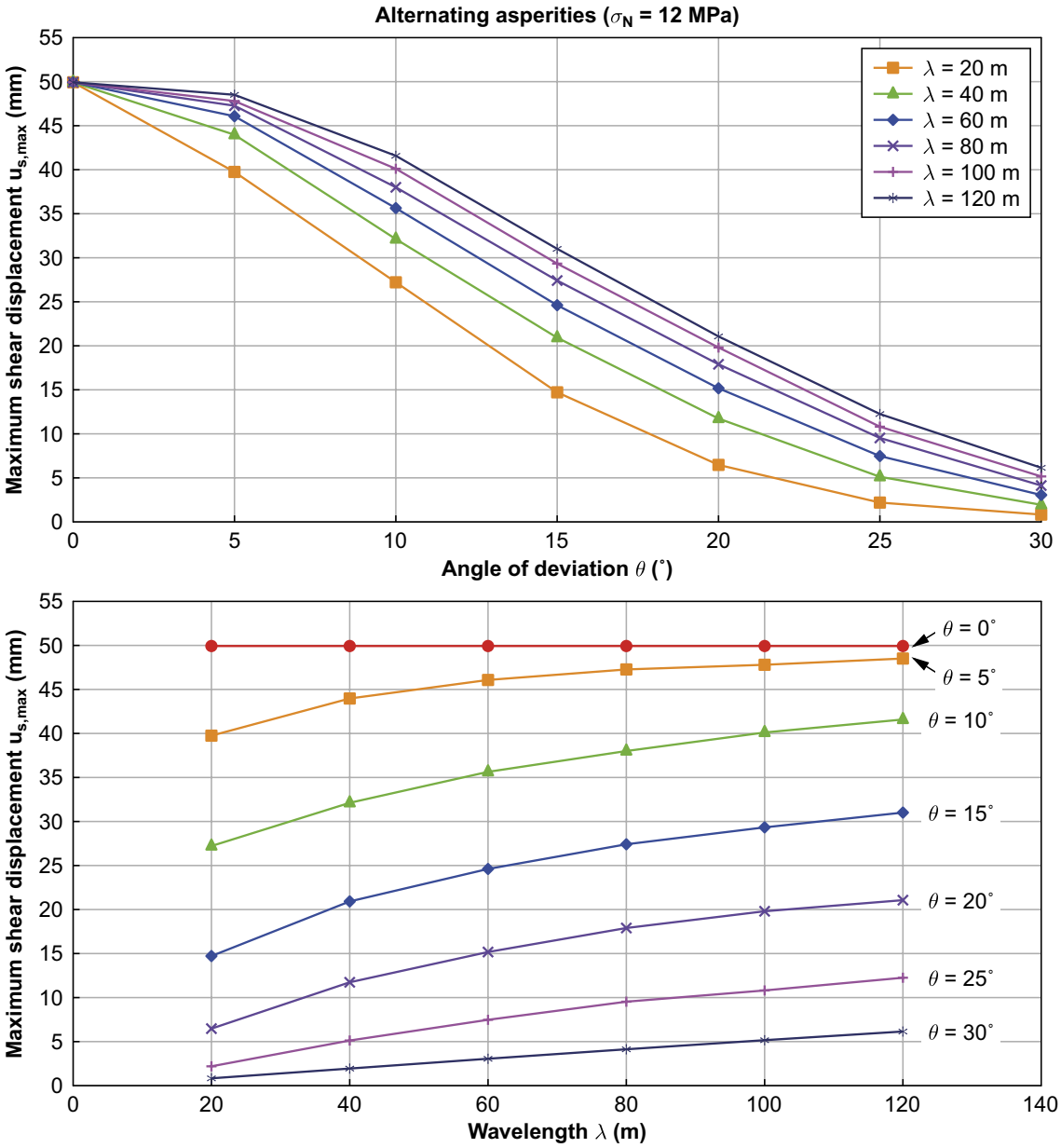

Figure 2-10. *Top: Maximum shear displacements along fractures with alternating asperities as functions of the angle of deviation for wavelengths in the range 20 m to 120 m. Bottom: Corresponding results shown as functions of the wavelength.*

The results in Figure 2-10 show how the shear displacement depends on the surface roughness wavelength. As for the wavy fractures (previous subsection), a shorter wavelength means a larger shear resistance and smaller displacements. Here, the shortest wavelength considered is 20 m (while it is 10 m for the wavy fractures), and it is not clear from the results how much the shear resistance would increase for wavelengths shorter than 20 m.

Figure 2-11 shows the calculated excess friction angles based on all results presented in Figure 2-10. For wavelengths up to about 40 m, the angle of deviation (θ) is a reasonable approximation of the excess friction angle. Note in Figure 2-9 that the excess friction angle tends to "saturate" at 20°, i.e., it does not continue to increase for further increase in θ. This is because further increase in θ gives such a high stability that very little slip takes place. This causes the estimate of the apparent friction angle to fail, see discussion in Section 2.1.2.

In addition, considering the results in Figure 2-9 (bottom), one can note that the optimal plunge angle is in reasonable agreement with the excess friction angle values in Figure 2-11 (cf discussion in previous subsection).

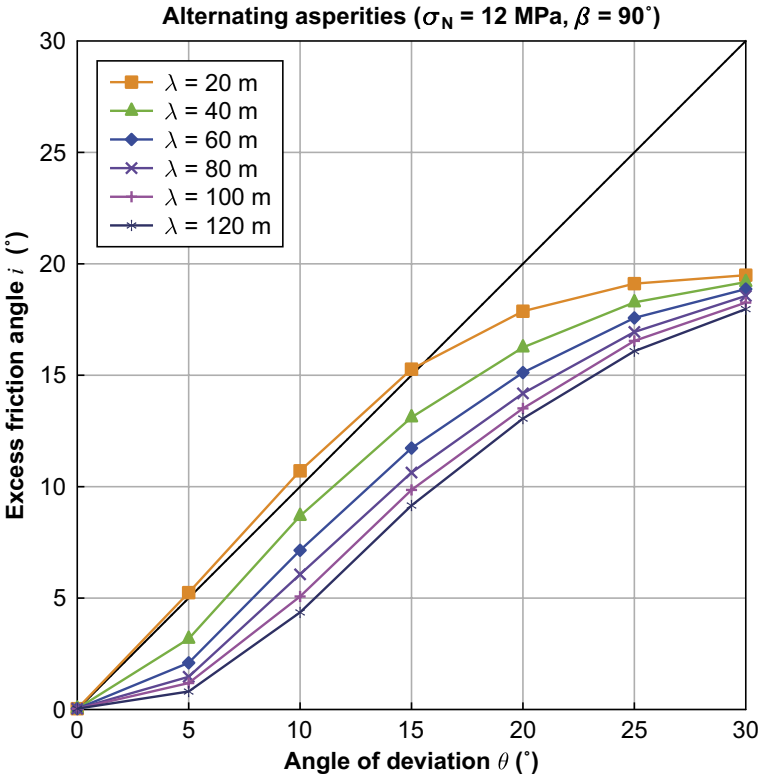

Figure 2-11. *Calculated excess friction angle (Equation* 2-9*) for each of the fractures with alternating asperities. The black diagonal line indicates the case for which the excess friction angle is equal to the angle of deviation.*

Fractal surfaces

The third type of surface considered here is fractal. The purpose of these surfaces is to assess if fractal surfaces (*i.e.*, surfaces with a distribution of asperities with different sizes and steepness) respond to loading differently compared with the generic surfaces (waves and alternating asperities) in any systematic way. Two types of synthetic fractal surfaces are considered: (1) surfaces with roughness parameters based on *JRC* determined from drill core samples and (2) fractal surfaces with generic roughness (generic parameter combinations). Note that although the fractal geometry gives an indication of the roughness on all scales, any impact of the small-scale roughness on the lab-scale shear strength is ignored and all fractal surfaces have shear strength parameters set according to Table 2-2.

Figure 2-12 shows the maximum shear displacements as functions of the *JRC*. These surfaces do not reduce the maximum shear displacements in any significant way (except for the surfaces based on the largest tested *JRC*-value). Plotting the results as functions of the average angle of deviation (see Figure 2-13) shows that the angles of deviation are modest for the fractal surfaces (up to some 5°) but that the response of these surfaces is qualitatively similar to that of the surfaces with alternating asperities. The *JRC*-surfaces tend to give less shear resistance than the alternating-asperity-surfaces and plot above the alternating-asperities-curve with corresponding angles of deviation and a wavelength of 20 m (minimum wavelength that can be resolved using the 5 m-grid). This suggests that the JRC-surfaces do not contain any significant amount of short wavelength roughness that could contribute to reducing the maximum shear displacement.

Since the *JRC*-surfaces have relatively small angles of deviation, a set of fractal surfaces based on generic roughness parameters are generated. As for the wavy surfaces and the alternating asperity surfaces, two issues are considered. First, it is assessed that the randomness does not introduce any unintentional directional anisotropy. Second, the average angle of deviation and how it relates to the effective shear strength of the fracture are determined.

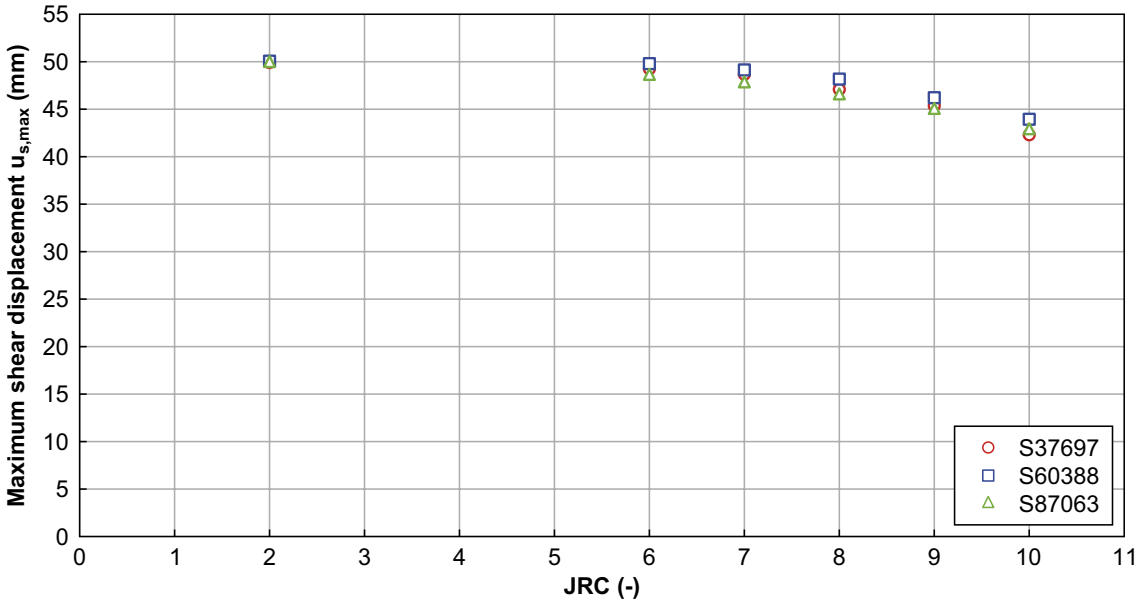

Figure 2-12. *Maximum shear displacements along the synthetic fractures with roughness parameters based on JRC determined from drill core samples as functions of the JRC. The numbers in the legend refer to different seeds used to generate the surfaces.*

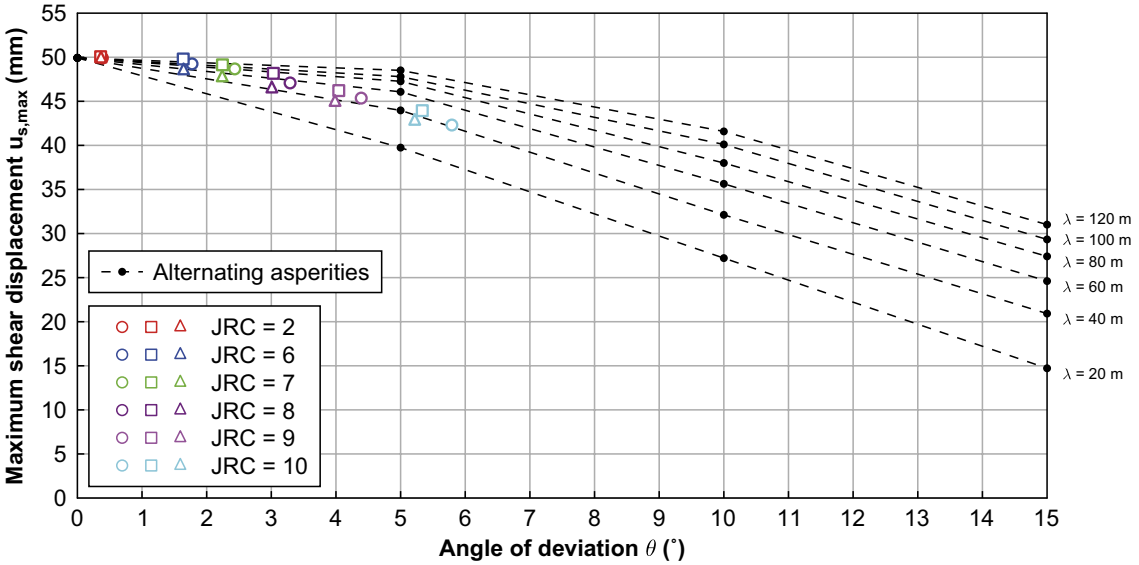

Figure 2-13. *Maximum shear displacements along the synthetic fractures with roughness parameters based on JRC determined from drill core samples as functions of the average angle of deviation. The JRC-surfaces are compared with the surfaces with alternating asperities (their wavelengths are indicated in the right margin).*

Figure 2-14 shows results for two non-planar surfaces with the same value of $h_{rms} = 0.01\ L$, but with different values of H (cf Equation 2-1 and 2-2). The results in the upper plot show that a surface with a lower value of H (more small-scale undulations in the spectrum) gives higher shear resistance. Hence, in this respect the results follow the same trend as that of the results for the generic surface geometries presented above. The trend is also in accord with the findings by e.g. Fang and Dunham (2013) who proposed an analytical model for estimating the shear resistance from the roughness on faults/fractures with self-similar fractal properties. According to their model, the shear resistance scales to the ratio Δ/λ_{min}, where Δ is slip and λ_{min} is the shortest wavelength on the surface.

The middle plots in Figure 2-14 show that the surfaces appear to be directionally isotropic, as was also found for the surfaces with alternating asperities.

Figure 2-15 shows peak displacement versus average angle of deviation for the fractal surfaces plotted along with the corresponding results for the generic surfaces with alternating asperities. In general, the response of the fractal surfaces follows trends similar to those of the generic surfaces. Notable is also that lower H values give results that tend to follow the trends of the generic surfaces with shorter wavelengths. The two values indicated by arrows correspond to the surface realisations considered in Figure 2-14. One can note that the angles of deviation for these surfaces are in general agreement with the optimal plunge angles indicated by the results in Figure 2-14 (lower). This indicates that the average angle of deviation corresponds to an excess friction angle, as is the case for the generic surfaces.

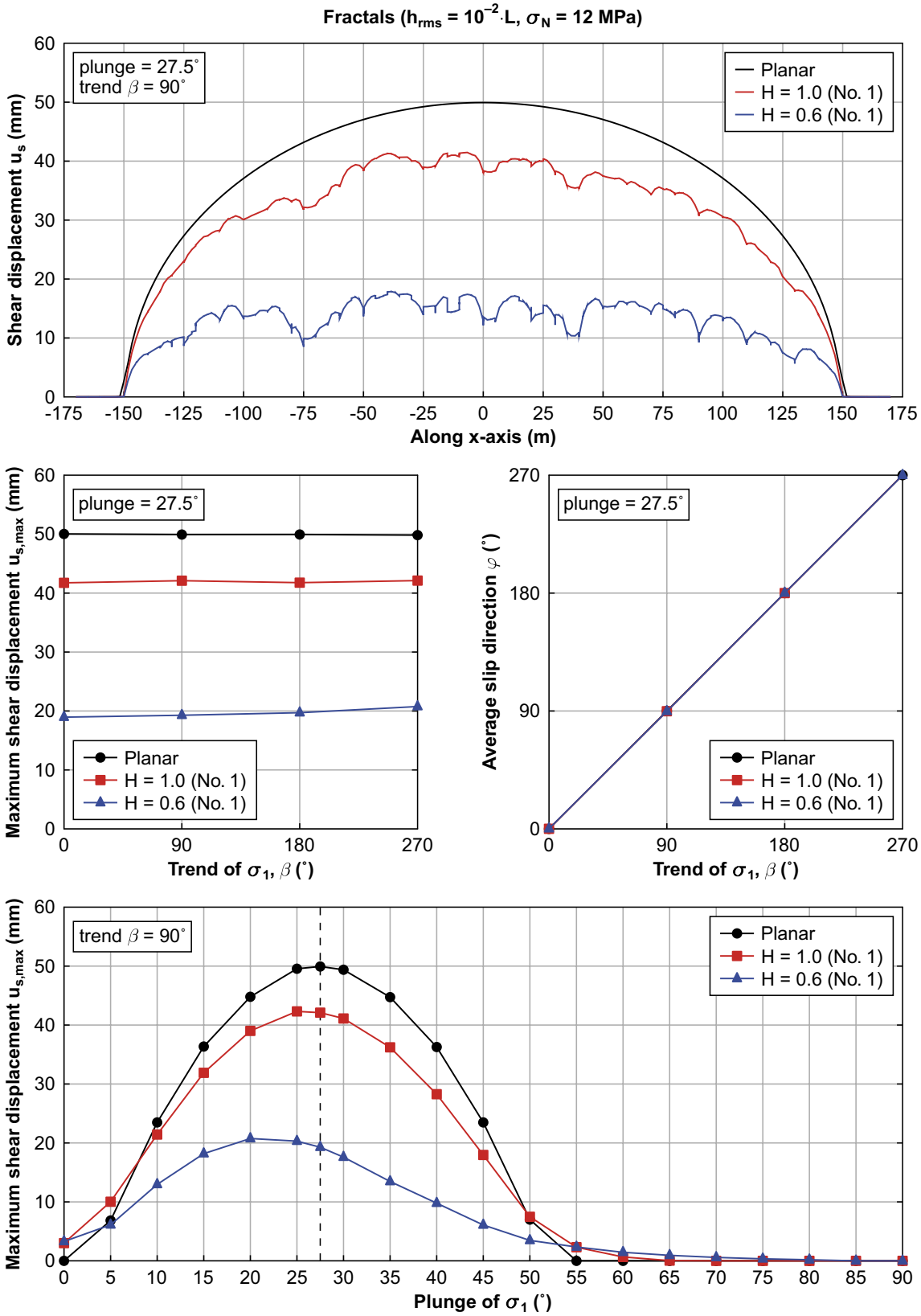

Figure 2-14. *Top: Comparison between the slip distributions along the optimally oriented planar fracture and two fractures with fractal surfaces. Middle left: Maximum shear displacements along the fracture as a function of the trend of the major principal stress. Middle right: Corresponding average slip direction evaluated using Equation 2-11. Bottom: Maximum shear displacements along the fracture as a function of the plunge of the major principal stress with respect to the mean fracture orientation. Note, "No. 1" in the legends indicates the surface realisation that is considered here.*

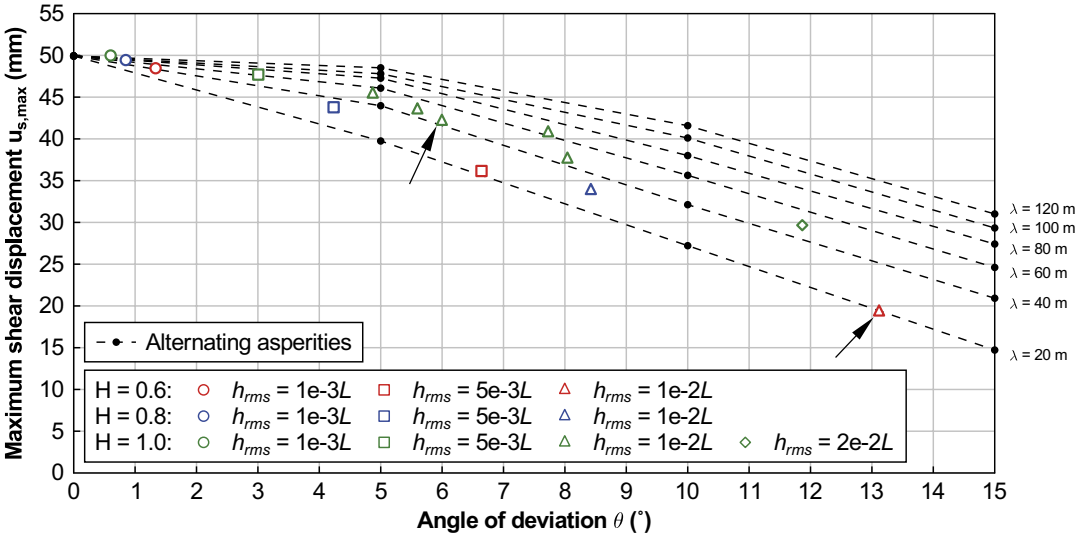

Figure 2-15. *Maximum shear displacements along the synthetic fractures with general fractal roughness as functions of the average angle of deviation. The fractal surfaces are compared with the surfaces with alternating asperities (their wavelengths are indicated in the right margin). Note that for H = 1 and $h_{rms} = 10^{-2}$ L, results for five surface realisations are generated. The two results indicated by arrows correspond to the surface realisations used when generating the results shown in Figure 2-14.*

Influence of stress model

To test if the response of the fractures is different depending on the level of normal stress, four different stress models are tested on fractures with waves and with alternating asperities (cf Figure 2-4):

- very low normal stress (1 MPa),
- low normal stress (6 MPa),
- medium normal stress (12 MPa, base-case), and
- high normal stress (24 MPa).

Figure 2-16 shows, both for the case with alternating asperities and for the case with waves, the maximum shear displacements for each of the tested levels of normal stress. It is observed that the efficiency of the roughness to reduce the maximum shear displacement increases with increasing level of normal stress. As noted earlier, the wavy fracture surface gives larger shear resistance.

Based on the shear displacement results in Figure 2-16, the excess friction angle is calculated according to Equation 2-8 and Equation 2-9. The results are presented in Figure 2-17. For deviation angles less than 15° and with exception for the lowest tested normal stress (1 MPa), the approximation of the excess friction angle with the angle of deviation is reasonable.

It is noted that the excess friction angles in Figure 2-17 are calculated assuming that the normal stress σ_N on the non-planar surface is constant and equal to that on the corresponding planar surface, i.e., $\sigma_N = \sigma^*_N$. This is a schematic assumption, see discussion in Section 2.1.2. To examine how this affects the calculation of the excess friction angle, an estimate is made here of the change in normal stress caused by the dilation on the non-planar surface. The maximum normal displacement is estimated through

$$u_{n,max} = u_{s,max}\, sin(\theta). \tag{2-13}$$

Here, $u_{s,max}$ is the maximum shear displacement on the non-planar fracture (along the direction of the surface segments) and θ is the angle of deviation. The maximum displacement takes place near the centre of the fracture. The correlation between change in normal stress and normal displacement is analogous to the correlation between change in shear stress (stress drop) and shear displacement (cf Equation 2-3 and e.g. Scholz (2002), hence

$$\Delta\sigma_N = \frac{u_{n,max}}{a}\frac{\pi(2-\vartheta)}{8}\frac{G}{(1-\vartheta)}\,. \tag{2-14}$$

By exchanging σ^*_N in Equation 2-8 for $\sigma^*_N + \Delta\sigma_N$, the results in Figure 2-18 are obtained. The agreement with the ideal solution (the black line) is improved considerably as compared to the results in Figure 2-17. For the two lowest normal stress levels the fit with the theoretical solution is very satisfactory for all values of θ, in particular for the case with a wavy surface. For cases with 12 and 24 MPa normal stress, the results deviate from the theoretical solution for larger θ-values when the displacements approach zero (cf Figure 2-16).

It is clear that the calculation of excess friction angle tends to be more sensitive to normal stress changes caused by dilation when the initial normal stress is low. This is because of the larger shear displacements and the associated larger dilation (Equation 2-13). In addition, a lower initial normal stress means that the normal stress change has a larger relative importance.

The results in this section indicate that the 3DEC results agree well with the findings by e.g. Patton (1966) that the excess friction angle is approximately equal to the angle of deviation. The agreement is good for a range of normal stress assumptions. It has also been demonstrated that the estimate of the excess friction angle on a fracture is improved considerably if the normal stress increase caused by dilation is considered in the calculation.

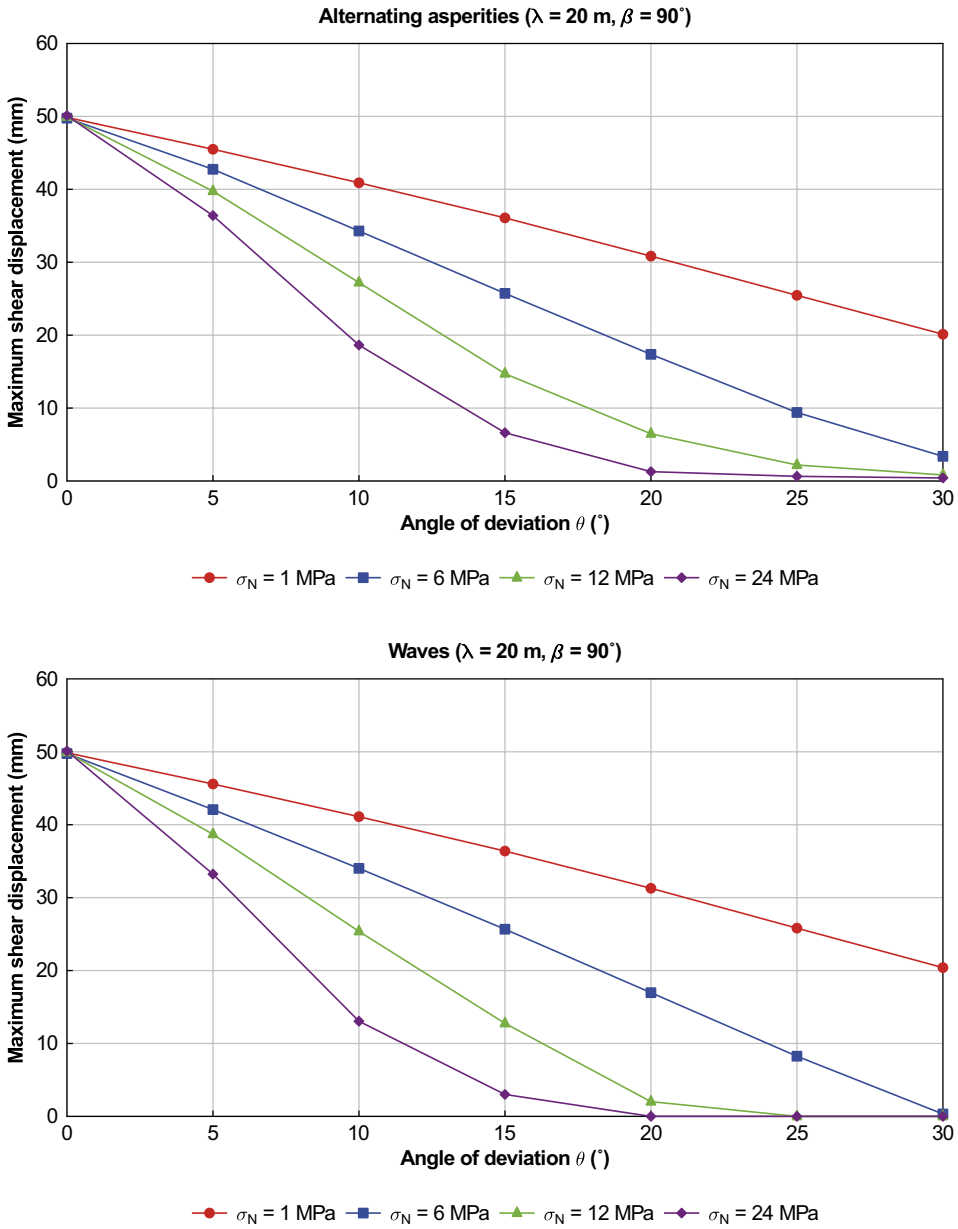

Figure 2-16. *Maximum shear displacement on fractures with alternating asperities (upper) and with waves (lower) (wavelength of 20 m) for different levels of normal stress.*

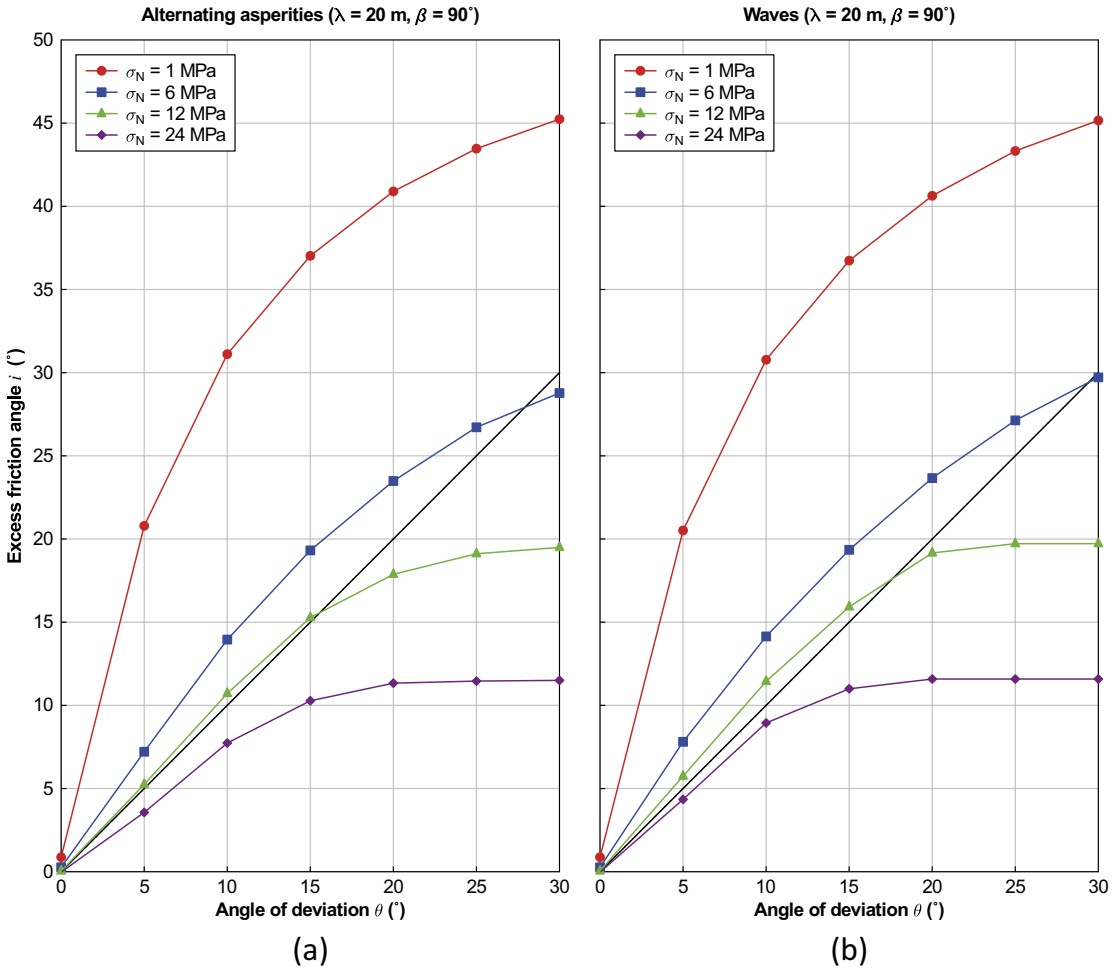

Figure 2-17. *Calculated excess friction angle (Equation 2-9) for each of the fractures with (a) alternating asperities and with (b) waves with a wavelength of 20 m subjected to different levels of normal stress. The black diagonal line indicates the case for which the excess friction angle is equal to the angle of deviation.*

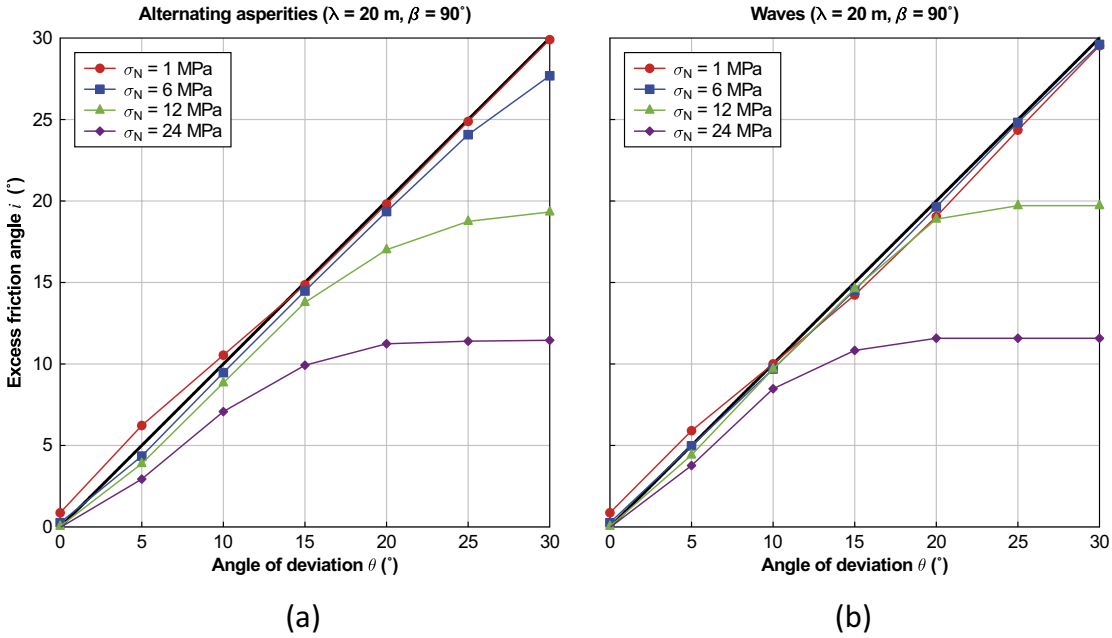

Figure 2-18. *Excess friction angles corresponding to those in Figure 2-17, but here the change in normal stress has been estimated according to Equation 2-14. The black diagonal line indicates the case for which the excess friction angle is equal to the angle of deviation.*

Relevance of continuum model

When generating the results that are presented in the preceding sections, the rock was assumed to have infinite strength. During shearing, the stresses in the most highly stressed parts (tips) of the asperities may be high enough that failure is initiated. The potential for failure and the influence on the maximum fracture shear displacements are investigated using the base-case stress model (see Figure 2-4c). Failure is simulated in two different ways:

1. The rock mass surrounding the fracture is assumed to respond to loading according to a Mohr-Coulomb elasto-plasticity model with brittle tension cut-off (i.e., the tensile strength is reduced to zero after tensile failure has occurred). The strength parameters (shear and tensile) are set at values corresponding to intact rock (Glamheden et al. 2007), cf Table 2-2.
2. 25 % of the amplitude of the asperities is removed, thus creating voids around the sharp bends (Figure 2-19).

In both cases, the results are compared with results from corresponding linear elastic models. The results are shown in Figure 2-20. For the planar case and for 5° deviation angle, the Mohr-Coulomb case gives slightly increased displacements as compared to the linear elastic case. This can be attributed to failure of the rock around the edges of the fracture, see Figure 2-21. The tips of the asperities stay intact, as is indicated by the no-tip case, which gives results that are practically identical to the linear elastic base case. This also indicates that, even though the tips are highly stressed, their contribution to the shear resistance is small. The small contribution can be attributed to the fact that the volume of the tips constitutes a small fraction of the total asperity volume. For the larger deviation angles, all three cases give similar results, thus indicating that the linear elastic assumption is relevant also for these angles.

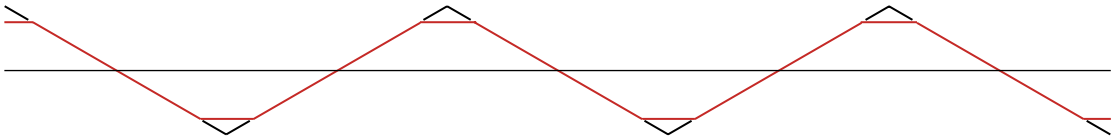

Figure 2-19. *The effect of removing 25 % of the amplitude of the asperities, cf Figure 2-2.*

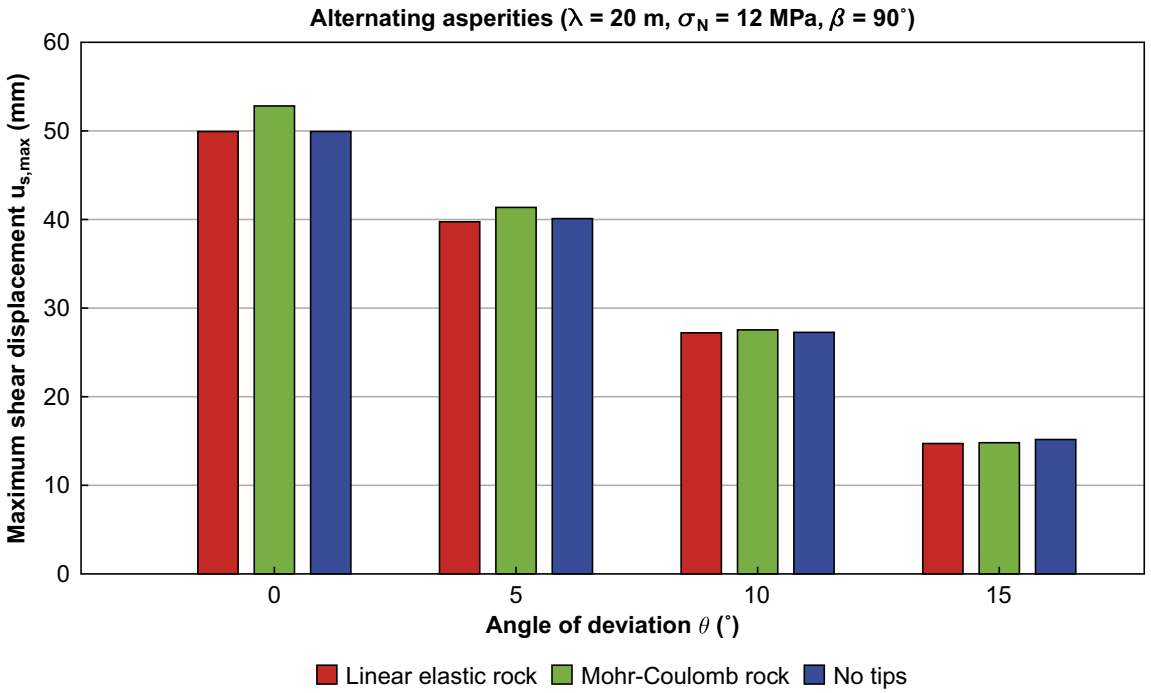

Figure 2-20. *Comparison between the maximum shear displacement along a fracture with alternating asperities embedded in linear elastic rock, in Mohr-Coulomb rock, or in linear elastic rock and with the tips of the asperities removed. Note that for the planar case (angle of deviation = 0°), the results for the "linear elastic"-case and the "no tips"-case are obtained from the same model.*

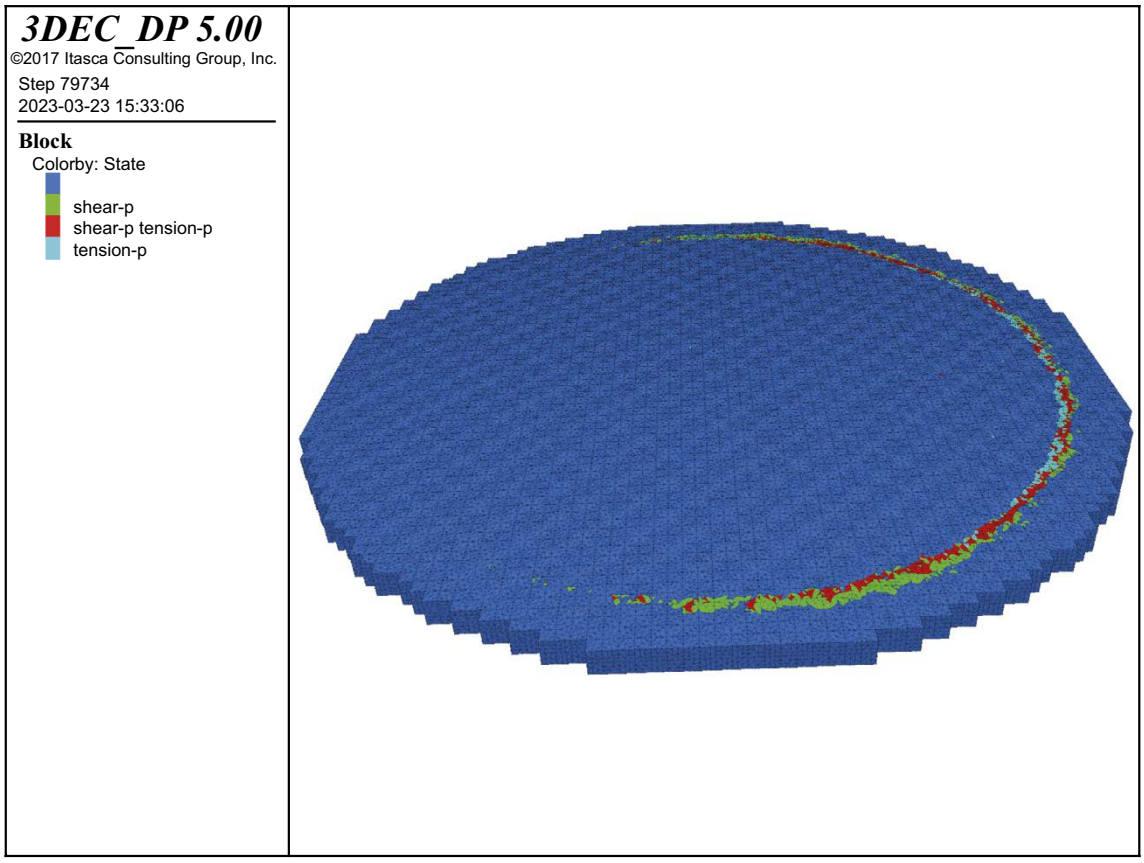

Figure 2-21. *One side of the fracture after shearing in the case with angle of deviation $\theta = 5°$ and Mohr-Coulomb rock. The colour scale indicates the failure state of the finite difference zones. Dark blue means no failure, i.e., the zone is still in its elastic state. The figure shows that failure has taken place only along the edge of the fracture.*

2.2 Non-mated fracture surfaces

2.2.1 General

All results presented in Section 2.1 were generated with models where the fracture surfaces were in perfect contact. This is not necessarily the case for real rock fractures, which may have gone through several episodes of movements and weathering of the surfaces. A fracture that has mis-matched surfaces or contains soft filling materials may permit larger shear displacements than perfectly mated ones. The calculations presented in this section aim at addressing this issue.

2.2.2 Stress models and calculation sequence

For a mated fracture with high stiffness, the approach used to simulate shearing that was applied in the previous sections of this report is equivalent to starting from an arbitrary state of stress below the strength envelope and subsequently ramping up the stresses to the final state (see e.g., Figure 2-4c). A fracture with mis-matched surfaces (or containing a soft filling material) may, however, be compressed during shearing, which could "possibly allow for significant displacements along the fracture mean plane" (Lönnqvist and Hökmark 2015a). Hence, the calculations presented in this section were performed in two steps and two loading paths were considered.

- For the first calculation step, two initial (background (BG)) stress tensors are constructed with principal stress magnitudes chosen such that the optimally oriented planar fracture is exactly at the stability-limit initially (Figure 2-22). The normal stress is set either 5 MPa lower than the final one (σ_N = 7 MPa, denoted *loading* (L) in the following) or 5 MPa higher than the final one (σ_N = 17 MPa, denoted *unloading* (UL) in the following) (blue Mohr circles in Figure 2-22). During this step, the model boundaries are locked in all directions to avoid unwanted shear displacements on the model boundaries. Whereas all non-planar and perfectly mated fractures will be stable by some margin, the fractures with explicitly defined aperture-variations may slip, open or close in response to stress redistribution effects around the voids. These displacements are set to zero before the main shearing calculation step starts.
- During the second calculation step, the stresses are ramped up to the final state (red Mohr circles in Figure 2-22) by controlling the movements of the model's boundaries in the *x*-, *y*- and *z*-directions.

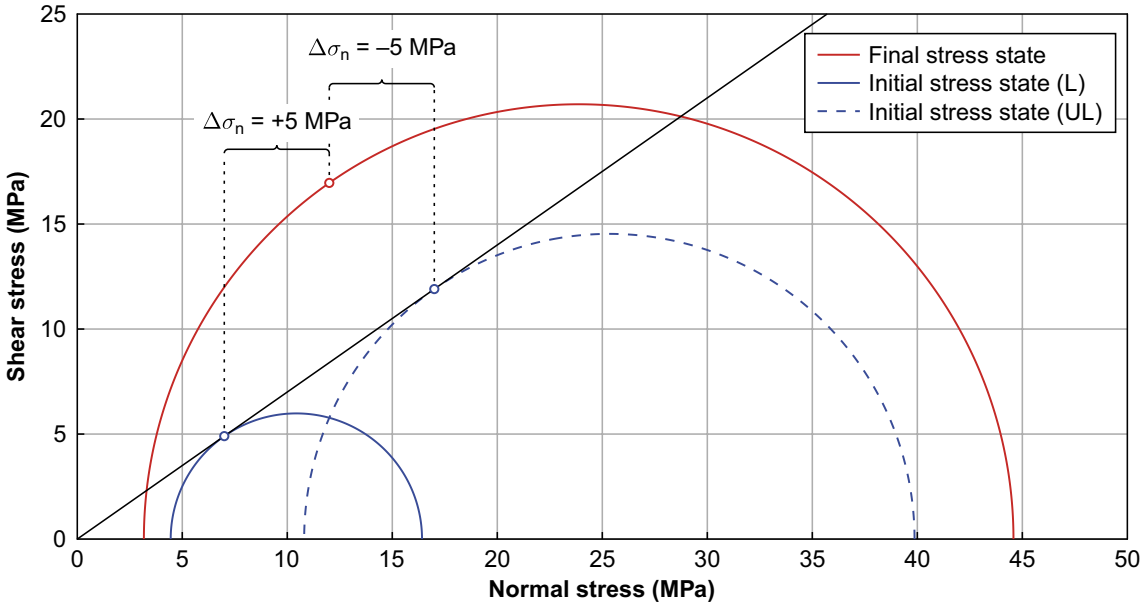

Figure 2-22. *Mohr-circle representations of the stress states. The intermediate principal stress σ_2 is 0.5 × (σ_1 + σ_3) in both cases.*

2.2.3 Normal stiffness variation on mated fracture

As a first approximation, the influence of the degree of mis-match and of fracture filling material is schematically modelled by changing the fracture's normal stiffness on a mated fracture, i.e., the type of fracture considered in Section 2.1. Table 2-3 shows a compilation of estimated ranges of variation in the normal stiffness of fractures (obtained from lab-scale tests) and deformation zones at the Forsmark site (Glamheden et al. 2007, Tables 4-15 and 5-7). Excluding the 30 km long Singö deformation zone, which is not of relevance to the problem considered here, the stiffnesses of the deformation zones are on average about one order of magnitude lower than that of individual fractures.

Table 2-3. Range of variations in normal stiffness of fractures and deformation zones at the Forsmark site, compiled from Glamheden et al. 2007 (Tables 4-15 and 5-7).

Discontinuity type	Normal stiffness (GPa/m)
Fractures (FFM01)	159 – 1 833
Deformation zones (excl. Singö deformation zone)	78–90
Singö deformation zone	0.2

To test to what extent the normal stiffness could affect the maximum shear displacement, four different values of the normal stiffness, k_n are considered[2]: 656 GPa/m (base-case value, see Table 2-2), 65.6 GPa/m, 6.56 GPa/m, and 0.656 GPa/m. Figure 2-23 shows the maximum shear displacement for each of the four tested stiffnesses. The results suggest that the normal stiffness needs to be reduced from the base-case value (656 GPa/m) by between one and two orders of magnitude before any substantial impact on the maximum shear displacements can be observed. Except for the lowest tested stiffness-value (0.656 GPa, which is comparable to that of the Singö deformation zone, cf Table 2-3), the increase in shear displacement is modest. The relative difference becomes larger with increasing deviation angle. For 15° deviation angle, when reducing the stiffness from the base case value to 65.6 GPa/m, which is the value relevant for deformation zones at Forsmark, the displacement increases by about 10 %. For 5° deviation angle, the corresponding increase becomes about 3 %. This holds for both stress paths.

In the following subsections, the 3DEC model used for simulating displacements on fractures with explicitly modelled initial apertures is described and the results from those simulations are presented.

[2] Note that the base-case stiffness is used in all models during the initial equilibrium state to ensure that the starting point is identical for all models. The stiffness is then changed prior to ramping up the stresses to the final state.

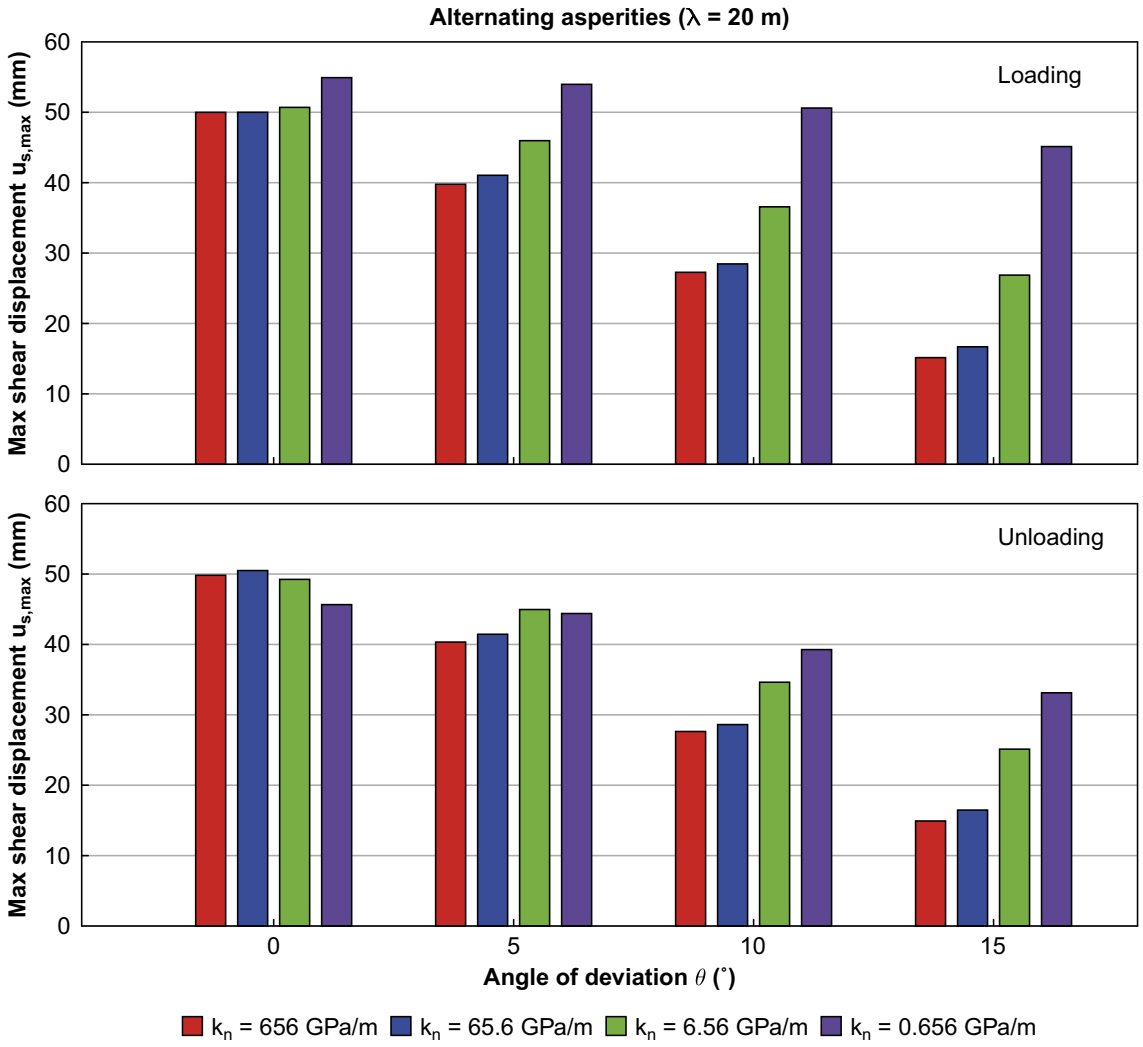

Figure 2-23. *Influence of normal stiffness on the maximum shear displacement with varying angle of deviation.*

2.2.4 Non-mated fracture 3DEC model description

The numerical model consists of a cube with side-length 1 600 m in which an isolated fracture with radius 150 m is included (Figure 2-24). The mean fracture plane is horizontal. The circular shape of the fracture is obtained by assignment of fracture properties within a circular region on the fracture plane. The fracture surfaces (cf Section 2.1.1) are constructed from convex blocks with triangular faces where the shortest side-length is 5 m. For the resolution considered here, the fracture surfaces consist of about 5 600 triangular sub-surfaces. The model is discretized with tetrahedral finite-difference elements with edge-lengths ranging from 1.8 m surrounding the fracture to 53 m near the model's boundaries.

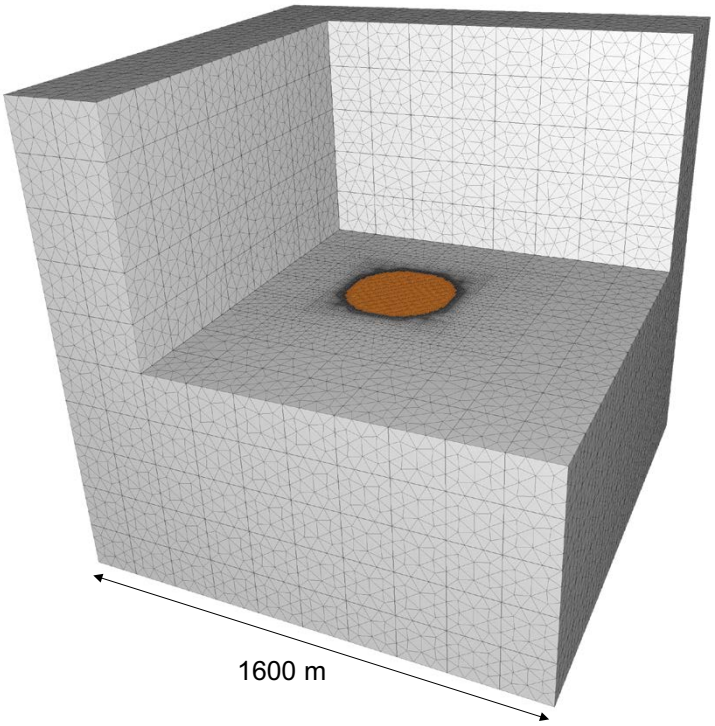

Figure 2-24. *Illustration of a 3DEC model with a non-planar and mis-matched fracture (marked in orange; alternating asperities, θ = 10°, λ = 40 m). Note that parts of the model are hidden to expose the fracture surface.*

The generic surface type with isotropic roughness denoted "alternating asperities" (see Section 2.1.1) is used. The wavelength is 40 m and angles of deviation in the range 0° to 15° (see Figure 2-25a and b) are considered. Following the terminology used by Ritz and Pollard (2012), positive slopes (assuming right-lateral shearing, cf Figure 2-25a) are referred to as "stoss"-sides and negative slopes as "lee"-sides. Initial maximum apertures (defined as the perpendicular distance between two matching triangular sub-surfaces) are 0 mm (perfectly mated fracture, Figure 2-25b), 10 mm, 20 mm, 50 mm, 100 mm and 200 mm. The distributions of the apertures are as follows (see also Figure 2-25c–f):

- One opening at the centre of the fracture (sub-figure c). The opening is located either on the lee-side or on the stoss-side of the corrugations.
- All lee-sides or, alternatively, all stoss-sides are open (sub-figure d).
- All side-slopes (*i.e.*, fracture segments with dip direction perpendicular to the main shearing direction) are open (sub-figure e).
- The surfaces are not in contact anywhere (sub-figure f). Note that openings of this kind cannot exist under the assumed background stress conditions. This case is included here for completeness.

The constitutive laws assigned to the continuum and the fractures are the same as those applied in the calculations presented earlier in this report, i.e., the continuum is linear elastic, and the fractures respond according to the ideal elasto-plastic law (see Section 2.1.1). The material property parameter values are according to the base case values in Table 2-2.

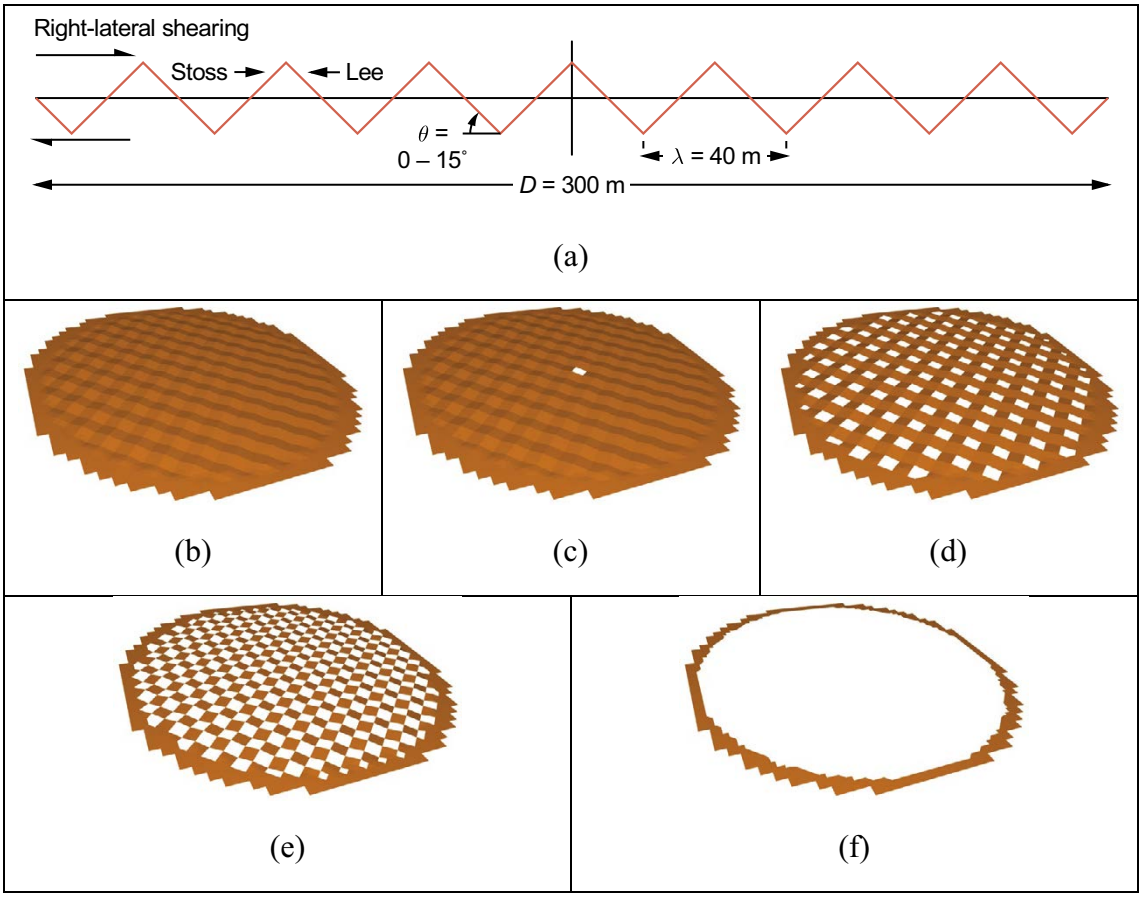

Figure 2-25. *Illustrations of fracture surface geometries: (a) cross-section geometry of the mated fracture (not to scale), (b) perfectly mated fracture, (c) one opening at the centre of the fracture (either on the lee-side or on the stoss-side), (d) openings on all lee-sides or, alternatively, all stoss-sides, (e) openings on all side slopes, and (f) no contact between the surfaces anywhere.*

2.2.5 Calculation of relative displacements

3DEC calculates relative displacements automatically when a fracture's surfaces are in contact with each other. For fractures with mis-matched surfaces, the relative displacements need to be evaluated from the displacement vectors on the block surfaces. To do so, a *FISH*-routine has been developed that (1) maps the triangular sub-surfaces (in the original block structure) on the top and bottom surfaces of the fracture, (2) finds the average normal vector associated with each pair of sub-surfaces, and (3) calculates the shear displacement magnitude associated with each pair of triangular sub-surfaces. The magnitude of the shear displacement for each pair of triangular sub-surfaces is given by (cf Figure 2-26)

$$u_{s,Tri} = \left| \left(\underline{u}_{Top} - \underline{u}_{Bottom} \right) - \left[\left(\underline{u}_{Top} - \underline{u}_{Bottom} \right) \cdot \underline{n}_{Average} \right] \underline{n}_{Average} \right| \tag{2-15}$$

where $\underline{u}_{Top}$ and $\underline{u}_{Bottom}$ are the average displacement vectors on the top and bottom surface (calculated from the gridpoints associated with the zone faces on each rigid triangular face), respectively, and $\underline{n}_{Average}$ is the average normal vector of the sub-surface pair.

2.2.6 Results

Small-strain versus large-strain analysis

3DEC has two calculation modes (Itasca 2020), small-strain mode and large-strain mode. Analyses performed in large-strain mode can be considered more accurate but come at increased computational complexity (Itasca 2020). In small-strain mode, the model does not physically deform when subjected to different types of loading. Furthermore, the contact between two touching fracture surfaces cannot be lost and new contact areas cannot be formed. This is an acceptable approximation when the shape of the deformed tetrahedral zones do not differ by more than a few percent from the original ones (Itasca 2020) and for "jointed systems that are initially closely-packed" (Lemos 2008).

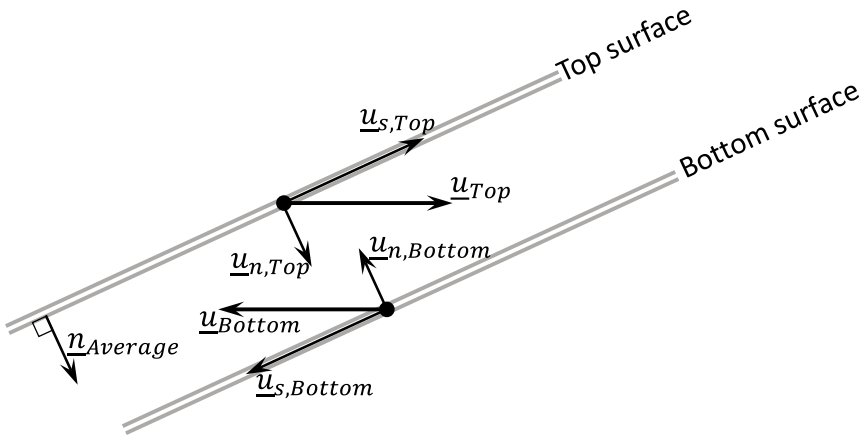

$$u_{s,Tri} = \left| \underline{u}_{s,Top} - \underline{u}_{s,Bottom} \right| = \left| \left(\underline{u}_{Top} - \underline{u}_{n,Top} \right) - \left(\underline{u}_{Bottom} - \underline{u}_{n,Bottom} \right) \right| =$$

$$= \left| \left[\underline{u}_{Top} - \left(\underline{u}_{Top} \cdot \underline{n}_{Average} \right) \underline{n}_{Average} \right] - \left[\underline{u}_{Bottom} - \left(\underline{u}_{Bottom} \cdot \underline{n}_{Average} \right) \underline{n}_{Average} \right] \right| =$$

$$= \left| \left(\underline{u}_{Top} - \underline{u}_{Bottom} \right) - \left[\left(\underline{u}_{Top} - \underline{u}_{Bottom} \right) \cdot \underline{n}_{Average} \right] \underline{n}_{Average} \right|$$

Figure 2-26. *Derivation of the shear displacement magnitude $u_{s,Tri}$ for a pair of sub-surfaces.*

The results presented in Section 2.1 indicate that 3DEC is able to reproduce the theoretical slip distribution (Segedin 1951) along planar fractures and to generate slip distributions along mated fractures with generic deviations from planarity that are logical and consistent with input assumptions in small-strain mode. To assess if shear displacements along mis-matched fractures also can be adequately captured by 3DEC-models analysed in small-strain mode, a fracture with openings located on all stoss-sides (cf Figure 2-25d) is analysed both in small-strain mode and in large-strain mode and the results are compared. The following is observed (see Figure 2-27):

- When the surfaces are perfectly matched (initial maximum aperture = 0 mm), the two methods yield the same results.
- For mis-matched surfaces, i.e., when the surfaces initially are not in contact with each other everywhere, a 3DEC-model analysed in small-strain mode cannot capture the increased resistance when the two surfaces come into contact with each other during the shearing process (i.e., the code cannot determine the size of the openings) and yields approximately the same maximum shear displacement regardless of initial aperture. In the models analysed in large-strain mode, the maximum shear displacement increases with the maximum initial aperture. For maximum initial apertures of 50 mm or greater, models analysed in small-strain mode and in large-strain model yield the same maximum shear displacements.

It can be concluded that large-strain analyses are necessary when a fracture is not perfectly mated. All subsequent analyses where initial apertures are explicitly modelled are, therefore, performed in large-strain mode.

Opening at the centre of a fracture

Figure 2-28 shows the case with a single void located at the centre of the fracture (cf Figure 2-25c). The response of this type of surface can be summarized as follows:

- A single void that is located on a lee-side of an asperity at the centre of the fracture does not influence the maximum shear displacements.
- If the void is located on a stoss-side, the void has a small-to-modest influence on the shear displacements (increased displacements in the order of a few millimetres compared with the perfectly mated fracture).
- The two load paths yield similar results.

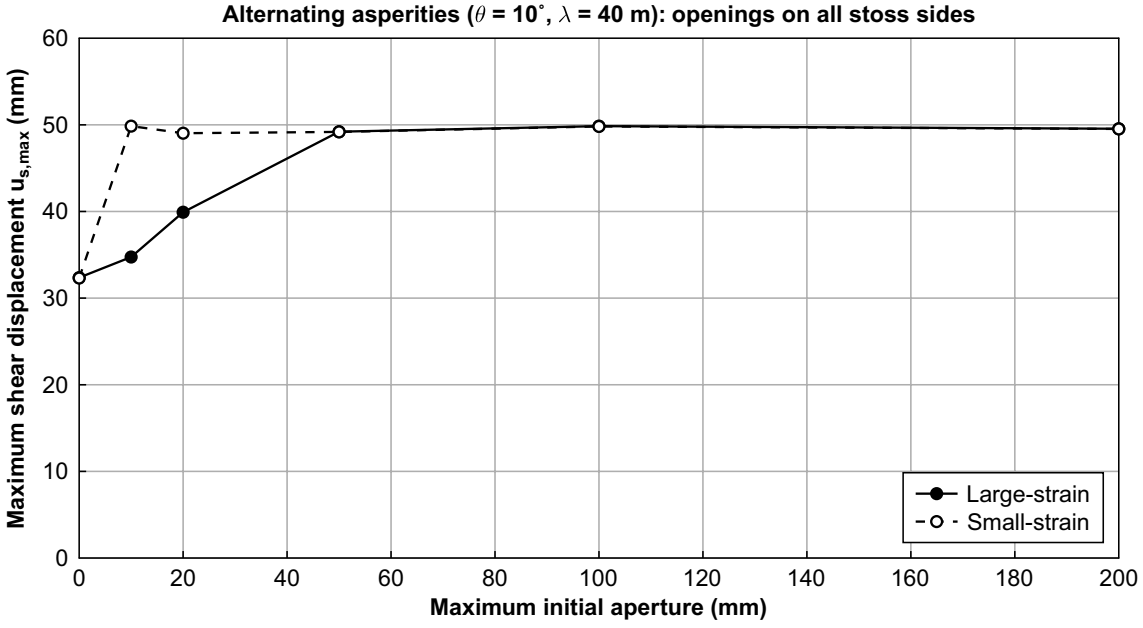

Figure 2-27. *Example of the maximum shear displacements along a non-planar fracture with mis-matched surfaces analysed in small-strain mode and in large-strain mode, respectively.*

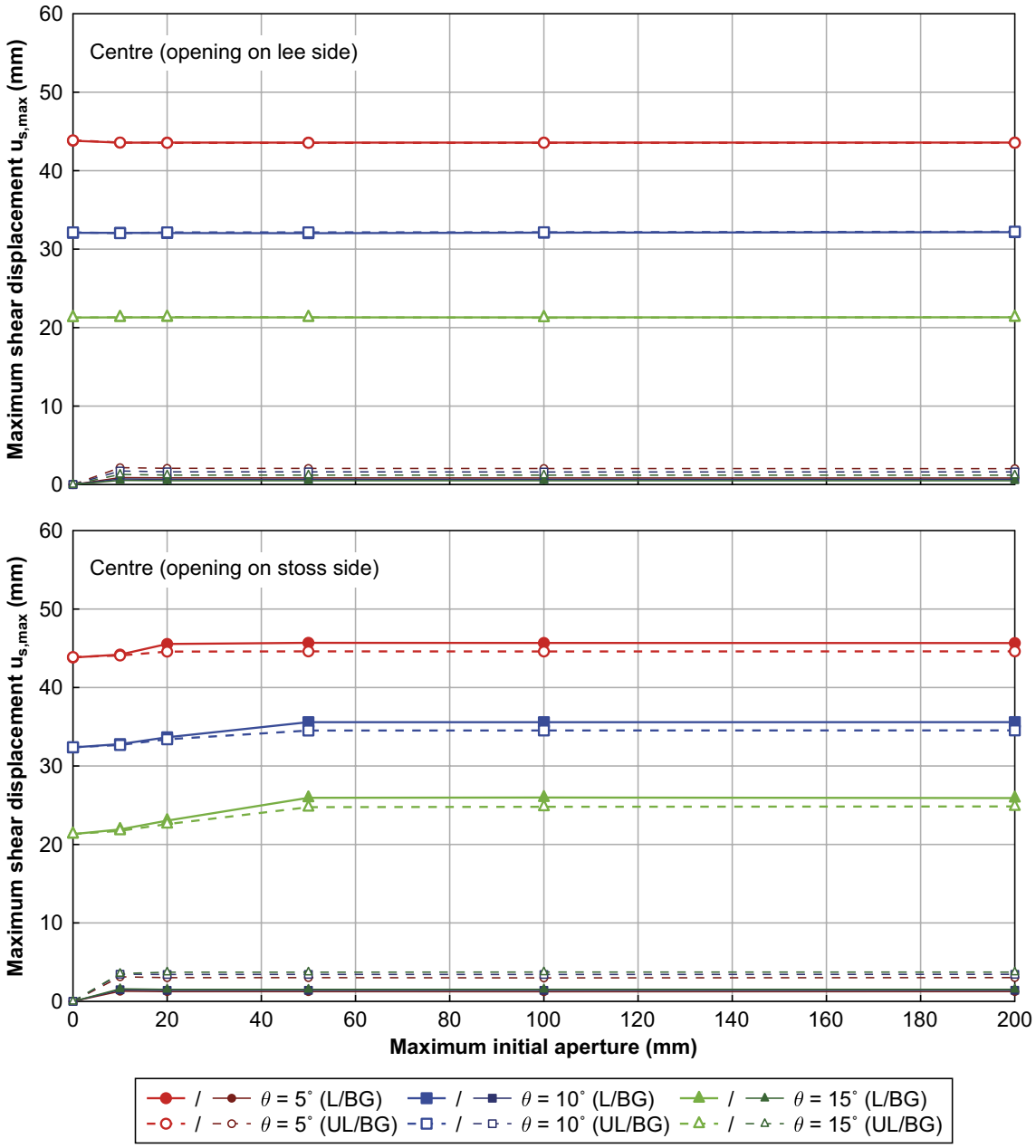

Figure 2-28. *Maximum shear displacements along a fracture with an opening at the centre on a lee-side (top) and on a stoss-side (bottom). Slip magnitudes shown in darker colour represent shear displacements that have occurred in response to the background ("BG") stress-field (i.e., during the first calculation step). Note, "L" and "UL" denote "Loading" and "Unloading, respectively (see Section 2.2.2).*

Openings on all lee- or stoss-sides

Figure 2-29 shows the case with voids systematically located on either all lee-sides or on all stoss-sides. The response of this type of surface can be summarized as follows:

- As for the fractures with a single void, there is an insignificant impact on the shear displacements if the voids are located on the lee-sides of the corrugations.
- For fractures with voids located on all stoss-sides, the voids have a considerable impact on the shear displacements. The increase in displacement compared with the mated fracture case amounts to a few millimetres for the smallest initial aperture to a few tens of millimetres for apertures > 50 mm. The impact becomes larger for larger angles of deviation.
- The two load paths yield similar results.

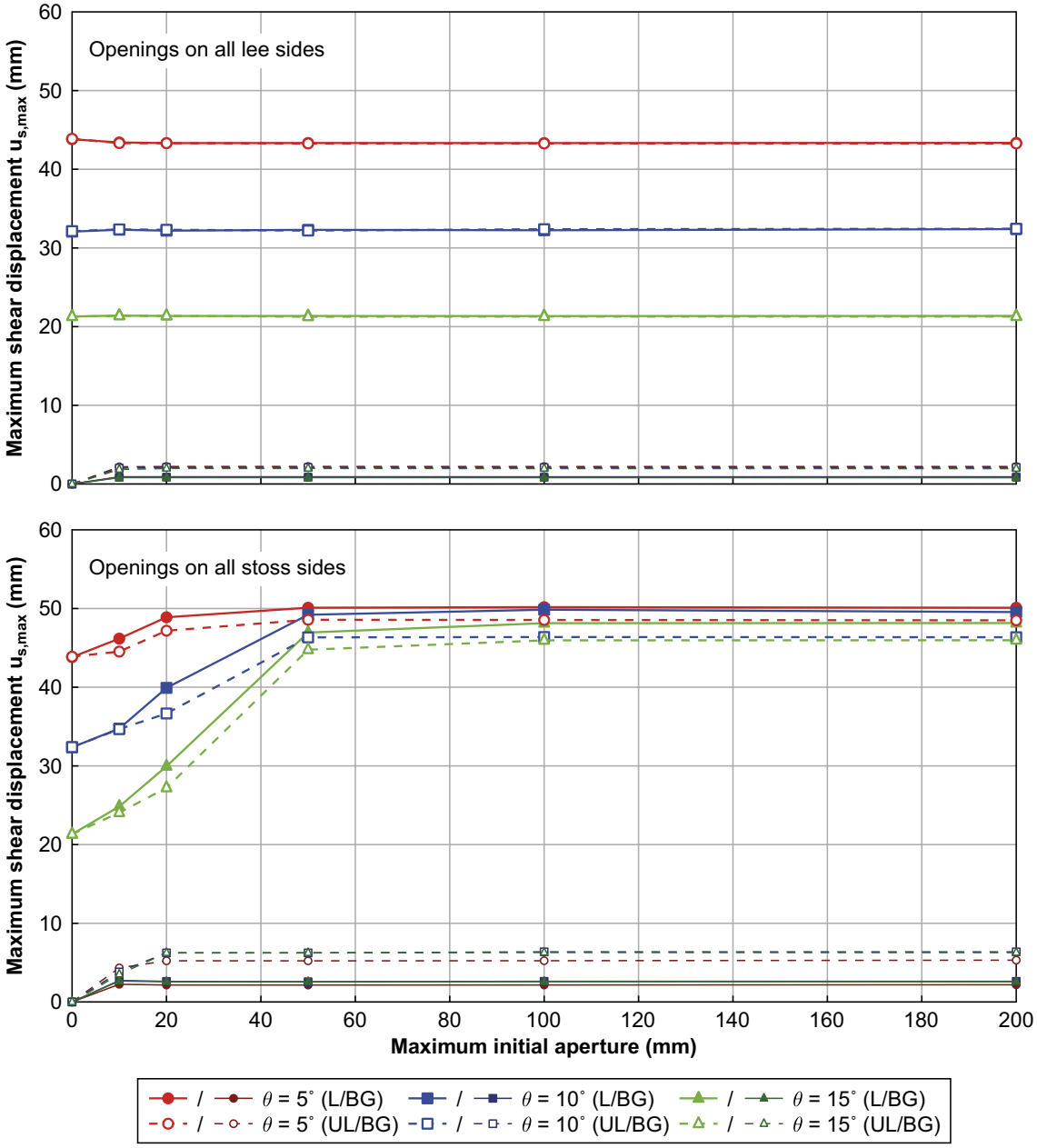

Figure 2-29. *Maximum shear displacements along a fracture with openings on all lee-sides (top) and on all stoss-sides (bottom). Slip magnitudes shown in darker colour represent shear displacements that have occurred in response to the background ("BG") stress-field (i.e., during the first calculation step). Note, "L" and "UL" denote "Loading" and "Unloading, respectively (see Section 2.2.2).*

Openings on all side slopes

Figure 2-30 shows the case with voids systematically located on all side-slopes. For this type of surface, the voids tend to have an insignificant impact or tend to reduce the maximum shear displacement compared with the mated fracture. The reduction in displacement may appear counterintuitive but can be attribute to the fact that the side slope surfaces are aligned with the shearing direction. Hence, relative to the stoss-sides they contribute only to a minor extent to the shear restriction imposed by the asperities. However, as the side slope surfaces are left open, the normal load is redistributed to the stoss-sides (the normal load on the lee-sides become practically zero during shearing), with increased shear resistance as a consequence.

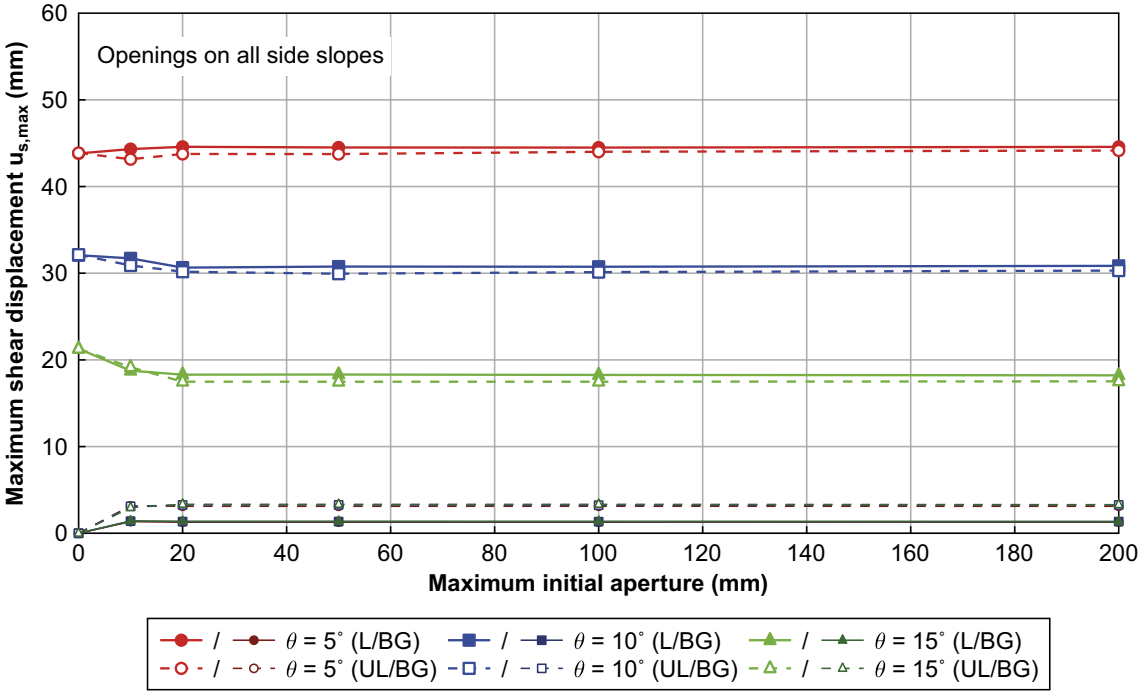

Figure 2-30. *Maximum shear displacements along a fracture with openings on all side slopes. Slip magnitudes shown in darker colour represent shear displacements that have occurred in response to the background ("BG") stress-field (i.e., during the first calculation step). Note, "L" and "UL" denote "Loading" and "Unloading, respectively (see Section 2.2.2).*

No initial contact between the fracture surfaces

Here, results from the models with no initial contact between the fracture surfaces are presented. It should be pointed out that openings of this kind cannot exist under the assumed background stress conditions. The results are included here for completeness.

The results are presented in Figure 2-31. For initial apertures of up to about 20 mm, contacts between the fracture surfaces on the stoss-sides and on the side slopes are established during the first calculation step when the background (BG) stress field is applied. Then during the second calculation step, the response of these fractures is approximately the same as for the fractures with openings on all lee-sides (cf Figure 2-29, upper). However, as the initial aperture is increased further, the response becomes significantly different. For instance, in the "Loading"-case (L), no contacts between the fracture surfaces are established during the first calculation step for apertures ≥ 50 mm. This means that the maximum displacement is not restricted by the surface properties but by the rock properties and the strain energy that is available for the applied stress field. That is why there is a plateau in the "Loading"-case curves for apertures ≥ 50 mm in Figure 2-31, lower. During the second calculation step, in which additional loading is applied, contacts are established, but only for initial apertures up to 100 mm. Hence, there is a plateau in the "Loading"-case curves for apertures ≥ 100 mm in Figure 2-31, upper.

In the "Unloading"-case (UL), the higher initial shear stress (cf Figure 2-22) yields larger initial displacements than the "Loading"-case (Figure 2-31, lower). Then during the second calculation step, the shear stress increase is lower than in the "Loading"-case (Figure 2-22). This, in combination with the normal stress reduction, gives smaller displacements than for the "Loading"-case.

It can be noted that counterintuitive results are generated in cases with large initial apertures, with smaller displacements for smaller angles of deviation. This arises in situations when no contact between the surfaces is established. Hence, changes in the surface geometry have no impact on the shear resistance and on the resulting continuum displacement field (as noted above). However, the calculated shear displacements (cf Section 2.2.5) are determined by the orientations of the surface segments (i.e. angle of deviation) relative to the displacement field. Here, this results in calculated shear displacements that are smaller for smaller angles of deviation.

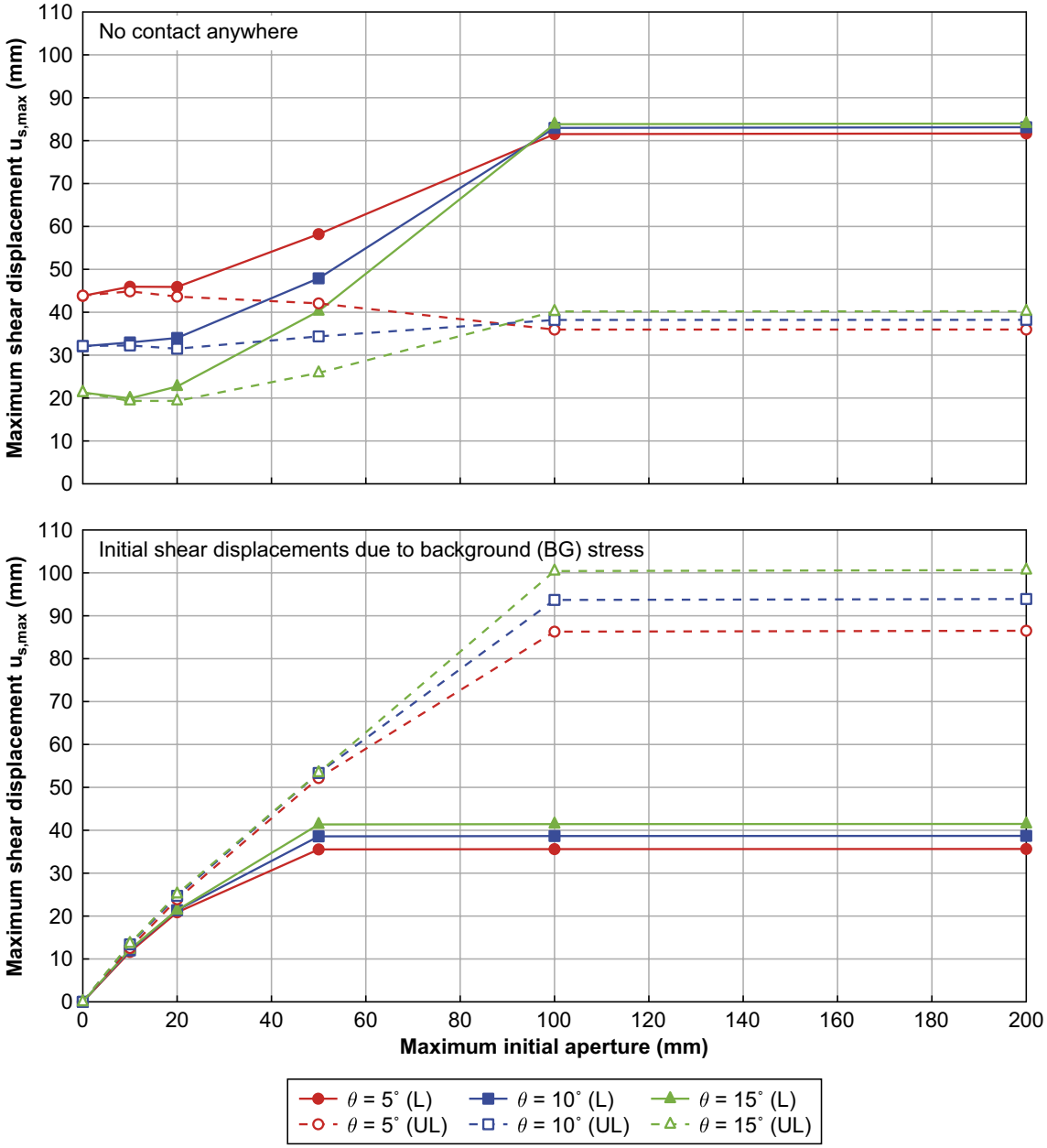

Figure 2-31. *Upper: Maximum shear displacements along a fracture with no initial contact between the surfaces. Lower: Shear displacements that have occurred in response to the background ("BG") stress-field (i.e., during the first calculation step. Note, "L" and "UL" denote "Loading" and "Unloading, respectively (see Section 2.2.2). Also note the difference in y-axis scale compared with Figures 2-28 to 2-30.*

Influence of fracture orientation

As shown in Section 2.1, a mated fracture with "alternating asperities", with a friction angle ϕ and an angle of deviation θ, will have an effective friction angle that is approximately equal to $\phi + \theta$. As noted above, the optimal plunge angle of the major principal stress relative to the average fracture plane would then be $45° - (\phi + \theta)/2$. This, however, may not necessarily be the optimal orientation for a non-planar fracture with aperture variations (note that the plunge was assumed to be 27.5° in all calculations previously presented in this results section). Figure 2-32 shows the maximum shear displacement as a function of the plunge angle for the mated fracture with $\theta = 10°$ and for two corresponding mis-matched surfaces with maximum initial apertures of 20 mm or 100 mm located either on all lee-sides or on all stoss-sides. The following is observed:

- Voids located on all lee-sides have an insignificant impact on the shear displacements, and the fracture responds to loading approximately as the mated fracture for all tested plunge-angles.

- The optimal plunge-angle for mis-matched fractures with voids located on all stoss-sides appears to be slightly higher than the theoretical one (≈ 22.5°). This would be consistent with a larger shear displacement and an effectively smaller friction angle on a non-mated fracture.

Even if only one case of deviation angle θ is tested here, it appears that the model generates results that are consistent with the input assumptions. Openings or soft fracture fillings allow for larger shear displacement as compared to those generated on the corresponding mated fracture. This gives a reduction of the effective fracture shear strength and a larger optimal plunge angle.

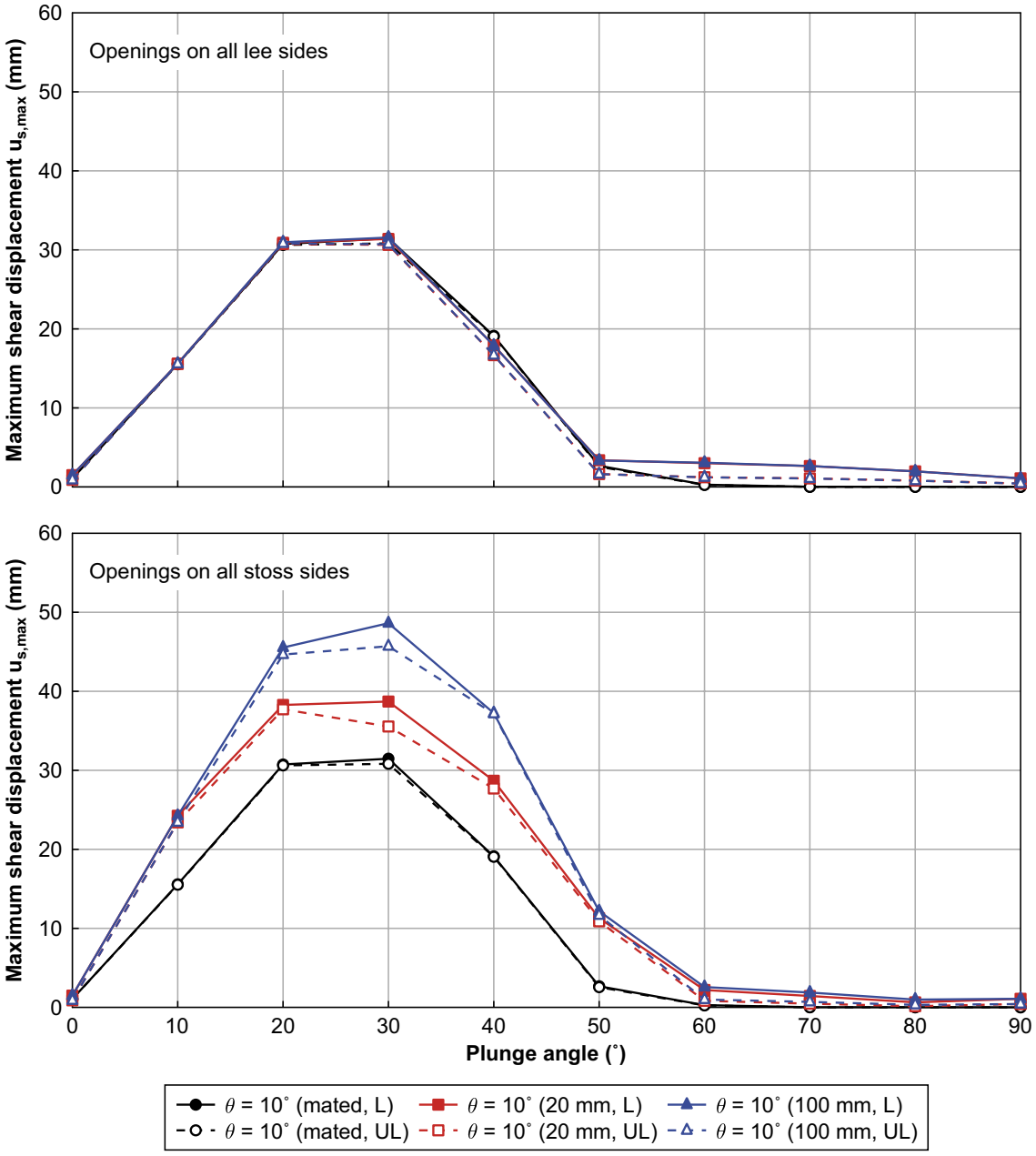

Figure 2-32. *Maximum shear displacements along the fracture as a function of the plunge of the major principal stress with respect to the mean fracture orientation for mated fractures and for mis-matched fractures with voids located on all lee-sides (top) and on all stoss-sides (bottom). The results for the mated fracture are the same in both sub-figures. Note, "L" and "UL" denote "Loading" and "Unloading, respectively (see Section 2.2.2).*

3 Dynamic earthquake loading

In this chapter, a sub-set of the previously analysed models are selected for dynamic analyses to determine if there are systematic and important differences in the mechanical response of a non-planar fracture to quasi-static and dynamic loading, respectively. The case considered here represents the case that is of concern for the long-term safety of the repository at Forsmark, i.e., that of co-seismic near-fault secondary fracture displacements.

3.1 Description of models

Since dynamic models can be very time-consuming, the modelling work presented here is conducted using so-called nestling. This approach, whereby some quantity (e.g., displacements) is extracted from the interior of a large-scale model and used as a boundary condition for a more detailed near-field model, has been adopted in several previous studies for quasi-static analyses (e.g. Hökmark et al. 2010, Lönnqvist and Hökmark 2015b, Suikkanen et al. 2016). The approach has been shown to be a reasonable approach also in dynamic analyses (Lönnqvist et al. 2019). The large-scale and near-field models used here are described in the following. It is recalled here that 3DEC v 5 is used for the large-scale model and for the near-field models with matched fracture surfaces. For the near-field models with explicitly modelled fracture apertures, 3DEC v 7 is used.

3.1.1 Large-scale model

Geometry

The model comprises a box that extends 21 km in the *x*-direction, 34 km in the *y*-direction and 11 km in the *z*-direction (Figure 3-1, left). The upper boundary of the model represents the ground surface. A gently dipping and surface-breaching joint plane that represents an earthquake fault (the primary fault) is included centrally in the model volume. The plane has 4 km length along strike, 5 km down-dip width and dips 30° with respect to the horizontal (Figure 3-1, middle). Given the stress-field (cf following section) the shallow dip angle means that it is possible to obtain low fault stability at all depths using realistic fault strength parameter values and thereby propagate an earthquake rupture over the entire fault plane. The hypocentre is located centrally with respect to the fault strike and at 4.5 km down-dip distance.

Two joint planes are inserted in the vicinity of the primary fault plane. One of the joint planes is located in the hanging wall and the other is located in the footwall (Figure 3-1, middle and right). Both planes have dip angle 27.5° and dip-direction parallel to the positive *y*-axis. Within a circular area on their respective plane, fracture properties are assigned such that circular target fractures with 150 m radius are formed. The centres of the fractures are located at 500 m depth and at 200 m perpendicular distance from the primary fault plane.

The target fractures are surrounded by a volume that extends 1 730 m, 800 m, and 900 m in the *x*-, *y*- and *z*-directions, respectively (Figure 3-1, right). The primary fault plane cuts through this volume such that two wedge-shaped boxes are formed, each containing one target fracture. These two wedge-shaped boxes correspond to the boundaries of the near-field models (see Section 3.1.2).

The model is discretized using finite difference zones. The average zone edge length within the target fracture boxes is 15 m. However, in the immediate vicinity of the target fractures, the grid is refined such that the zone edge length is 10 m along the fracture planes. Outside the target fracture boxes, in the volume surrounding the primary fault, the edge length is set to 25 m. In the far-field volume the zone edge length is gradually increased toward the model boundary such that the longest edge length is about 500 m.

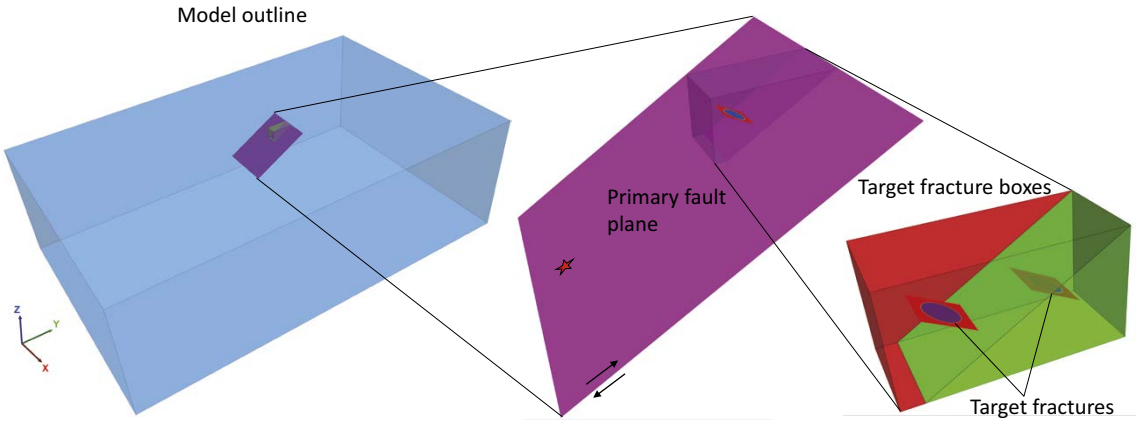

Figure 3-1. *Large-scale model geometry. The star indicates the hypocentre and the arrows indicate the sense of primary fault slip.*

Stresses and material properties

A reverse-type initial stress field is applied. This yields a thrust faulting earthquake fault movement. The stress field is based on the notion of data indicating that the intraplate crust is in a state of frictional failure equilibrium on optimally oriented faults (Zoback and Townend 2001). The stress field is constructed using a Mohr-Coulomb failure criterion (see Jaeger and Cook (1979) according to

$$\frac{\sigma_1 - P}{\sigma_3 - P} = (\sqrt{\mu^2 + 1} + \mu)^2 \tag{3-1}$$

Here σ_1 is the major principal stress, σ_3 the minor principal stress, P is the pore pressure and μ is the friction coefficient. Equation 3-1 involves only the major and minor principal stress components. The intermediate principal stress component, σ_2, is constrained by (after Gephart and Forsyth (1984):

$$R = \frac{\sigma_1 - \sigma_2}{\sigma_1 - \sigma_3} \tag{3-2}$$

Using Equations 3-1 and 3-2, a reverse stress field is constructed according to

$$\begin{aligned} \sigma_1 &= A(\sigma_3 - P) + P = \sigma_H \\ \sigma_2 &= \sigma_1(1 - R) + R\sigma_3 = \sigma_h \\ \sigma_3 &= \sigma_v \end{aligned} \tag{3-3}$$

with $A = (\sqrt{(\mu^2 + 1)} + \mu)^2$. It is assumed that σ_3 is vertical and that it corresponds to the weight of the rock overburden. It is further assumed that the friction coefficient is $\mu = \tan(35°) = 0.7$, in accordance with the site descriptive model for Forsmark (Glamheden et al. 2007), $R = 0.5$ and that the pore pressure is hydrostatic. The principal stress components are plotted in Figure 3-2. The stresses are aligned with the model axes such that $\sigma_{xx} = \sigma_2$, $\sigma_{yy} = \sigma_1$ and $\sigma_{zz} = \sigma_3$.

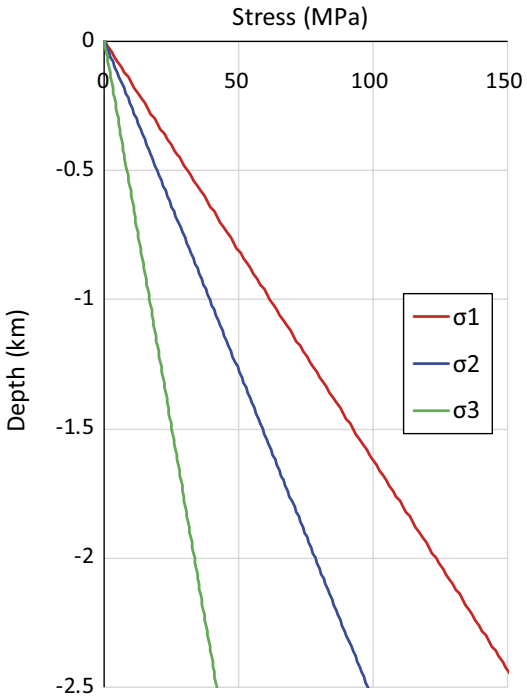

Figure 3-2. *Initial stresses.*

The rock mass is modelled as a linear elastic, isotropic and homogeneous continuum with parameter values set according to the site descriptive model for Forsmark (Glamheden et al. 2007). The discontinuities (the primary fault and target fractures) are represented by planar joint planes that respond to loads according to an ideal elasto-plastic material model with constant joint stiffness and a Coulomb failure criterion. Note that the target fractures are planar here. The secondary displacements generated on these are only used as reference when assessing the validity of the boundary conditions transferred from the large-scale model to the near-field model. The parameter values for the shear strength of the target fractures are set in agreement with the site descriptive model for Forsmark (Glamheden et al. 2007). The stiffness values are, however, generic and set to reasonably low values to avoid very short model time steps and long running times. The material property parameter values are given in Table 3-1.

Table 3-1. Material property values.

Component	Parameter	Value
Rock mass	Young's modulus, E (GPa)	70
	Poisson's ratio, v (-)	0.24
	Density, ρ (kg/m^3)	2700
	P wave speed, V_p (km/s)	5.5
	S wave speed, V_s (km/s)	3.2
Target fracture	Friction angle, ϕ (°)	35
	Cohesion, c (MPa)	0
	Normal stiffness, k_n (GPa/m)	20
	Shear stiffness, k_s (GPa/m)	20
Fault plane	Static friction coefficient, μ_s (-)	0.86
	Dynamic friction coefficient, μ_d (-)	0.55
	Slip-weakening distance, d_c (m)	0.08
	Normal stiffness, k_n (GPa/m)	20
	Shear stiffness, k_s (GPa/m)	20

The strength break-down during fault rupture simulation is modelled according to the widely used slip-weakening law (Ida 1972), where the fault frictional strength μ is modelled as a linear function of slip u over a slip-weakening distance d_c, i.e.,

$$\mu^{SW} = \begin{cases} \mu_d + (\mu_s - \mu_d)\left(1 - \frac{u}{d_c}\right) & u \le d_c \\ \mu_d & u > d_c \end{cases}. \tag{3-4}$$

Here, μ_d is the dynamic friction coefficient and μ_s is the static friction coefficient. The rupture is initiated by adopting an approach described by Bizzarri (2010). Starting at the hypocentre (Figure 3-1, middle) a radially expanding rupture is enforced to propagate at a constant rupture speed v_{force} within a nucleation region Σ_{nucl}. Here, v_{force} is set to be 50 % of the shear wave speed V_s of the surrounding medium. The friction coefficient is determined by

$$\mu = \begin{cases} \mu_{nucl} = \min\left\{\mu^{SW}, \mu^{tw}\right\} & \forall (x,z) \in \Sigma_{nucl} \\ \mu^{SW} & \forall (x,z) \notin \Sigma_{nucl} \end{cases}, \tag{3-5}$$

where μ^{SW} is determined by Equation 3-4 and μ^{tw} is given by

$$\mu^{tw} = \begin{cases} \mu_s - (\mu_s - \mu_d)\dfrac{(t - t_{force})}{t_0} & t - t_{force} < t_0 \\ \mu_d & t - t_{force} \ge t_0 \end{cases}. \tag{3-6}$$

Here, t_{force} is the time of rupture initiation and t_0 is the time over which the strength is ramped down from μ_s to μ_d, here set at 0.08 s. At some time during the initiation process, the slip-weakening (SW) law (Equation 3-4) takes over and the rupture propagates spontaneously.

When examining effects of parameter variations (in this case effects of fracture undulations), it is easier to evaluate the results if the model generates an output (in this case shear displacements) that is clear and hence easily can be distinguished from effects of possible numerical artefacts. To obtain stronger secondary stress effects, and thereby larger target fracture displacements, a high value of the dynamic friction coefficient μ_d is assigned within a circular asperity region close to the target fractures. The asperity region has a radius of a = 300 m and is centrally located along the fault strike and with its centre at 850 m depth. The dynamic friction coefficient within the asperity is varied with radial distance r according to Figure 3-3. To obtain a significant effect on the fault slip and on the corresponding secondary effects, the strength is set to a high value. At locations where $\mu_{asperity} > \mu_s$, the fault exhibits a slip-strengthening response, i.e., the shear strength increases with increasing slip.

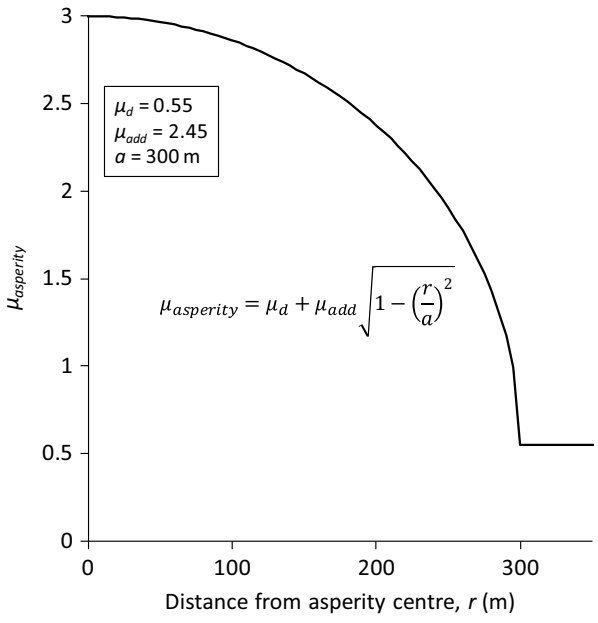

Figure 3-3. *Variation of dynamic friction coefficient within fault asperity.*

The increased shear strength simulates the potential effects of an asperity on the fault that restricts the slip locally. Here, this generates quasi-static as well as dynamic stress effects that have an impact on the amount of displacement generated on the nearby target fractures. Slip on a real fault may be restricted by, for instance, geometric features on different scales (e.g. Scholz 2002) and simulations indicate that the geometry of a slipping fault may locally have an impact on the co-seismic secondary stress effects (Johri et al. 2014). However, it is not a straightforward task to model the effects of fault irregularities using property variations on a planar fault. Here, this is done in a schematic way.

Calculation sequence

The calculation sequence comprises two steps, the quasi-static step and the dynamic step.

During the quasi-static step, initial stresses are applied (Figure 3-2), the primary fault and the target fractures are assigned their properties and the model is allowed to reach static equilibrium under gravity. The bottom boundary is locked for displacements in the *z*-direction, the vertical boundaries are locked in the *x*- and *y*-directions and the top boundary is kept free. The static equilibrium state is the point of departure for the following dynamic step.

During the dynamic step, the top boundary is kept free to allow for surface reflections, while the other boundaries are redefined to be quiet, i.e., non-reflecting. At the start of this step, all displacements are reset. Hence, the displacements presented below are the co-seismic displacements generated during earthquake rupture. The earthquake rupture is initiated and is allowed to propagate until the entire fault plane has ruptured. The target fracture shear displacements at the fracture centres as well as the *x*-, *y*-, and *z*-displacements on the boundaries of the target fracture boxes (Figure 3-1, right) are monitored and recorded.

Primary fault response

The synthetic earthquake generates an average stress drop of 6.3 MPa, an average slip of 0.63 m and a moment magnitude of M_w 5.6 over a rupture area of 20 km^2. The distributions of slip and of peak slip velocity are shown in Figure 3-4. Due to the breaching of the ground surface, there is a low resistance to slip in the upper end of the fault and the largest slip is developed in a region at shallow depth. However, the slip is clearly influenced by the high dynamic friction coefficient assigned within the circular asperity region close to the target fractures. The increased fault strength also clearly influences the slip velocities, as seen in the right plot. In that plot, it can further be noted that the slip velocities are in the range 2–3 m/s over a major part of the fault plane. These velocities are in accordance with slip velocities inferred from recorded data (Ma et al. 2003, Wald and Heaton 1994).

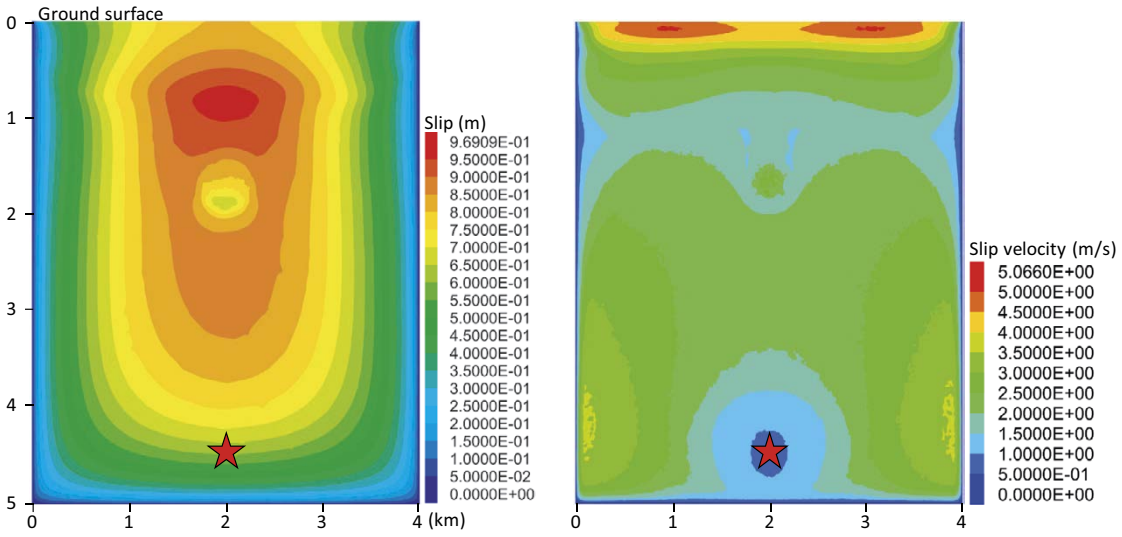

Figure 3-4. *Primary fault slip (left) and peak slip velocity (right). The stars indicate the hypocentre.*

Target fracture response

Figure 3-5 shows the temporal evolution of shear displacement at the centre of each target fracture. These displacements are used as reference when assessing the validity of the boundary conditions transferred from the large-scale model to the near-field-model, see Section 3.2.1. It can be noted that the displacements are considerably larger on the hanging wall fracture. This indicates that the dynamic secondary stress effects are stronger on this side of the primary fault. Stronger secondary effects in the hanging wall of a gently dipping and shallow fault has been observed at short distances from the fault also in previous work (e.g. Fälth et al. 2016). The strong effects result in dynamic displacement overshoot, which is followed by a rebound after about 2 seconds.

Input to the the near-field models

During simulation, the temporal evolutions of displacements in the *x*-, *y*-, and *z*-directions are monitored at a large number of points on the boundaries of the wedge-shaped boxes containing the target fractures (Figure 3-6). Note that no displacements are monitored on the side representing the ground surface since this is a free boundary, i.e., without any restrictions. The displacement histories are then used as input to the near-field models described in Section 3.1.2.

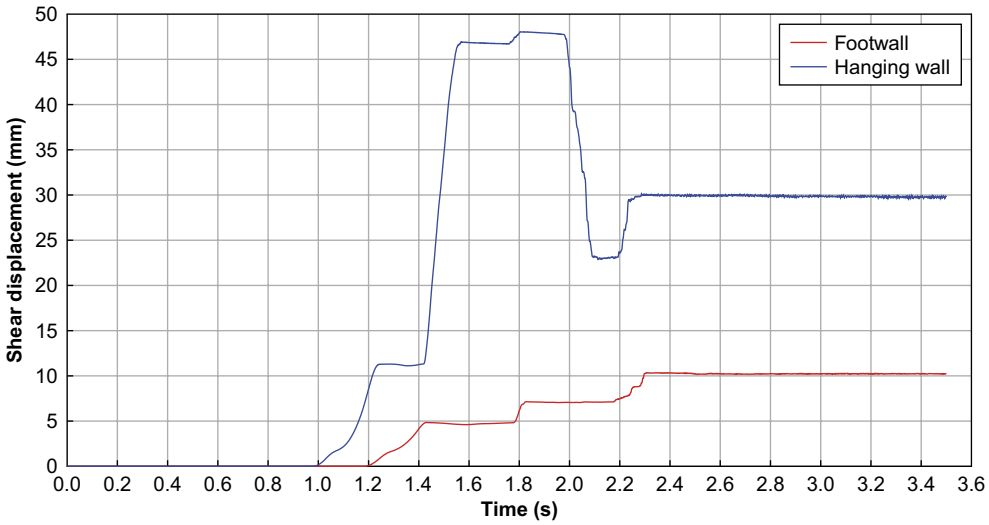

Figure 3-5. *Temporal evolution of shear displacement at the centre of each target fracture in the large-scale model.*

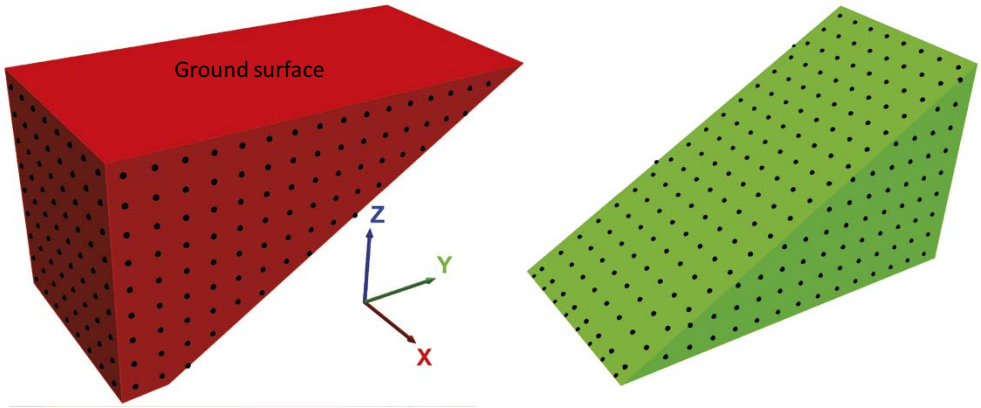

Figure 3-6. *Grid of displacement-monitoring points (black dots) on the target fracture box boundaries.*

3.1.2 Near-field models

Model outlines

The box containing the target fractures and the fault in the large-scale model is divided into two separate sets of wedge-shaped near-field models (see Figure 3-7): one on the footwall side (denoted FW-model) and one on the hanging wall side (denoted HW-model). Each near-field model contains a single circular target fracture with the same size, orientation, and location with respect to the fault as in the corresponding box in the large-scale model. To ensure that the calculation time for each model can be kept reasonably short, the resolution of the fracture surfaces is decreased compared with that used in the quasi-static models. Here, the fracture surfaces are created from triangular prisms with a shortest side-length of 10 m (5 m in the case with a non-mated fracture). The models are discretized using tetrahedral finite-difference elements with edge-lengths ranging from 3.5 m (1.8 m in the case with a non-mated fracture) around the fracture to 15 m near the model boundaries. Using the same largest edge-length in these models as in the large-scale model, implies that the shortest wavelength that can be properly transmitted through the near-field box is the same in both the near-field models and in the large-scale model.

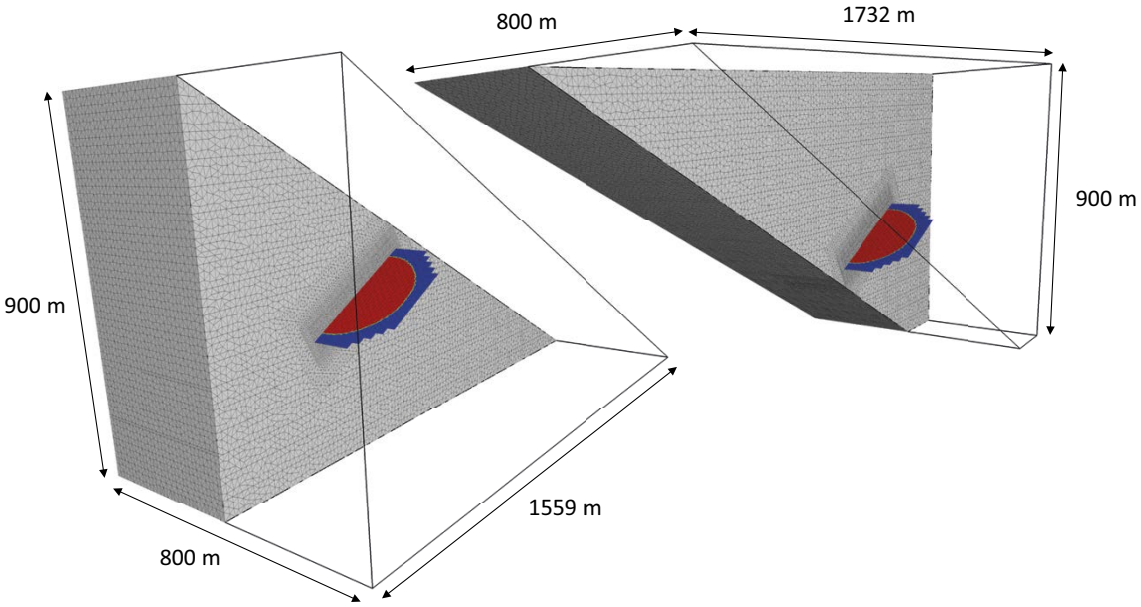

Figure 3-7. *Illustration of the two types of near-field models: footwall (FW) model (left) and hanging wall (HW) model (right). Note that parts of each model are hidden to expose the target fracture (marked in red).*

Fracture surface geometry

A subset of the fracture surface geometries considered in Chapter 2 is selected for analyses in the dynamic models. In all cases the surface wavelength is 40 m.

Matched fractures

The matched fracture geometries include

1. surfaces with "alternating asperities" with angles of deviation in the range 0° (planar surface) to 30°;
2. fractal surfaces based on one realisation using $H = 1.0$ and h_{rms} in the range $1 \times 10^{-3}\ L$ to $2 \times 10^{-2}\ L$. Note that the grid used to construct the surfaces is coarser than the one in Chapter 2, which implies that the impact of the small-scale roughness cannot be captured to the same extent by the model and the surfaces will appear smoother.

Mis-matched fractures

The set of mis-matched fracture geometries include surfaces with "alternating asperities" with the following distribution of initial apertures:

- Openings on all stoss sides (cf Figure 2-25d).
- Openings on all lee sides (cf Figure 2-25d).
- Openings on all side slopes (cf Figure 2-25e).

In all cases the angle of deviation is 10°. Four different initial apertures are tested: 10 mm, 20 mm, 50 mm, and 100 mm. In total, there are 12 different geometrical models.

Input data

Material properties

The rock mass is assumed to respond to loading as a homogeneous, isotropic and linear elastic material with the same parameter values as in the large-scale model (see Table 3-1). The fracture is assigned an elasto-plastic constitutive relation with constant normal and shear stiffnesses, zero tensile strength and shear strength based on a Mohr-Coulomb criterion. In the large-scale model, the stiffnesses are both set at a relatively low value (20 GPa/m) to achieve an acceptable time-step or, equivalently, an acceptable calculation time. This value appears to be sufficiently high to suppress elastic normal deformations for (quasi-static) normal loading or unloading of around ± 5 MPa, see Figure 2-23. The variations in normal stress during the dynamic phase can be, as shown in Figure 3-8, larger than 5 MPa. To ensure that impact of stiffness is small also for the non-planar fractures, the normal and shear fracture stiffnesses in the base-case near-field models are increased to 100 GPa/m and 50 GPa/m, respectively[3]. Alternative values of the normal stiffness are also tested to demonstrate the sensitivity to stiffness (i.e., the degree of matedness or aperture variations). The shear strength (cohesion and friction angle) is the same as in the large-scale model (see Table 3-1). The parameters and their values used in the near-field models are summarized in Table 3-2.

[3] Scoping calculations indicate that certain combinations of parameter values for k_n and k_s with k_s set at 100 GPa/m could generate large amounts of noise, which influenced the results. This was not observed when the value of k_s was reduced to 50 GPa/m.

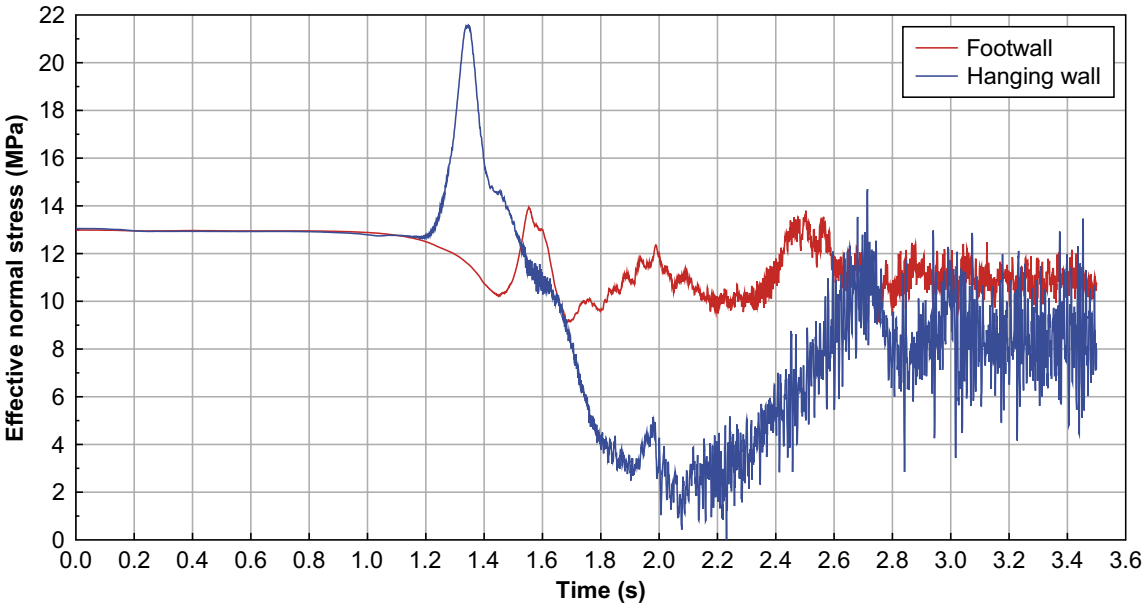

Figure 3-8. *Temporal evolution of the normal stress at the centre of the target fractures in the large-scale model.*

Table 3-2. Material property values. Alternative values are given in brackets.

Component	Parameter	Value
Rock	Young's modulus, E (GPa)	70
	Poisson's ratio, v (-)	0.24
	Density, ρ (kg/m^3)	2700
Fracture	Friction angle, ϕ (°)	35
	Cohesion*, c (MPa)	0
	Tensile strength*, σ_t (MPa)	0
	Normal stiffness, k_n (GPa/m)	100 (65.6, 6.56)
	Shear stiffness, k_s (GPa/m)	50

* The cohesion and tensile strength are ramped down in small steps during the quasi-static step from intially high values to zero to minimize non-physical movements due to unbalanced forces at the beginning of a calculation cycle (Lönnqvist and Hökmark 2015a).

In situ stress and groundwater pressure

The initial state of stress and the groundwater pressure are the same as in the large-scale model, see Figure 3-2.

Calculation sequence

The calculation sequence for the near-field models mimics that in the large-scale model and comprises the same two steps: a quasi-static step and a dynamic step.

During the quasi-static step, initial stresses are applied (Figure 3-2), the target fracture is assigned its properties (Table 3-2) and the model is allowed to reach static equilibrium under gravity. The vertical and bottom boundaries are locked for displacements in the normal directions and the top boundary (HW-model only) is kept free. The inclined boundary that represents the fault is assigned stresses according to Figure 3-2. Any aseismic shear displacements that may occur during this phase are set to zero at the start of the dynamic step.

During the dynamic step, the combined impact of the quasi-static stress-redistributions and of the stress-waves generated by the slipping fault are simulated by controlling the movements of the model boundaries according to displacement histories extracted from the large-scale model (Lönnqvist et al. 2019). The approach to do so can be summarized as follows:

- Each boundary (except the top surface in the HW-model, which is free) is divided into sub-surfaces and labelled 1 to N (the number of sub-areas and their sizes varies between the boundaries, see Figure 3-6).
- For each sub-surface, unique displacement histories in the x-, y-, and z-directions are imported from the large-scale model and converted into velocity-histories. The velocities are assigned uniformly (without interpolation) to the sub-surface corresponding to the original displacement history.

It is, however, observed that the evaluated velocity components based on raw data from the large-scale model contain a large amount of high-frequency noise, particularly during the later stages of the modelling period. To assess the influence of the noise on the fracture shear displacements, a filtering technique is used where high-frequency components are removed (see subsection 3.2.1 for details).

Time step

The default time-step in high-resolution models with high fracture stiffnesses is often very small. Consequently, such models can be very time-consuming. It is, however, possible to increase the time-step manually; the code then adds mass to certain grid-points to achieve numerical stability (so-called "partial density scaling") (Itasca 2013, Lönnqvist et al. 2019). Based on scoping calculations presented in the Appendix, the results appear to be unaffected by an increase in total mass of up to about 50 ppm. This has, therefore, been used here as a guideline to select time-steps for the models.

3.2 Results

3.2.1 Comparison with large-scale model: planar fracture

The displacement histories obtained from the large-scale model were sampled using a sampling interval of 0.8 ms and can, theoretically, resolve frequencies up to 625 Hz (Nyquist frequency). However, the near-field model volume in that model was discretized with finite-difference elements with maximum average edge-lengths of 15 m and can, given the material properties of the rock mass (cf Table 3-2) in combination with the Kuhlemeyer-Lysmer criterion (Itasca 2013), properly propagate shear waves with frequencies up to around 20 Hz. Higher frequency contents could, therefore, be regarded as numerical noise that could be removed using a low-pass filter.

The displacement histories obtained from the large-scale model are filtered using a low-pass Butterworth filter of order 6 implemented in Python. For the purpose of this study, three cut-off frequencies are tested: 20 Hz, 10 Hz and 5 Hz. The filtered displacement histories are subsequently sampled at an interval of 0.024 s corresponding to a maximum frequency of about 21 Hz.

Figure 3-9 shows a comparison between the temporal evolutions of the shear displacement history at the centre of each target fracture as simulated in the large-scale model and in the near-field models. Qualitatively, the results from the two types of models agree well. Quantitatively, however, the near-field model tends to generate larger displacements as compared to the large-scale model. This is regardless of the choice of cut-off frequency in the boundary conditions and is particularly evident on the footwall-side of the earthquake fault. The qualitative agreement indicates that the boundary conditions are correctly transferred from the large-scale model to the near-field models. The differences in displacement magnitudes between the large-scale and the near-field models can be attributed to the fact that approximations both in space and time are made in the transfer of the boundary conditions. Hence, all details in the displacement evolutions cannot be captured, and some disturbances are inevitably introduced. For instance, this may lead to differences in the wave reflections at the ground surface in the large-scale and the near-field models. In addition, it cannot be excluded that the filtering of the data has added some artefacts in the signal. However, this is not considered to be a problem here; when the impact of fracture roughness is examined, near-field model results are compared mutually and not with the large-scale model results.

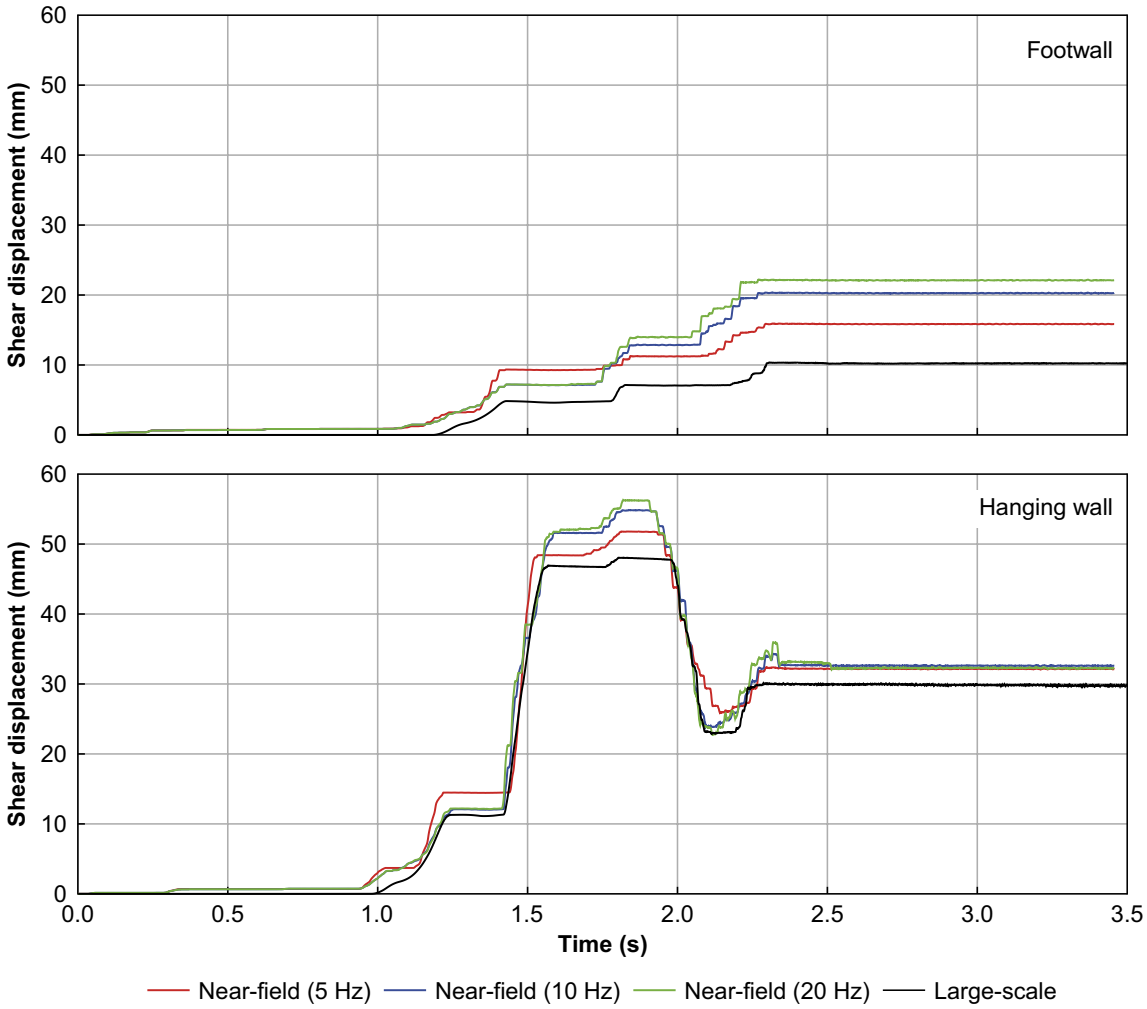

Figure 3-9. *Comparison between the induced shear displacement at the centre of the planar target fracture on the footwall side (top) and on the hanging wall side (bottom) in the large-scale model and in the near-field models with different cut-off frequencies in the boundary conditions.*

Figure 3-10 shows the temporal evolution of the normal stress at the centre of the target fracture in the near-field models. The near-field model results are associated with a larger amount of noise than in the large-scale model (cf Figure 3-8) regardless of filtering level. On the hanging wall side of the fault, the level of noise is sufficiently high that the fracture loses compression entirely; the amount of noise is, however, lowest for the model filtered at 5 Hz.

For the purpose of this study, i.e., to achieve a dynamical load scenario that can be used to assess the mechanical response of non-planar fractures to dynamical loading, the agreement between the large-scale model and the near-field model with boundary conditions filtered at 5 Hz is judged to be adequate.

Figure 3-11 shows the temporal evolution of shear stress τ, normal stress σ_N, Coulomb Failure Stress *CFS* and shear displacement at the centre of a planar fracture for the case with 5 Hz cut-off frequency in the input filtering. The quantity *CFS* is defined as $CFS = \tau - \mu\sigma_N$ (Harris 1998), and hence is a measure of fracture stability with positive values indicating instability. The graph illustrates the complex dynamic load histories which differ significantly between the footwall and hanging wall sides. Note that the stresses are obtained from models where the fracture is locked for slip. Hence, the dynamic displacement overshoot and the associated rebound (cf Section 3.1.1) in the hanging wall model is not reflected in the *CFS* evolution.

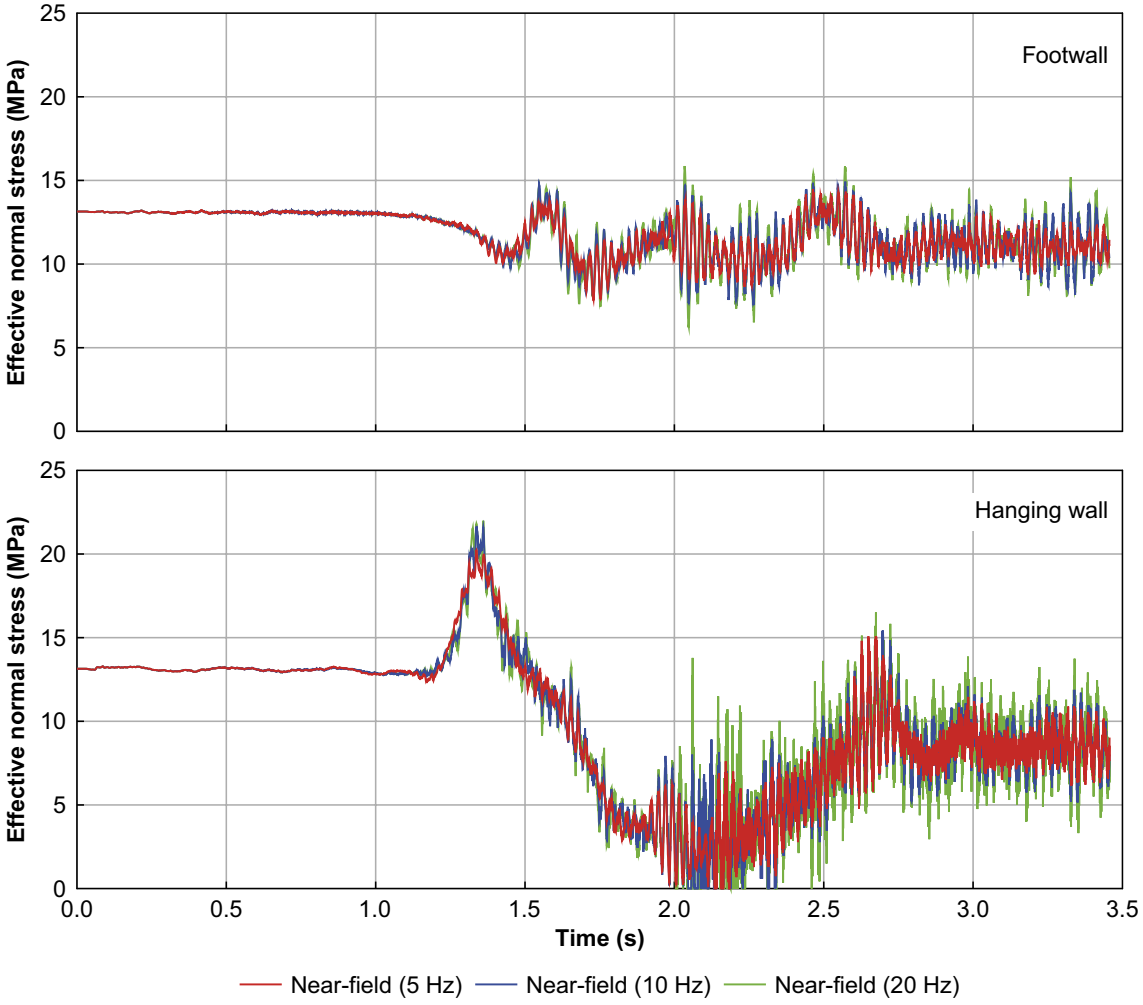

Figure 3-10. *Comparison between the normal stress evolution at the centre of the target fracture on the footwall side (top) and on the hanging wall side (bottom) in the three near-field model analyses with different cut-off frequencies in the boundary conditions.*

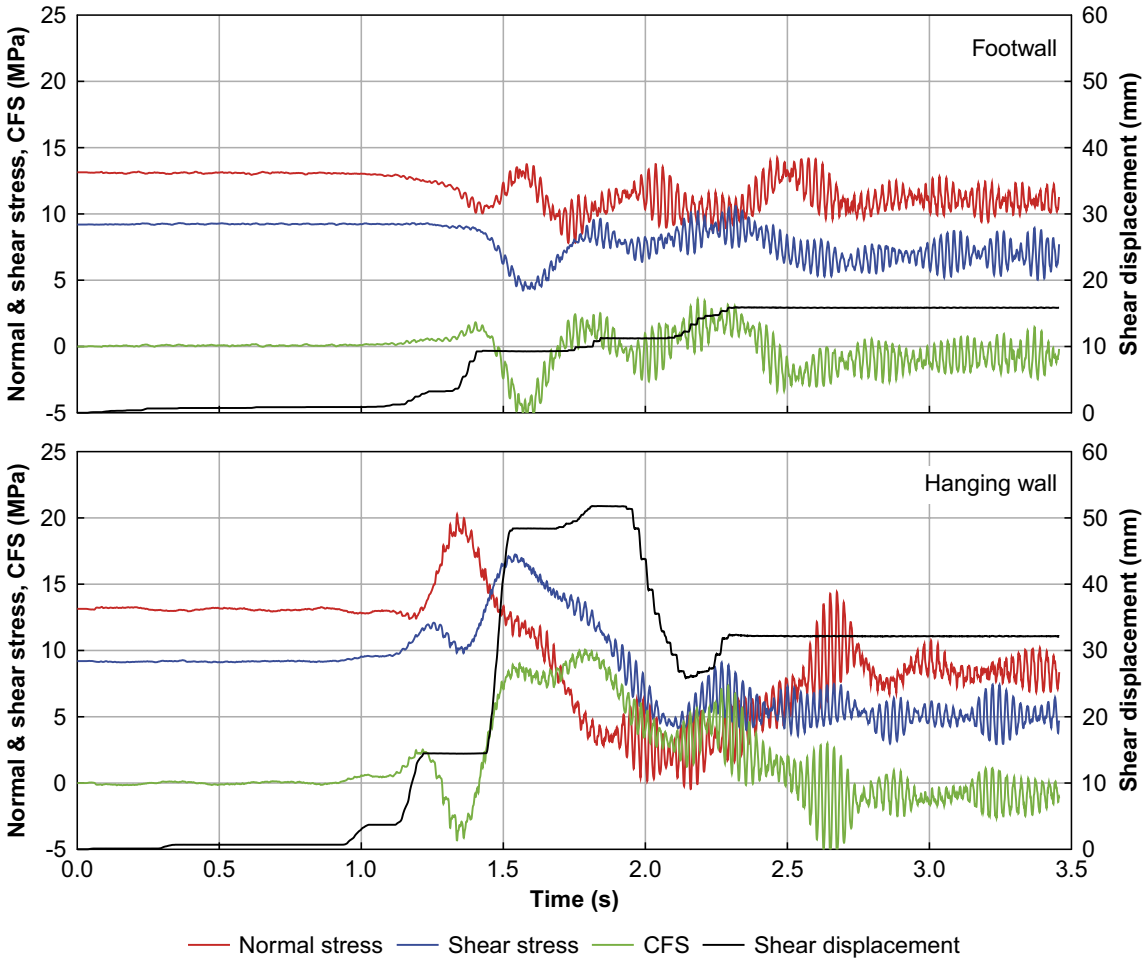

Figure 3-11. *Temporal development of the normal stress σ_N, shear stress τ, CFS and shear displacement at the centre of the planar fracture on the footwall side (top) and on the hanging wall side (bottom) of the earthquake fault. The results are generated applying a 5 Hz cut-off frequency when filtering the input. Note that the stress histories are obtained from models in which the target fracture is locked for slip.*

3.2.2 Influence of surface geometry

Figure 3-12 shows the maximum induced shear displacement on the non-planar target fractures (both the surfaces with alternating asperities and the fractal surfaces) as functions of the (average) angle of deviation. Figure 3-13 shows the same results normalised to the planar-surface-results (zero deviation) and plotted along with the corresponding quasi-static results (cf Figure 2-10, case with λ = 40 m). Similar to the quasi-static simulations, the maximum shear displacements decrease with increasing angle of deviation. Note, that the efficiency of the deviating surface segments to reduce the maximum shear displacement depends on the dynamic load that the fracture is subjected to. The reduction in displacement is smaller on the hanging wall side. This can possibly be attributed to the larger reduction of the fracture normal stress at this location (see Figure 3-11). As shown earlier, the efficiency of the deviating surface segments to reduce displacements depends on the normal stress (cf Figure 2-16). However, for the smallest angle of deviation considered here (5°), the difference between the two dynamic load cases (hanging wall and footwall) and the quasi-static case is modest. For this angle the reduction is some 10 % while the reduction is about 20 % or more for an angle of 10°.

3.2.3 Apparent shear strength

The induced shear displacements along the planar fractures take place in several steps under varying stresses (see Figure 3-11). Consequently, there does not appear to be an easy way to translate the displacement-results from the dynamic models (Figure 3-12) into excess friction angles in the same way as for the quasi-static models.

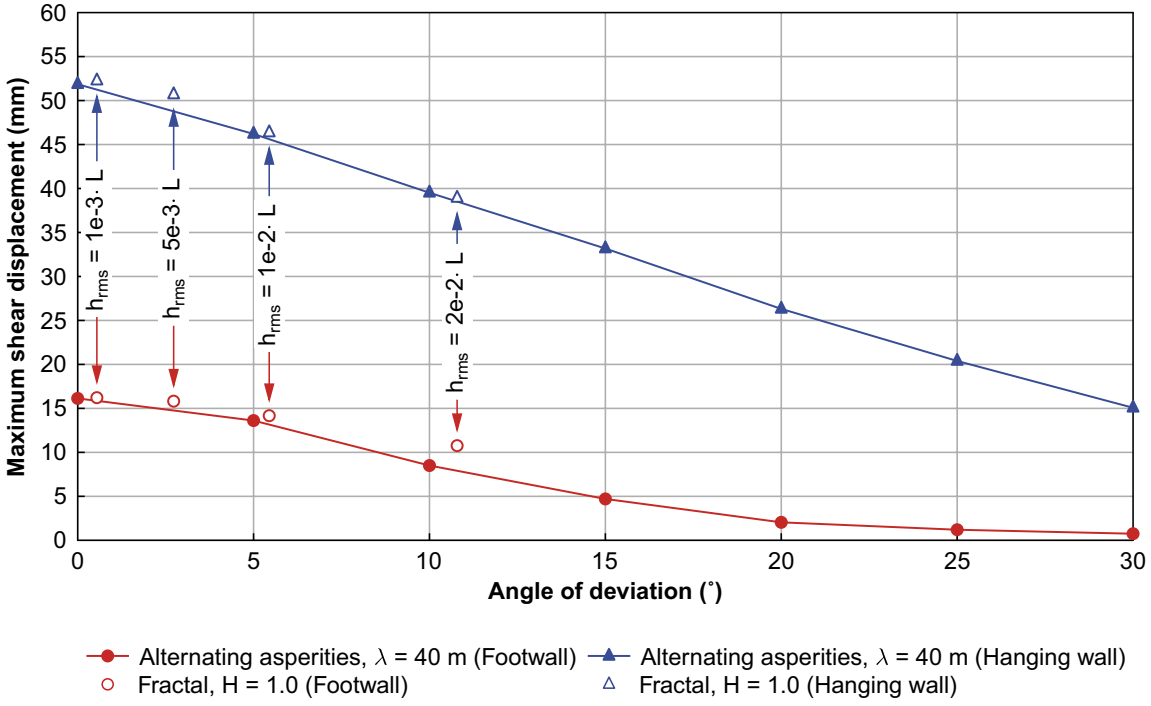

Figure 3-12. *Maximum induced shear displacement along the target fractures with alternating asperities and along the target fractures with fractal surfaces as functions of the angle of deviation. For each of the fractal surfaces, the root mean square value, h_{rms}, is marked in the graph.*

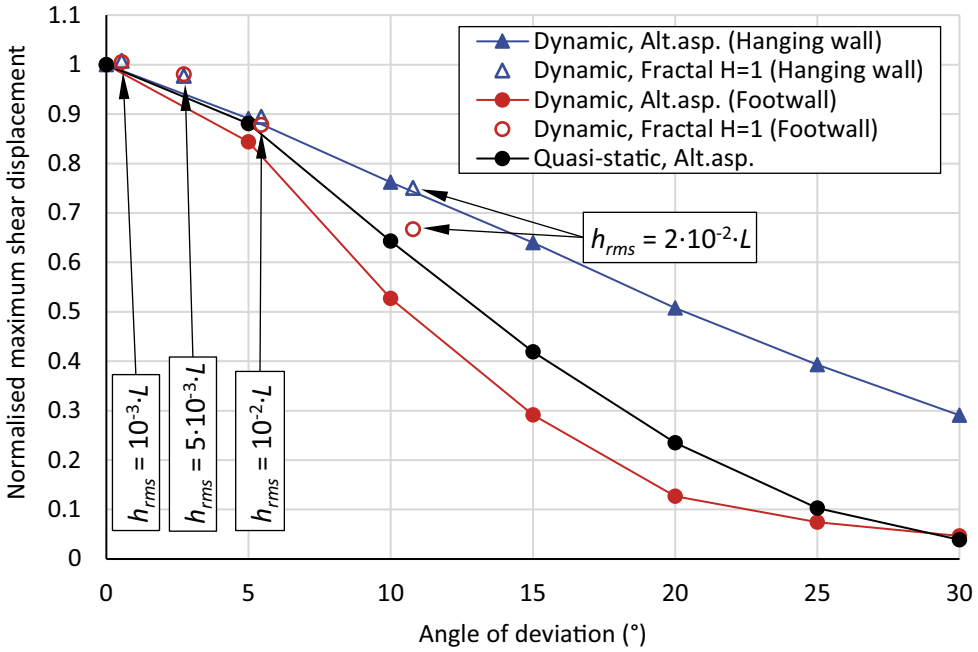

Figure 3-13. *Maximum induced shear displacement on fractures with alternating asperities and on fractures with fractal surfaces as functions of the angle of deviation. For the fractal surfaces, the root mean square value, h_{rms}, is marked in the graph. The results are normalised to the planar-surface-results (zero deviation) and plotted along with the corresponding quasi-static results (cf Figure 2-10, case with λ = 40 m).*

The results from the quasi-static models indicate that the apparent friction angle, at least to a first approximation, is equal to $\phi + \theta$ where ϕ is the lab-scale fracture friction angle and θ is the (average) angle of deviation (equivalent to dilation angle), cf Figure 2-11. To test if the mechanical response of a non-planar fracture to dynamical loading can be approximated using a planar fracture with adjusted shear strength, the models with a planar target fracture are re-analysed with adjusted shear strength according to Table 3-3. The results are shown in Figure 3-14. The following can be observed:

- On the footwall side of the fault, the planar fractures with adjusted shear strength tend to under-estimate the maximum shear displacements compared with that obtained on the non-planar fractures. The difference tends to be larger for larger angles of deviation.
- On the hanging wall side of the fault, there is a good agreement between the maximum shear displacements obtained from the models with non-planar fractures and the corresponding models with planar fractures with adjusted shear strength.
- Setting the dilation angle $i = 0$ in the case with $\theta = 5°$ gives about 8 % larger displacement on the planar fracture on both the footwall side and the hanging wall side.

One may argue that the better agreement in the results on the hanging wall side can be attributed to the lower normal stress on that fracture (cf Figure 3-11). Note that the estimate of excess friction angle was found to be slightly better for lower normal stresses in the quasi-static case when accounting for the effect of dilation (Figure 2-18). However, setting the dilation angle $i = 0$ on the planar fracture here gives the same relative increase in displacement (8 %) on the footwall side and the hanging wall side (see the case with θ = 5° in Figure 3-14). This indicates that accounting for dilation is equally important in both cases even though the normal stress levels differ (Figure 3-11). Hence, it appears that, for a fracture subjected to dynamic loading, approximating the effects of non-planarity by adjusting the shear strength on a planar fracture is not as straight forward as for a quasi-static load case.

It can be concluded for the dynamic load case tested here that, for small angles of deviation, the impact of corrugations is reasonably well approximated using a planar fracture with an excess friction angle and dilation angle, both equal to the (average) angle of deviation. However, the approximation seems to be less valid than for a quasi-static case. This can possibly be attributed to the larger complexity in the dynamic load.

Table 3-3. Adjusted fracture shear strength to approximate a surface with alternating asperities with different angles of deviation, θ.

Parameter	θ = 5°	θ = 10°	θ = 15°
Friction angle, ϕ (°)	35 + 5 = 40	35 + 10 = 45	35 + 15 = 50
Dilation angle, i (°)	0 or 5	10	15

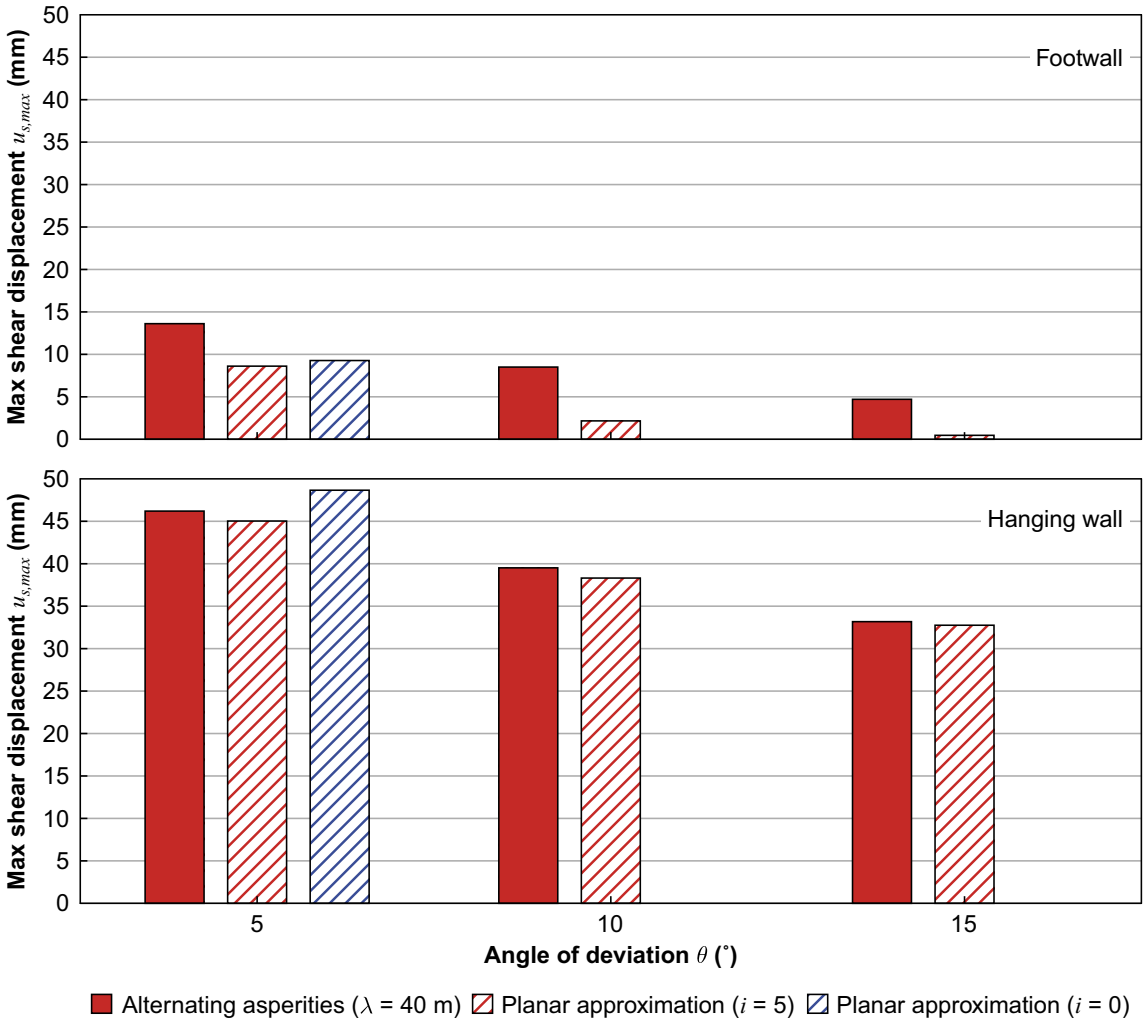

Figure 3-14. *Comparison between the maximum induced shear displacement along the target fractures with alternating asperities as functions of the angle of deviation and corresponding planar fracture approximation (cf Table 3-3).*

3.2.4 Influence of normal stiffness and aperture variations

The shear displacements in the quasi-static models were only modestly influenced by a reduction in the normal stiffness by one or two orders of magnitude (cf Figure 2-23). To assess the influence of stiffness in the dynamic case, which involves more complex loading paths with both loading and unloading sequences (cf e.g., Figure 3-8), three different values of the normal stiffness are tested: 100 GPa/m (base-case), 65.6 GPa/m and 6.56 GPa/m. The results are presented in Figure 3-15. Unlike the results from the quasi-static models, there is only an insignificant impact of normal stiffness for dynamic loading.

Although the results in Figure 3-15 suggest that the impact of soft filling materials or mis-matched fracture surfaces will be relatively small, the effects are investigated further using a model with explicitly modelled width-variations. Note that only the hanging wall model is used for this. The results of this are presented in Figure 3-16, which shows the maximum induced shear displacements on fractures (in the hanging wall) with different types of aperture variations as functions of the maximum initial aperture. The following can be observed:

- Voids located on the lee-sides or on the side-slopes of the asperities lead to 10–25 % reductions of the maximum shear displacements.
- Voids systematically located on the stoss-sides tend to increase the maximum shear displacements. Here, the increase is modest and in the order of at most around 10 mm (i.e. about 25 %) compared with the perfectly mated fracture. This is obtained for apertures ≥ 50 mm. For apertures ~ 10 mm, the increase is negligible.

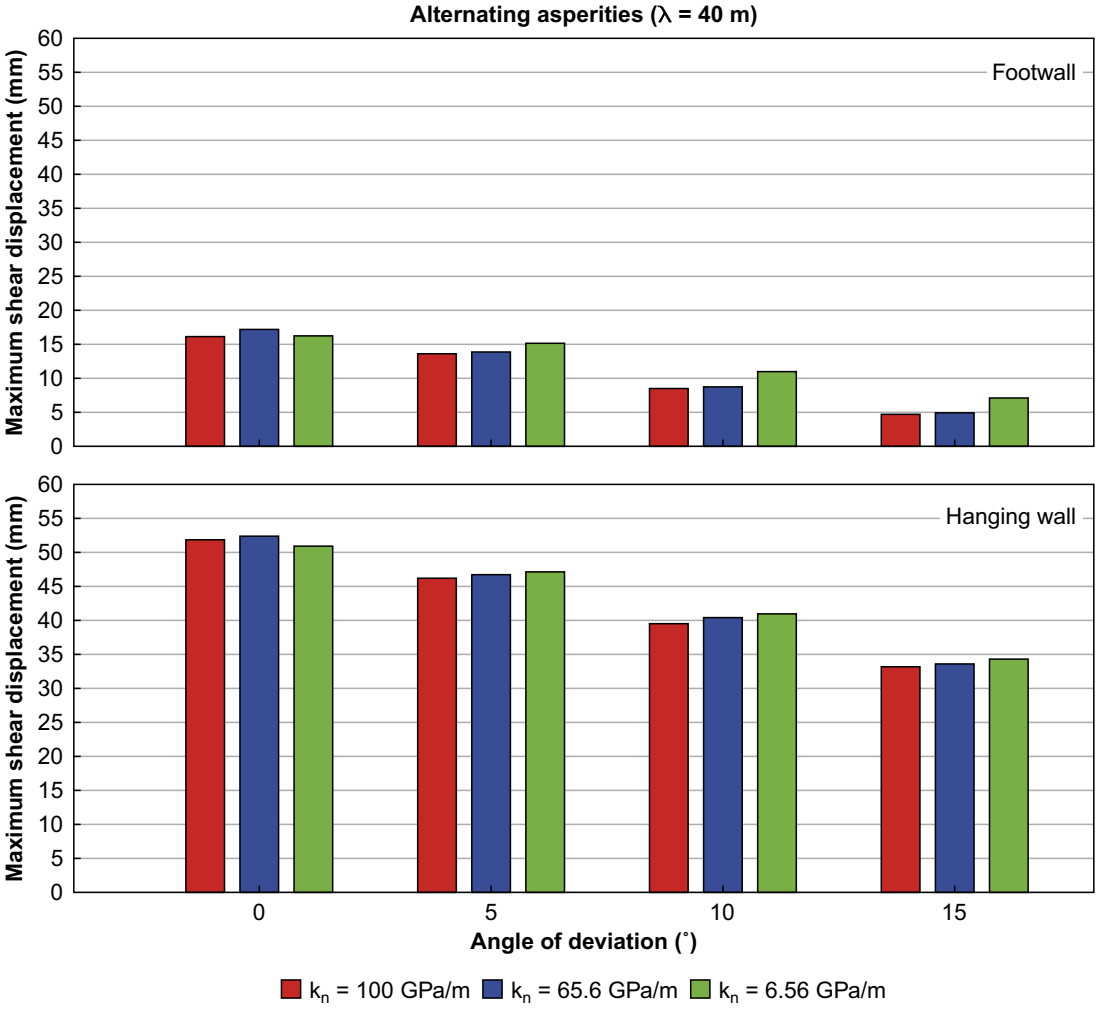

Figure 3-15. *Maximum shear displacements as functions of the angle of deviation for different values of the fracture normal stiffness (k_n) on a mated fracture. Top: fractures located on the footwall side of the fault. Bottom: fractures located on the hanging wall side of the fault.*

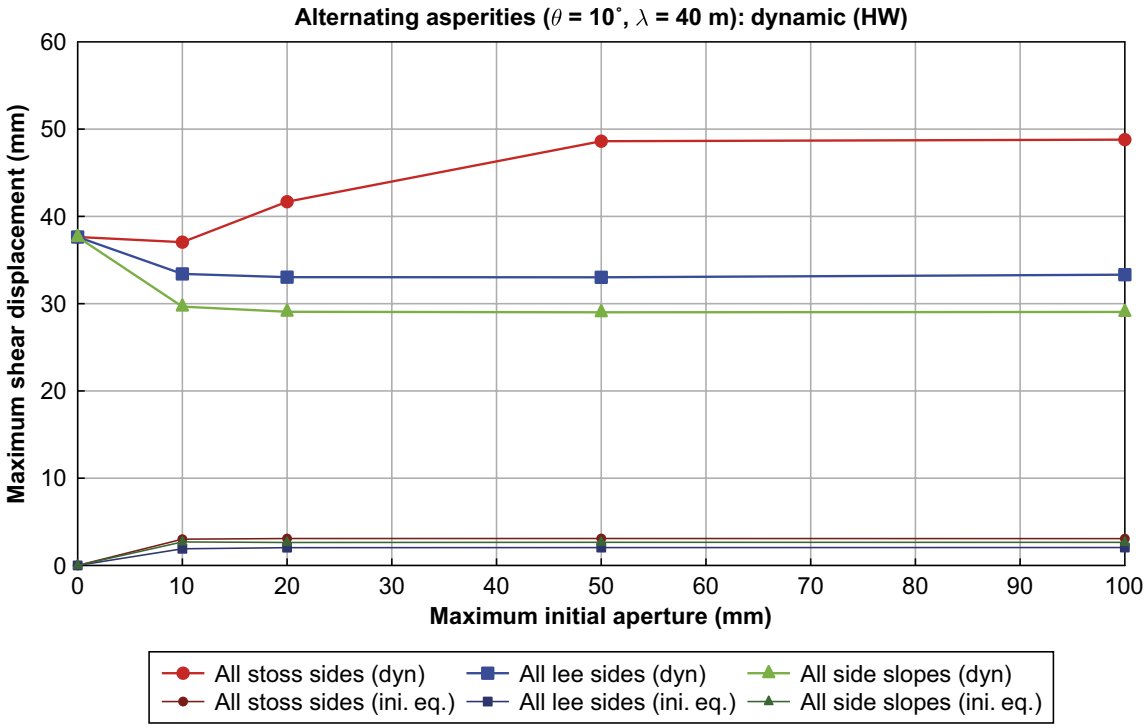

Figure 3-16. *Maximum induced shear displacements on fractures (in the hanging wall) with different types of aperture-distributions as functions of the maximum initial aperture. The aseismic slip in response to stress redistribution effects around the voids during the initial equilibrium is indicated by darker colours.*

The response of the fracture is qualitatively in agreement with that of the corresponding fracture subjected to quasi-static loading; openings on the stoss-sides lead to increased displacements while openings on the lee-sides and on the side slopes tend to give reduction in displacement. However, the impact on the displacement due to the stoss-side openings is smaller than in the quasi-static case while the lee-side and side slope openings have larger impact (cf Figure 2-29 and Figure 2-30). Due to the complex dynamic load history (cf Figure 3-11, lower), it is difficult to determine in detail the cause of these differences. From the test made here it appears, though, that fracture openings and/or fracture fillings do not lead to larger displacement increase in a dynamic load case as compared to a quasi-static case.

4 Discussion and conclusions

In this study, the influence of the surface geometry on the shear resistance of large fractures has been investigated. The intention with the study was to provide results that can be used to assess the conservativeness of the fracture shear displacement estimates that are made for the Forsmark repository site.

The work was carried out by means of numerical modelling using 3DEC. Shear displacements on 300 m diameter fractures were simulated for both quasi-static loading conditions and dynamic (earthquake) loading conditions. Results were generated for different types of surface geometries, different surface wavelengths, different surface deviation angles, and for different stress situations (different normal stresses). The impact on the results of soft fracture fillings/apertures was examined by normal stiffness variations on perfectly mated fractures as well as by explicit modelling of fracture apertures.

Shear displacements large enough to be of concern for the repository safety are only a theoretical possibility if the fracture is large, i.e., if it has dimensions on the order of several tens of metres or more (cf e.g. Fälth et al. 2010, 2016). The surface geometry of such fractures has not been documented at the Forsmark site. Therefore, as input to the numerical models, fracture surface geometries with different degrees of idealisation were used:

- Wavy surfaces with undulations in only one direction.
- Alternating asperities created by superposition of two triangular waves in orthogonal directions.
- Fractal surfaces. Two types of synthetic fractal surfaces were considered: (1) surfaces with roughness parameters based on *JRC* determined from drill core samples, and (2) fractal surfaces with generic roughness properties.

The block edge length along the fracture surfaces was 5 m, which means that the shortest surface wavelength that could be represented was 10 m for the wavy surfaces and 20 m for the alternating asperity surfaces and the fractal surfaces. Since the purpose of the work was to examine the importance of undulations on scales larger than the lab-scale, the friction angle was assumed to be the same in all cases considered here, i.e., for all different surface wavelengths. Hence, it was assumed that the small-scale (i.e. lab-scale) roughness is independent of the large-scale roughness.

The large fractures modelled in this study were assumed to be continuous, i.e., without any steps or bridges. The purpose of the work was to study the impact of modest surface undulations. It was outside the scope of this work to consider possible effects of steps or bridges, which, from a mechanical point of view, effectively may divide a large fracture into smaller fractures.

The simulation results appear to be consistent with the input assumptions and with findings in previous studies. In the quasi-static simulations, the apparent increase in friction angle imposed by the corrugations is approximately equal to the average angle of deviation. This is in agreement with experimental results (Patton 1966) as well as with numerical results (Fälth et al. 2018, Lönnqvist and Hökmark 2015a). The results also indicate that higher roughness amplitudes and shorter surface roughness wavelengths tend to add more shear resistance to the fracture (cf Fang and Dunham 2013, Marshall and Morris 2012, Ritz and Pollard 2012). These findings apply to both the schematically modelled surfaces and the fractal surfaces.

For the model cases considered here, it appears that the base case assumption of a linear elastic rock mass is valid. Only modest alterations in the results were observed when the Mohr-Coulomb elasto-plastic continuum model was applied or if the tips of the asperities were removed. As indicated by the results, including yet shorter wavelengths on the rough surfaces would give higher shear resistance. We speculate that, at some wavelength-to-displacement ratio, this could possibly lead to loads in the asperities high enough that plastic deformations are induced. In such a case, the shear resistance would be governed not only by the surface frictional properties and the surface geometry, but also by the strength of the asperities.

The potential impact of mis-match/soft fillings on fracture surfaces was examined using the alternating asperity surface geometry. In the case that gave the strongest impact on the displacements (excluding the zero-contact case in Figure 2-25f), all initial apertures were systematically located on the stoss-sides. This appears to be a logical result consistent with the input assumption. Comparing the results in Figure 2-23 with those in Figure 2-29 (lower) indicates that the stoss-side case with 20 mm initial aperture corresponds approximately to a normal stiffness reduction by two orders of magnitude on a perfectly mated fracture. Furthermore, the stoss-side case with 10 mm aperture has slightly larger relative impact than a one-order-of-magnitude stiffness reduction. Note that a one-order-of-magnitude stiffness reduction corresponds to assuming a stiffness value that is relevant for the deformation zones at Forsmark with dimensions on the km-scale (see Table 2-3). Given that there appears to be some correlation between fault/fracture size and normal stiffness, the case with 10 mm aperture on the stoss-sides could then be regarded a bounding case for Forsmark fractures with dimensions on the 0.1 km-scale.

The results from the quasi-static analyses can be summarized as follows:

- The main parameters influencing the maximum shear displacement along a non-planar fracture are the (average) angle of deviation and the (dominant) wavelength. Surfaces with steeply inclined asperities combined with small wavelengths give the largest reductions in slip. As noted above, this agrees with observations made in previous studies.
- The efficiency of a given fracture surface type to reduce the shear displacements depends on if shearing takes place under high or low normal stress. Higher normal stress means that the non-planarity introduces less dilation and more shear resistance.
- If the dominant wavelength is reasonably small in comparison with the size of the fracture (around 10 % of the fracture diameter or less) the apparent increase in friction angle i resulting from the corrugations is approximately equal to the (average) angle of deviation θ. On a non-planar fracture, the effect of dilation may be significant, particularly at low normal stresses. Hence, when simulating the effects of corrugations using a planar fracture with increased friction angle, the dilation angle should be set equal to the excess friction angle i.
- The influence of aperture variations or soft fracture filling materials, as simulated by a reduced normal stiffness, shows that the normal stiffness can be reduced by one to two orders of magnitude before any significant increase in the maximum shear displacements is observed. Given that the stoss-side case with 10 mm aperture can be regarded a relevant bounding case for estimating the impact of soft fracture fillings (cf discussion above), the results suggest that the maximum shear displacement on an undulated low-stiffness fracture may, for deviation angles in the range 5° to 15°, become some 5–15 % larger, as compared to the displacement on a high-stiffness fracture.

The results from the dynamic models are in qualitative agreement with the results from the quasi-static models in the sense that the maximum induced shear displacements along the non-planar fractures decrease with increasing angle of deviation. The efficiency of the corrugations to reduce the maximum induced shear displacement (expressed as the ratio of maximum slip along a non-planar fracture to that along the correspondingly oriented and positioned planar fracture) appears to be dependent on details in the dynamic load. However, for the two dynamic load cases tested here (hanging wall and footwall cases), and for modest angles of deviation ($\theta \sim 5°$), the reduction in displacement becomes similar and on par with the reduction obtained in the quasi-static case. For small θ the impact of the corrugations also appears to be reasonably well approximated using a planar fracture with an excess friction angle and dilation angle, both equal to the (average) angle of deviation θ.

The results presented here show that the non-planarity of fractures contributes to their shear resistance. The question is then, what amount of surface roughness can be expected on host rock fractures at Forsmark, and what is the corresponding potential impact on shear displacements? As pointed out earlier, no data of large fractures at Forsmark are available yet. However, given that the scaling from 0.1 m-scale to 100 m-scale (drill core-scale to fracture-scale) would be reasonably relevant, the fractal surfaces based on *JRC*-values from drill core samples may give an indication. The surfaces considered here were based on *JRC*-values in the range 2 to 10. Given the 5 m resolution used here, these surfaces have modest average angles of deviation approximately in the range 0.5° to 5° (Figure 2-13). According to the simulations made here, these surface geometries would give a reduction in fracture slip up to about 10 % on a mated fracture. Then, accounting for upper-bound effects

of fracture mis-match or soft fracture fillings, the reduction would be some 5 %. These numbers may be revised if site-specific data on large fractures at Forsmark become available and/or if models with higher resolution of the fracture surface are considered.

The results indicate that contributions to the fracture shear resistance from large-scale undulations can be expected at Forsmark. The effect appears to be modest, though, and the planar-fracture-assumption seems to be a fairly good but pessimistic approximation of an undulated fracture. Hence, models that include planar fractures with friction angles obtained from lab-scale samples (i.e. no account for large-scale undulations) should generate shear displacements that can be regarded as overestimates rather than underestimates.

References

SKB's (Svensk Kärnbränslehantering AB) publications can be found at www.skb.com/publications.

Bizzarri A, 2010. How to Promote Earthquake Ruptures: Different Nucleation Strategies in a Dynamic Model with Slip-Weakening Friction. Bulletin of the Seismological Society of America 100:3, 923–940. https://doi.org/10.1785/0120090179

Brady B H G, Brown E T, 1993. Rock mechanics for underground mining. 2nd ed. London: Chapman & Hall.

Chester F M, Chester J S, 2000. Stress and deformation along wavy frictional faults. Journal of Geophysical Research: Solid Earth (1978–2012) 105, 23421–23430. https://doi.org/10.1029/2000JB900241

Dieterich J H, Smith D E, 2009. Nonplanar Faults: Mechanics of Slip and Off-fault Damage. Pure and Applied Geophysics 166 (10–11), 1799–1815. https://doi.org/10.1007/s00024-009-0517-y

Fang Z, Dunham E M, 2013. Additional shear resistance from fault roughness and stress levels on geometrically complex faults. Journal of Geophysical Research: Solid Earth 118 (7), 3642–3654. https://doi.org/10.1002/jgrb.50262

Fälth B, 2015. Simulating Earthquake Rupture and Off-Fault Fracture Response. Lic thesis. Uppsala University, Sweden.

Fälth B, 2018. Simulating Earthquake Rupture and Near-Fault Fracture Response. PhD thesis. Uppsala University, Sweden.

Fälth B, Hökmark H, Munier R, 2010. Effects of large earthquakes on a KBS-3 repository. Evaluation of modelling results and their implications for layout and design. SKB TR-08-11, Svensk Kärnbränslehantering AB.

Fälth B, Hökmark H, Lund B, Mai P M, Roberts R, Munier R, 2015. Simulating Earthquake Rupture and Off-Fault Fracture Response: Application to the Safety Assessment of the Swedish Nuclear Waste Repository. Bulletin of the Seismological Society of America 105:1, 134–151. https://doi.org/10.1785/0120140090

Fälth B, Hökmark H, Lund B, 2016. Simulation of co-seismic secondary fracture displacements for different earthquake rupture scenarios at the proposed nuclear waste repository site in Forsmark. International Journal of Rock Mechanics and Mining Sciences 84, 142–158. https://doi.org/10.1016/j.ijrmms.2016.02.009

Fälth B, Lund B, Hökmark H, 2018. Influence of fault roughness on co-seismic near-fault stress evolution. In B Fälth. Simulating earthquake rupture and near-fault fracture response. PhD thesis. Uppsala university, Sweden.

Gephart J W, Forsyth D W, 1984. An improved method for determining the regional stress tensor using earthquake focal mechanism data: Application to the San Fernando Earthquake Sequence. Journal of Geophysical Research 89:B11, 9305. https://doi.org/10.1029/JB089iB11p09305

Glamheden R, Fredriksson A, Röshoff K, Karlsson J, Hakami H, Christiansson R, 2007. Rock Mechanics Forsmark. Site descriptive modelling Forsmark stage 2.2. SKB R-07-31, Svensk Kärnbränslehantering AB.

Harris R A, 1998. Introduction to special section: Stress triggers, stress shadows, and implications for seismic hazard. Journal of Geophysical Research 103:B10, 24347–24358. https://doi.org/10.1029/98JB01576

Hökmark H, Lönnqvist M, Fälth B, 2010. THM-issues in repository rock. Thermal, mechanical, thermo-mechanical and hydro-mechanical evolution of the rock at the Forsmark and Laxemar sites. SKB TR-10-23, Svensk Kärnbränslehantering AB.

Hökmark H, Fälth B, Lönnqvist M, Munier R, 2019. Earthquake simulations performed to assess the long-term safety of a KBS-3 repository. Overview and evaluation of results produced after SR-Site. SKB TR-19-19, Svensk Kärnbränslehantering AB.

Ida Y, 1972. Cohesive force across the tip of a longitudinal-shear crack and Griffith's specific surface energy. Journal of Geophysical Research 77:20, 3796–3805. https://doi.org/10.1029/JB077i020p03796

Itasca, 2013. 3DEC – 3-Dimensional Distinct Element Code, User's Guide, v. 5.0. Minneapolis, MN: Itasca Consulting Group Inc.

Itasca, 2020. 3DEC – 3-Dimensional Distinct Element Code, User's Guide. Minneapolis, MN: Itasca Consulting Group Inc.

Jaeger J C, Cook N G W, 1979. Fundamentals of rock mechanics. Third ed. London: Science Paperbacks/Chapman and Hall.

Johri M, Dunham E M, Zoback M D, Fang Z, 2014. Predicting fault damage zones by modeling dynamic rupture propagation and comparison with field observations. Journal of Geophysical Research: Solid Earth 119:2, 1251–1272. https://doi.org/10.1002/2013JB010335

Kalenchuk K S, Diederichs M S, Hutchinson D J, 2012. Three-dimensional numerical simulations of the Downie Slide to test the influence of shear surface geometry and heterogeneous shear zone stiffness. Computational Geosciences 16, 21–38. https://doi.org/10.1007/s10596-011-9245-3

Kaven J O, Hickman S H, Davatzes N C, Mutlu O, 2012. Linear complementarity formulation for 3D frictional sliding problems. Computational Geosciences 16, 613–624. https://doi.org/10.1007/s10596-011-9272-0

Lejri M, Maerten F, Maerten L, Soliva R, 2015. Paleostress inversion: A multi-parametric geomechanical evaluation of the Wallace–Bott assumptions. Tectonophysics 657, 129–143. https://doi.org/10.1016/j.tecto.2015.06.030

Lemos J V, 2008. Block modelling of rock masses: Concepts and application to dam foundations. European Journal of Environmental and Civil Engineering 12, 915–949, doi:10.1080/19648189.2008.9693054

Lindblom U, 2010. Bergbyggnad. Stockholm: Liber.

Lisle R J, 2013. A critical look at the Wallace-Bott hypothesis in fault-slip analysis. Bulletin de la Société Géologique de France 184 (4–5), 299–306. https://doi.org/10.2113/gssgfbull.184.4-5.299

Lönnqvist M, Hökmark H, 2015a. Assessment of method to model slip of isolated, non-planar fractures using 3DEC. In 13th ISRM International Congress of Rock Mechanics, Montreal, 10–13 May 2015. Lisbon: International Society for Rock Mechanics.

Lönnqvist M, Hökmark H, 2015b. Thermal and thermo-mechanical evolution of the Äspö Prototype Repository rock mass. Modelling and assessment of sensors data undertaken in connection with the dismantling of the outer section. SKB R-13-10, Svensk Kärnbränslehantering AB.

Lönnqvist M, Fälth B, Hökmark H, 2019. Influence of a Discrete Fracture Network on Seismically Induced Fracture Shear Displacements. In Hökmark H, Fälth B, Lönnqvist M, Munier R (eds). Earthquake simulations performed to assess the long-term safety of a KBS-3 repository. Overview and evaluation of results produced after SR-Site. SKB TR-19-19, Svensk Kärnbränslehantering AB.

Ma K-F, Brodsky E E, Mori J, Ji C, Song T-R A, Kanamori H, 2003. Evidence for fault lubrication during the 1999 Chi-Chi, Taiwan, earthquake (Mw7.6). Geophysical Research Letters 30:5. https://doi.org/10.1029/2002GL015380

Marshall S T, Morris A C, 2012. Mechanics, slip behavior, and seismic potential of corrugated dip-slip faults. Journal of Geophysical Research 117:B3. https://doi.org/10.1029/2011JB008642

Patton F D, 1966. Multiple modes of shear failure in rock and related materials. PhD thesis. Champaign, IL: University of Illinois.

Peitgen H-O, Saupe D (eds), 1988. The Science of Fractal Images. New York, NY: Springer New York.

Power W L, Tullis T E, 1991. Euclidean and fractal models for the description of rock surface roughness. Journal of Geophysical Research: Solid Earth 96:B1, 415–424. https://doi.org/10.1029/90JB02107

Ritz E, Pollard D D, 2012. Stick, slip, and opening of wavy frictional faults: A numerical approach in two dimensions. Journal of Geophysical Research 117:B3. https://doi.org/10.1029/2011JB008624

Scholz C H, 2002. The Mechanics of Earthquakes and Faulting. 2. Cambridge: Cambridge University Press.

Segedin C M, 1951. Note on a pennyshaped crack under shear. Mathematical Proceedings of the Cambridge Philosophical Society 47:2, 396–400. https://doi.org/10.1017/S0305004100026736

Suikkanen J, Lönnqvist M, Hökmark H, 2016. Analyses of the stability of a KBS-3H deposition drift at the Olkiluoto site during excavation, thermal loading and glacial loading. POSIVA 2016-15, Posiva Oy, Finland.

Wald D J, Heaton T H, 1994. Spatial and temporal distribution of slip for the 1992 Landers, California, earthquake. Bulletin of the Seismological Society of America 84:3, 668–691. https://doi.org/10.1785/BSSA0840030668

Zoback M D, Townend J, 2001. Implications of hydrostatic pore pressures and high crustal strength for the deformation of intraplate lithosphere. Tectonophysics 336:1–4, 19–30. https://doi.org/10.1016/S0040-1951(01)00091-9

Appendix

Influence of mass scaling

Each dynamic near-field model takes a little over two days to analyse using the default time-step Δt (cf Table A-1). To reduce the calculation time, the time-step is increased. This is done through so-called partial mass-scaling. This means that the user sets a time-step and then 3DEC adds mass to critical grid points such that a numerically stable solution is obtained. A larger time-step means that more mass is added. However, if too much mass is added there is a risk that the solution becomes affected in an undesirable way.

To assess the possibility to reduce the simulation time, different time-steps (amounts of mass-scaling) are applied, and the response of the model is monitored. The fracture displacement results shown in Figure A-1 indicate that even for the largest time-step tested here ($\Delta t = 1 \times 10^{-4}$ s), no significant effects on the results can be observed. To be on the safe side, however, the shorter time-step $\Delta t = 7.5 \times 10^{-5}$ s is used in the present work. This corresponds to a maximum increase in total model mass of about 5 ppm (Table A-1).

Table A-1. Model calculation time for different time steps.

	Time-step Δt (s)	Increase in mass (ppm)	Approximate calculation time (h)
Footwall	1.6×10^{-5} (default)	-	56
	5.0×10^{-5}	1.1	18
	7.5×10^{-5}	5.1	12
	1.0×10^{-4}	189	9
Hanging wall	1.6×10^{-5} (default)	-	57
	5.0×10^{-5}	0.9	18
	7.5×10^{-5}	4.3	13
	1.0×10^{-4}	156	10

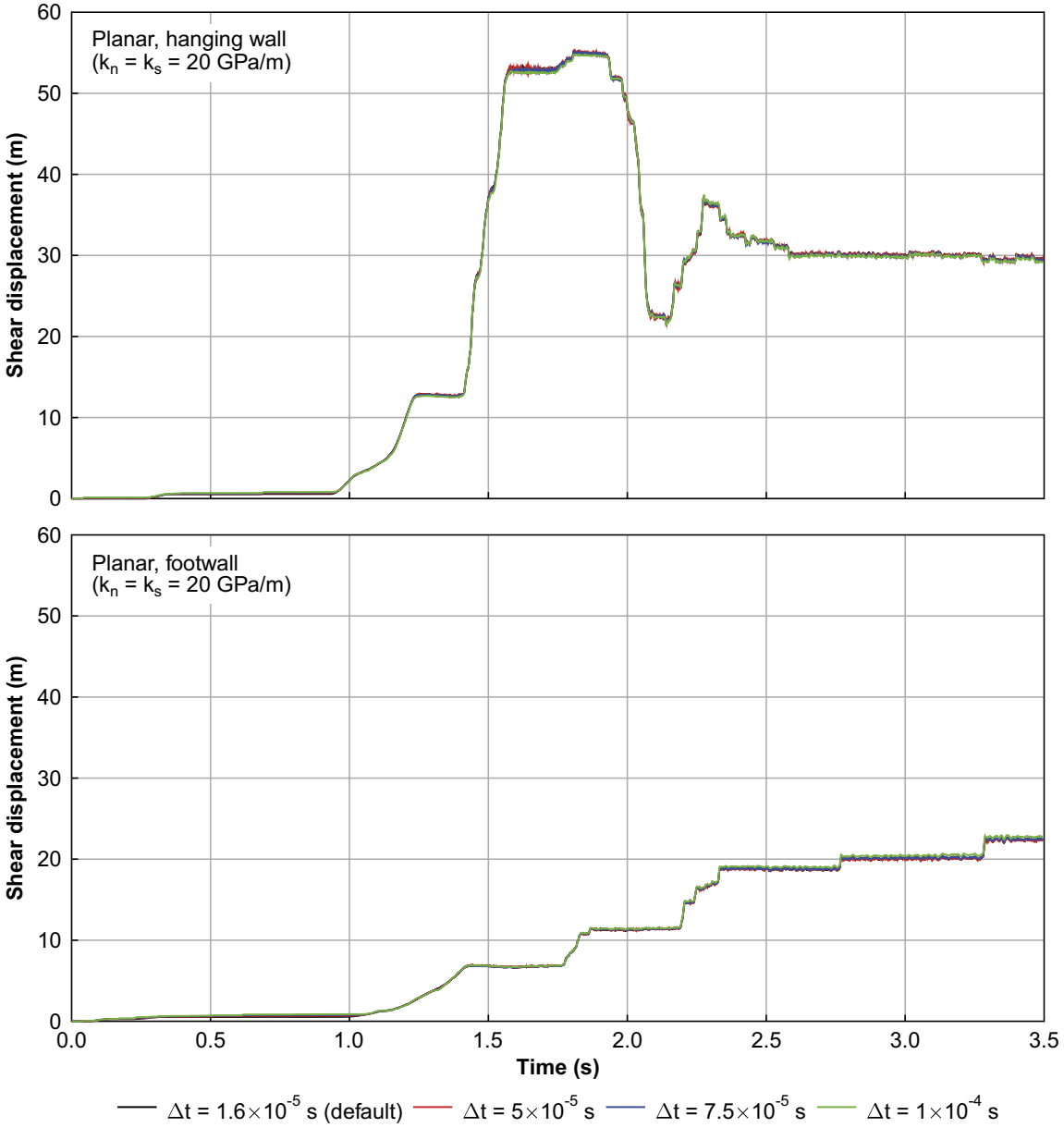

Figure A-1. *Temporal evolution of shear displacement at the centre of the target fractures for different time-steps Δt.*

Arkitektkopia AB, Bromma, 2023

SKB is responsible for managing spent nuclear fuel and radioactive waste produced by the Swedish nuclear power plants such that man and the environment are protected in the near and distant future.

skb.se